



UNIVERSITÀ
DEGLI STUDI
DI PADOVA

Head Office: Università degli Studi di Padova

Department: Ingegneria Industriale

Ph.D. COURSE IN: INDUSTRIAL ENGINEERING

CURRICULUM: MECHANICAL ENGINEERING

XXXI CYCLE

**ASSESSMENT AND DEVELOPMENT OF LASER-BASED ADDITIVE MANUFACTURING
TECHNOLOGIES FOR METAL MICROFABRICATION**

Coordinator: Prof. Paolo Colombo

Supervisor: Prof. Paolo Francesco Bariani

Ph.D. student: Saeed Khademzadeh

I would like to dedicate this thesis to my wonderful wife
who always supported me

Acknowledgements

I would like to express my special appreciation and thanks to my supervisor Prof. Paolo Francesco Bariani who has been a tremendous mentor for me. I would like to thank him for his continuous and invaluable support to me. This work could not have been made without his precious guidance. I would like to express my gratitude to my colleagues at the precision manufacturing engineering group of the industrial engineering department, University of Padova: Prof. Simone Carmignato for his valuable suggestions and support, Dr. Filippo Zanini, Ing. Nicolò De Marchi, Ing. Jessica Rocco and Ing. Luca Biasiolo. I also would like to thank Ing. Riccardo Manzetto, Te. Si laboratory engineer, for all his help to conduct experiments. I would like to thank Dr. Katya Brunelli from materials group of our department for all her help to conduct XRD experiments. Words are not enough to express how grateful I am to my amazing family, particularly my parents, brothers and my sister for their love and support.

Saeed Khademzadeh

“Imagination is more important than knowledge, Knowledge is limited,

Imagination encircles the world”

Albert Einstein

Abstract

Nowadays many devices are produced in very small sizes or containing small features for particular application such as biomedical and microfluidic devices. Based on this demand, manufacturing processes should be developed for implementation of micro features in different ranges of sizes. A broad range of microfabrication technologies have been developed which have different applications and capabilities such as laser ablation, plating, photolithography, lithography and electroplating. However, such techniques are restricted when utilized to new microproducts which need the employment of a diversity of materials and have complicated three-dimensional geometries. Additive manufacturing (AM) needs each layer to be fabricated according to an exact geometry defined by a 3D model. This concept seems suitable for production of complicated parts with micro features. Development of robust metal additive manufacturing for microfabrication opens a new window toward miniaturization of metallic parts such as design and production of porous implants containing micro features and micro pores (50-500 μm). This work covers the development of micro additive manufacturing through two laser based AM processes with two different concepts: Micro direct metal deposition (μDMD) and selective laser melting (SLM). Nowadays, NiTi shape memory alloys are among the most interesting materials in the field of bioengineering and medical applications. Assessment of both techniques for production of NiTi porous scaffolds for biomedical application was carried out in this thesis. Long-term fixation of biomedical implants is achievable by using porous materials. These kinds of materials can develop a stable bone-implant interface. A critical aspect in production of porous implants is the design of macro and micro pores.

At the first step of this thesis, the process parameters of both technologies were optimized to obtain full density samples. Secondly, porous scaffold structures with geometry controlled porosity were designed and manufactured using both technologies. Investigations using X-ray diffraction and scanning electron microscopy equipped with energy dispersive spectroscopy showed that B2-NiTi phase with small quantity of unwanted intermetallics can be obtained by micro direct metal deposition of mechanically alloyed $\text{Ni}_{50.8}\text{Ti}_{49.2}$ powder. Micro direct metal deposition was optimized through a set of process parameters and designed experiments to improve the geometrical accuracy and repeatability of micro fabrication. Micro X-ray

computed tomography were used to analyze the surface topography, micro porosity, and deviations of products with respect to nominal geometrical models. Below 10% deviation to nominal geometrical models was achieved in hollow NiTi samples through a set of micro direct metal deposition process parameters and designed experiments.

A comprehensive study was conducted on Ni_{50.8}Ti_{49.2} (at%) alloy to discover the influence of SLM process parameters on different aspects of physical and mechanical properties of NiTi parts. The provided knowledge allowed choosing different optimized parameters for production of complicated geometry with micro features maintaining the phase composition through the sample. For the first time and in this thesis, without going through any solid solution and heat treatments, single phase austenite was obtained in SLM NiTi parts with the selection of three different regimes of process parameters. This knowledge led to manufacture of NiTi bony structure applying different process parameters for the border and internal parts. The experimental results showed that SLM process with specific process parameters is a feasible micro additive manufacturing method to implement the complicated internal architecture of bone. It is an important issue in production of customized prostheses.

Contents

Contents	ix
List of Figures	xiii
List of Tables	xix
Nomenclature	xxi
Chapter 1 Introduction.....	1
1.1 Micro manufacturing, classifications and methods.....	2
1.2 Additive manufacturing.....	3
1.2.1 Basic principles of additive technologies	3
1.2.2 Additive Micro manufacturing	6
1.2.3 MICA process	7
1.2.4 Micro direct metal deposition (μ DMD).....	8
1.2.5 Selective laser melting (SLM)	10
1.3 Fabrication of NiTi component with micro features.....	11
1.3.1 History of shape memory alloys	11
1.3.2 NiTi shape memory alloy (shape memory effect, superelasticity)	12
1.3.3 NiTi fabrication methods	13
1.3.4 Additive manufactured NiTi alloys	16
1.3.5 NiTi porous scaffolds for biomedical application and bone printing	17
1.4 Objectives and technical approach.....	22
Chapter 2 Experimental procedure	25
2.1 Experimental procedure of μ DMD process	25
2.1.1 Preparation of NiTi alloy powder	25
2.1.2 Aluminium-Titanium-Niobium alloy powder.....	27
2.1.3 Micro direct metal deposition process	27
2.1.4 Micro direct metal deposition samples	30
2.1.5 Evaluation of μ DMD parts using micro computed tomography	36
2.2 Experimental procedure of SLM process.....	38
2.2.1 Initial powders	38
2.2.2 Selective laser melting process	39
2.2.3 Facilities for preparation and characterization of μ DMD and SLM samples....	41
Chapter 3 Results and discussion: μ DMD.....	46
3.1 APP (Aiming to Process Parameters) procedure.....	46
3.1.1 μ DMD process parameters	47

3.1.2	New approach to calculate the height of single tracks and thin walls	55
3.2	Single phase NiTi by μ DMD of elemental powder mixtures	59
3.2.1	High energy mechanical alloying of (Ni-Ti) mixtures	60
3.2.2	Micro direct metals deposition of mechanically alloyed NiTi alloy.....	64
3.3	Investigation of micro pores in μ DMD NiTi parts by means of micro computed tomography	71
3.3.1	Inherent micro porosity in NiTi alloy fabricated by μ DMD	72
3.3.2	Controllable micro porosity in μ DMD NiTi parts	78
3.4	Textural evolution during μ DMD of NiTi alloy	83
3.5	Microfabrication of NiTi parts using micro direct metal deposition	91
3.6	Production of multi section samples using μ DMD	99
3.7	Summary and conclusion (μ DMD of NiTi)	103
Chapter 4	Results and discussion: SLM of NiTi and production of lattice structures	107
4.1	Production of dense NiTi using SLM	107
4.1.1	The effect of process parameters on phase transformation in SLM NiTi.....	111
4.1.2	The effect of platform's material on quality of products	116
4.1.3	Surface topography evaluation	117
4.1.4	Porosity analysis in SLM NiTi alloy	122
4.2	Design and manufacture of self-supported scaffolds	125
4.2.1	The effect of SLM process parameters on microstructure of stainless steel 316L alloy	125
4.2.2	The effect of pore shape on productivity of lattice structures	130
4.2.3	The effect of porosity distribution on mechanical properties	133
4.3	NiTi porous scaffolds and bone printing.....	141
4.3.1	Computed tomography of bone biopsy.....	141
4.3.2	Support design for NiTi scaffolds.....	143
4.3.3	Design and SLM fabrication of regular and natural porous scaffolds.....	145
4.4	Summary and conclusion (SLM of NiTi)	154
Chapter 5	General conclusions	157
References	158
Appendix A	Governing equations of powder and gas motion in μ DMD process.....	A-1
A.1	Carrier gas equations.....	A-1
A.2	Modelling of powder particles	A-3
Appendix B	G-codes, laser focus position	B-1
Appendix C	G-codes, single tracks	C-2
Appendix D	G-codes, thin walls	D-2
Appendix E	G-codes, cubes ($\theta_T=0$, $\theta_L=90$)	E-2

Appendix F	Description of Finite Element	F-1
------------	-------------------------------------	-----

List of Figures

Figure 1.1– STL format designs with different dimensions of triangles [9]	4
Figure 1.2– MICA Freeform metal products containing micro features	8
Figure 1.3– Schematic diagram of micro direct metal deposition system [13]	9
Figure 1.4– The schematic of powder bed fusion-laser process [24]	11
Figure 1.5– Schematic of shape memory effect of SMAs [32].	13
Figure 1.5– Major drawbacks in machining NiTi shape memory alloys: (a) high tool.....	14
Figure 1.7– (a) Laboratory setup for VIM processing of binary NiTi (1: graphite	16
Figure 1.7– Macro and microstructure of cortical and cancellous bone.....	18
Figure 1.8– CPP porous scaffolds with a hollow centre and different graded porous layers [45].....	20
Figure 1.9– Process map for production of bio-inspired implants using SLM and regular unitcells	20
Figure 2.1– Scanning electron micrographs of starting materials, (a) Titanium powder particles, (b) Nickel powder particles	26
Figure 2.2– X-ray patterns of Ni ₅₀ Ti ₅₀ after 4h and 8h of milling.....	27
Figure 2.3– Schematic diagram of μ DMD process (nozzle shape: conic, lower width of the nozzle: 6 mm, number of injectors: 11, injector’s diameter: 0.5 mm).....	28
Figure 2.4- Components of powder feeding system, MSL50 machine, Manudirect.....	28
Figure 2.5- Coaxial nozzle used for powder injection in MSL50 machine, Manudirect.....	29
Figure 2.6- Interface of CALD software, Manudirect company	30
Figure 2.7– Micro direct metal deposition process samples in this project.....	30
Figure 2.8– Steel 316L substrate holder and Ti pellet substrates	31
Figure 2.9– SEM image of NiTi single tracks produced by μ DMD (RF _n : 1.26 mg/sec), (b): 3D optical profiles of NiTi single tracks.....	32
Figure 2.10– Schematic of layer array and overlap between layers.	32
Figure 2.11– Design nr.1 (a) and design nr. 2 (b) of hollow samples with internal holes (top view)	35
Figure 2.12– Nikon MCT 225 micro computed tomography system.....	37
Figure 2.13– μ CT analysis of thin walls produced by μ DMD and inherent micro pore analysis at the central part (red shaded areas).....	38

Figure 2.14– SEM micrograph of pre-alloyed Ni _{50.8} Ti _{49.2} powder produced by gas atomization, TLS company	39
Figure 2.15– SISMA MYSINT 100 selective laser melting machine	40
Figure 2.16– Schematic of SLM process in MYSINT100	40
Figure 2.17– Roadmap in SLM process	41
Figure 2.18– Carbolite CWF furnace.....	42
Figure 2.19– Differential scanning calorimetry (DSC Q200)	42
Figure 2.20– Scanning electron microscope (Quanta 450, FEI) equipped with EDS and EBSD	43
Figure 2.21– X-ray diffractometer X'Pert Pro MRD, Panalytical	44
Figure 2.22– Optical profilometer (Sensofar Plu Neox).....	45
Figure 3.1– NiTi single tracks, (a) P= 20 W, V= 20 mm/min, dl= 30 μm, E= 2 KJ/mm ² , (b) P= 30 W, V= 20 mm/min, d= 30 μm, E= 3 KJ/mm ² , red arrows show baling effect (c) P= 50 W, V=20 mm/min, d= 30 μm, E= 5 KJ/mm ²	48
Figure 3.2– Scanning electron micrographs of single tracks using (a) P= 15 W, (b) P= 40 W of laser power.....	49
Figure 3.3– Coaxial powder feeding system in micro laser melting machine, RFn= 0.76 mg/sec, carrier Argon flow= 0.7 lit/min, (S2= 2.57 mm).....	50
Figure 3.4– (a) Positions of laser focus point (d _{LF}), middle of dense powder column (d _{PF}) and working plane (d _{WP}), (b) different regions of dense powder column (Ar flow: 0.7 lit/sec), (S2= 2.57 mm), (all dimensions in mm).....	51
Figure 3.5– Road map for finding the best positions of working plane and laser focus in μDMD process.....	52
Figure 3.6– (a) NiTi single tracks produced by different working plane positions, same laser focus point (S2+1.5mm) and same process parameters (P= 30 W, dl= 30 μm, V= 50 mm/min, RFn= 1.26 mg/sec), (b) NiTi single tracks produced by different working plane positions, same laser focus point (S2+2 mm) and same process parameters (P= 30 W, dl= 30 μm, V= 50 mm/min, RFn= 1.26 mg/sec)	53
Figure 3.7– Optical profiles of thin walls produced by μDMD, working plane: S2+2.2 mm, laser focus plane (a): S2+2.4, (b): S2+2.2 and (c): S2+2 mm.	54
Figure 3.8– NiTi thin walls produced by μDMD and P= 30 W, ΔZ= 10 μm, RFn= 1.26 mg/sec, NH= 100 μm, V= (a, Wall 1): 20, (b, Wall 2): 50, (c, Wall 3): 70 mm/min.....	56
Figure 3.9– (a) 2D optical profiles of NiTi thin walls (1) to (3) according to Table 3.2, (b) 3D image rendering of wall (2).....	57
Figure 3.10– (a) the effect of scanning speed on the height of NiTi thin walls produced by μDMD (η=0.5), (b) NiTi single tracks, P= 50 W, RFn= 1.26 mg/sec, V= (1): 20 mm/min, (2): 40 mm/min.	58
Figure 3.11– X-ray diffraction patterns of Ni ₅₀ Ti ₅₀ alloy powder after different time of milling (powders A, B and C).....	61
Figure 3.12– Morphology of Ni ₅₀ Ti ₅₀ alloy powder particles after (a) 4h (powder A) and (b) 8h (powder B) of milling time	62

Figure 3.13– Backscattered electron micrographs of Ni ₅₀ Ti ₅₀ powder particles after (a) 4h of milling (powder A) and (b) 8h of milling (powder B).....	62
Figure 3.14– EDS analysis in line scan mode of Ni ₅₀ Ti ₅₀ powder particles after (a) 4h of milling (powder A) and (b) 8h of milling (powder B).....	63
Figure 3.15– X-ray diffraction pattern of laser melted Ni ₅₀ Ti ₅₀ (cube 1, Table 3.4).....	64
Figure 3.16– Chemical composition of phase constituents in laser melted Ni ₅₀ Ti ₅₀ powder (Cube 1, Table 3.4)	65
Figure 3.17– Ni-Ti phase diagram [73]	66
Figure 3.18– X-ray patterns of NiTi cubes 1 and cube 2 (see Table 3.4).....	68
Figure 3.19– X-ray patterns of 10h mechanically alloyed Ni _{50.8} Ti _{49.2} before (powder D) and after (powder E) heat treatment	69
Figure 3.20– SEM micrographs of 10h mechanically alloyed Ni _{50.8} Ti _{49.2} before (powder D) and after (powder E) heat treatment.....	70
Figure 3.21– EDS analysis of 10h mechanically alloyed Ni _{50.8} Ti _{49.2} powder particles (a): before heat treatment (powder D) and (b): after heat treatment (powder E)	70
Figure 3.22– X-ray patterns of laser deposited cube 2 and cube 3 (Table 3.4)	71
Figure 3.23– Effect of scanning speed and substrate temperature on the height of single tracks produced by μDMD with (a) 0.76 mg/sec and (b) 1.26 mg/sec powder feeding rates.....	73
Figure 3.24– Effect of layer overlap in fabrication of NiTi thin walls by μDMD (a) without overlap between layers, (b) with 10% overlap between layers.....	73
Figure 3.25– Effect of layer overlap and temperature of substrate on shape and inherent micro porosity distribution of thin walls (a): T=200 °C, V=150 mm/min, %OV=0%, porosity =1.49%, (b): T=200 °C, V=150 mm/min, %OV= 30%, porosity = 0.98%, (c): T=300 °C, V=70 mm/min, %OV=0%, porosity =1.01%, (d): T=300 °C, V=70 mm/min, %OV=30%, porosity =0.79%.....	75
Figure 3.26– Effect of scanning speed and temperature of substrate on inherent micro porosity of NiTi thin walls produced by μDMD (a): without overlap between the layers, (b): with 30% overlap between layers	77
Figure 3.27– Effect of layer overlap and temperature of substrate on inherent micro porosity of NiTi thin walls produced by μDMD	78
Figure 3.28– SEM micrographs of top surface of NiTi cubes produced by μDMD with (a) 100 μm, (b) 150 μm, (c) 200 μm hatch distances. (T = 200 °C, P = 30 W, V = 100 mm/min, ΔZ=4 μm, RF _n : 1.26 mg/sec, strategy of scanning: strategy B according to Table 2.4)	79
Figure 3.29– SEM micrographs were taken of top surface of μDMD NiTi cubes produced by (a) strategy A, (b) strategy B, (c): strategy C, (d) strategy (D), (e) strategy E of scanning according to Table 5, (f) small inherent micro pores in higher magnification	80
Figure 3.30– Total porosity percentages and mean value of micro pore's sizes in micro laser melted NiTi cubes produced by different strategies of scanning.....	81
Figure 3.31– EBSD orientation maps from the top view of the μDMD-processed NiTi samples representing three main phases distribution in three scanning strategies of A, C and D according to Table 2.4, (a, b, c): all phases, (d, e, f): NiTi, (g, h, i): NiTi ₂ , (j, k, l): Ni ₃ Ti. The scanning (RD-TD) and building (BD) directions are indicated by the black arrows on the top left	84

Figure 3.32– The corresponding (100) and (111) pole figures (PFs) of NiTi cubes produced by strategies A (a, b), strategy C (c, d) and D (e, f) according to Table 2.4.....	89
Figure 3.33– orientation distribution function (ODF) plots of the μ DMD fabricated NiTi samples corresponding to the EBSD scans shown in Fig. 4, (a) strategy A, (b) strategy C and (c) strategy D according to Table 2.4.....	90
Figure 3.34– Scanning electron micrographs of NiTi samples A and B	92
Figure 3.35– (a) Cross section of sample B obtained by μ CT and (b) determined surface (white contour). Controllable micro porosity distribution between single tracks can be observed.....	93
Figure 3.36– Distribution of the deviations of sample B (measured by μ CT) with respect to the CAD model shown as colour-coded map of deviations.....	94
Figure 3.37 (a) Diagram showing the amount of surface area of sample B interested by each specific deviation value. Each set of points (shown in different colours) corresponds to a specific hole; (b) least-squares diameters and position of the internal holes compared to nominal diameters and position	94
Figure 3.38– Scanning electron micrographs of NiTi sample C	95
Figure 3.39– Scanning electron micrographs of (a) NiTi sample with 500 μ m hole diameter produced by μ DMD in this research, (b) Ti hollow sample with 750 μ m hole diameter produced via SLM by Hollander et al. [23]	97
Figure 3.40– Distribution of the deviations of sample C (measured by μ CT) with respect to the CAD model shown as colour-coded map of deviations.....	97
Figure 3.41– (a) diagram showing the amount of surface area of sample C interested by each specific deviation value. Each curve corresponds to a specific hole; (b) least-squares diameters and position of the internal holes compared to nominal diameters and position	98
Figure 3.42– Porosity distribution between tracks in NiTi samples (a) B and (b) C produced by μ DMD.....	99
Figure 3.43– Exponential decay with different exponential decay constant	100
Figure 3.44– CAD model of simple cone with maximum overhang of 20°	101
Figure 3.45– Process parameters adssignment for fabrication of Ti-Al-Nb cone using μ DMD and heat decay model: Layer 1: 50 μ m, Layer 2: 200 μ m, Layer 3: 500 μ m, Layer 4: 1000 μ m, Layer 5: 5500 μ m, Layer 6: 1750 μ m	102
Figure 3.46– Ti-Al-Nb cone produced by μ DMD using heat decay model (in collaboration with Manudirect company)	103
Figure 4.1– (a, b) two CAD designs used in this study for NiTi samples, (c) an overview of the chessboard hatching strategy used in this study.....	108
Figure 4.2– DSC curves of SLM NiTi samples produced by two different input energy densities according to Table 3.....	111
Figure 4.3– XRD patterns of SLM NiTi samples produced by LP and MP parameters (Table 4.4) and two different layer thicknesses (a) 0.02 mm and (b) 0.025 mm	114
Figure 4.4– XRD patterns of SLM NiTi samples produced by LP parameters (Table 4.4) and two different layer thicknesses (0.02 and 0.025 mm).....	115
Figure 4.5– XRD patterns of SLM NiTi samples produced by LP and MP parameters (Table 4.4) and two different layer thicknesses (a) 0.02 mm and (b) 0.025 mm	116

Figure 4.6– 2D profile imaged by an image probing sensor on the cut-section of an AM part. Several re-entrant features can be observed [90].....	118
Figure 4.7– CT reconstructed model of one NiTi sample (a); surface topography extracted from the CT volume (b) and 2D profile containing re-entrant features extracted from the surface topography (c)	118
Figure 4.8– Roughness measurements of SLM NiTi (Table 4.3) using optical microscope and focus variation methods	120
Figure 4.9– Surface topographies extracted form CT data of samples LP (a), MP (b) and HP (c).....	120
Figure 4.10– Example of surface profiles extracted from CT data of samples LP (a), MP (b) and HP (c)	121
Figure 4.11– Comparison of Pa values measured using focus variation microscope and X-ray CT. Maximum and mean Prf values are also reported as index of surface complexity	122
Figure 4.12– Scanning electron micrographs of SLM NiTi (according to Table 4.3) samples after polishing (P%: porosity percentage calculated by image processing applied on SEM micrographs)	123
Figure 4.13– Porosity analysis conducted on CT scanned samples LP (a), MP (b) and HP (c). The detected pores are colored based on their volume	124
Figure 4.14– XRD patterns of the SLM SS316L produced by different (a) laser powers and (b) scanning speeds.	126
Figure 4.15– Microhardness values of SLM SS316L parts as a function of (a) scanning speed and (b) laser power.....	128
Figure 4.16– (a) Microstructure of SLM SS316L in a cross-section parallel to the building direction (BD) - photo obtained through optical microscope and magnification 200x, (b) epitaxial growth of SLM SS316L – photo obtained through SEM and magnification 500x along BD	129
Figure 4.17– (001) pole figure and inverse pole figure of SLM SS316L produced by (a, b): 90 W and (c, d): 130 W power of laser	130
Figure 4.18– Support design for over angle surfaces	131
Figure 4.19– The effect of topology optimization on productivity of self-supported scaffolds	132
Figure 4.20–Ti6Al4V hollow samples with the same porosity (35%) and different pore shape and distribution produced by SLM	134
Figure 4.21– distribution of elastic stress in hollow NiTi FEM designs in uniaxial compression direction.	136
Figure 4.22– distribution of plastic strain in transverse direction of sample 1 according to Table	136
Figure 4.23– distribution of plastic strain in transverse direction of sample 5 according to Table	136
Figure 4.24– FEM stress-strain curves of Ti6Al4V hollow samples with different geometries and distribution of pores	137
Figure 4.25– stress-strain curves of Ti6Al4V hollow samples with different geometries and distribution of pores, uniaxial compression test (parameters same as FE modeling).....	138

Figure 4.26– regular porous scaffolds and related unitcells with (a) 35%, (b) 42% and (c) 56% porosity designed by Magics software, (d) 3 mm block support designed for scaffolds	139
Figure 4.27– stress-strain curves from uniaxial compression test of NiTi porous scaffolds (see fig) produced by SLM.....	140
Figure 4.28– (a) human bone biopsy (collaboration with medicine school, UNIPD), (b) positioning of bone biopsy in micro computed tomography for scanning	141
Figure 4.29– Biopsy comprising cortical and cancellous	142
Figure 4.30– (a) micro CT scanning of bone biopsy, (b) selection of unitcell in 2-D view, (c) 3-D view of selected trabecular unitcell	143
Figure 4.31– A structure of scaffold in substitution of bone tissues, which mimics the internal	145
Figure 4.32– applying different SLM regimes for boarder (MP) and internal (HP) in regular and natural trabecular scaffolds (a) S_{F1} , (b) $S_{F1.5}$, (c) $S_{T1.5}$ (Table 4.12).....	151
Figure 4.33– NiTi trabecular scaffolds based on natural and regular unitcells presented in Table 4.12 produced by SLM.	151
Figure 4.34– Surface view, regular and natural NiTi trabecular scaffolds (a) S_{F1} , (b) $S_{F1.5}$, (c) $S_{T1.5}$ (Table 4.12).....	151
Figure 4.35– (a) S_{nat1} , (b) S_{art1} (Table 4.13)	154

List of Tables

Table 1.1 – Products/parts produced by different techniques of micro manufacturing [3]	6
Table 1.2 – Typical methods/processes of micro-manufacturing [3]	7
Table 2.1– Stoichiometry ratio and specifications of NiTi alloy powders	25
Table 2.2– Characteristics of initial powders used for μ DMD of NiTi.....	26
Table 2.3 – μ DMD process parameters used in this research.....	31
Table 2.4– Scanning strategies used to produce NiTi cubes	34
Table 2.5– μ DMD process parameters input	35
Table 2.6 – μ DMD process parameters used for fabrication of NiTi porous samples	36
Table 2.7– CT scanning parameters for μ DMD parts	37
Table 2.8- Gas atomized NiTi powder impurity level	39
Table 3.1– Surface roughness of thin walls	55
Table 3.2– Overview of process parameters used for NiTi thin walls production ($\Delta Z=t$: layer thickness, NH: nominal height of thin wall).....	56
Table 3.3– NiTi powder batches produced by mechanical alloying of elemental powders. ...	60
Table 3.4– NiTi cubes produced by μ DMD and alloy powders presented in Table 3.4.	60
Table 3.5– The fundamental and superlattice peaks of NiTi B2 phase, Cu K α radiation [72]	66
Table 3.6– Inherent micro porosity analysis of NiTi thin walls using μ CT scanning	76
Table 3.7– Micro pore’s shape analysis of NiTi cubes (top surface) produced by different scanning strategies according to Table 2.4	82
Table 3.8– Surface quality of NiTi cubes	83
Table 3.9– Sa and Sz parameters evaluated by μ CT on the inner hole’s surfaces	96
Table 3.10– μ DMD process parameters in z direction according to heat decay model ($\lambda=1$)	101
Table 4.1- SLM process parameters used for production of dense NiTi in the literature.....	109
Table 4.2- Overview of scanning parameters used for SLM of NiTi	109
Table 4.3- Overview of proposal regimes of process parameters for SLM of NiTi	110
Table 4.4– Selected SLM process parameters regimes to obtain single phase NiTi	113
Table 4.5– Thermal properties of Ti6Al4V, Stainless steel 316 and Nitinol	117
Table 4.6– CAD designs of Ti6Al4V hollow samples with the same porosity (35%) and different pore shape and distribution	133

Table 4.7– elastic modulus (stiffness) of porous NiTi produced by SLM in comparison to other synthetic and natural materials	140
Table 4.8– Design of experiment, support design for NiTi scaffolds.....	144
Table 4.9– Support design for NiTi scaffolds.....	144
Table 4.10– Natural and regular unitcells according to the computed tomography of cortical and trabecular bones	147
Table 4.11– Design of SLM experiment, NiTi trabecular scaffolds (natural and regular)....	149
Table 4.12– NiTi natural and regular scaffolds based on the porosity of trabecular bone	150
Table 4.13– NiTi functionally porous scaffolds (natural and regular)	153

Nomenclature

SLM: selective laser melting

DMD: micro direct metal deposition

μ DMD: micro direct metal deposition

PF_u: upper plane of powder column in μ DMD process

PF_L: Lower plane of powder column in μ DMD process

RF_n: Nominal value of powder feeding rate

List of Publications

- [1] Saeed Khademzadeh, Nader Parvin, Paolo F. Bariani, *Production of NiTi alloy by direct metal deposition of mechanically alloyed powder mixtures*, International journal of precision engineering and manufacturing vol. 16, no. 11, pp. 2333-2338, 2015.
- [2] Saeed Khademzadeh, Simone Carmignato, Nader Parvin, Filippo Zanini, Paolo F. Bariani, *Micro porosity analysis in additive manufactured NiTi parts using micro computed tomography and electron microscopy*, Materials and Design, vol. 90, pp. 745–752, 2016.
- [3] Saeed Khademzadeh, Paolo F. Bariani, Stefania Bruschi, *Textural Evolution During Micro Direct Metal Deposition of NiTi Alloy*, Metals and Materials International, Vol. 24, pp. 24:869–876, 2018.
- [4] Saeed Khademzadeh, Filippo Zanini, Paolo F. Bariani, Simone Carmignato, *Precision additive manufacturing of NiTi parts using micro direct metal Deposition*, The International Journal of Advanced Manufacturing Technology, vol. 96, pp.3729–3736, 2018.
- [5] Jessica Rocco, Saeed Khademzadeh, Paolo F. Bariani, *the effect of selective laser melting process parameters on microstructure and textural evolution of stainless steel 316L alloy*, Euro PM 2018, conference, oral presentation, Bilbao, Spain, 2018.
- [6] S. Khademzadeh, F. Zanini, J. Rocco, K. Brunelli, P. F. Bariani, S. Carmignato, *Microstructural assessment and surface topography of NiTi parts produced by selective laser melting*, under review in journal of Materials and Design, 2018.

Chapter 1 Introduction

Design and manufacturing of complicated parts containing small features is in high demand for many industrial applications such as biomedical and microelectromechanical systems. Development of new manufacturing techniques capable to implement complicated micro features are under research. To address this industrial problem, many processes have been developed. However, most of these techniques such as investment casting have many limitations in design and implementation of complicated structures. To overcome the limitations of conventional manufacturing methods, additive manufacturing (AM) is being used ever more widely in industrial applications such as aerospace, automotive and medical engineering. In such applications use of AM allows for high geometrical complexities to be achieved with no additional cost being incurred in comparison to equivalent traditional manufacturing. AM technologies have been widely utilized with the purpose of producing complicated 3D components. Essential modifications have been implemented to make AM technologies suitable for microfabrication. Scalable AM technologies such as stereolithography, selective laser sintering, inkjet printing, and laminated object manufacturing (LOM) are the first group of the technology which have been regarded as a promising approach for 3D micromanufacturing. However, this class of micro-AM systems still suffers by some difficulties for microscale manufacturing as AM technologies have been developed mainly for normal-size fabrication. Some limitations of this group are due to its temperament and are same for both normal- and microsize manufacturing but some other limitations are for adaptation of this group for microsize manufacturing [1].

So far only a few studies have been conducted on development of laser aided additive manufacturing methods for fabrication of micro features. Systematic studies are needed to better understand the relationship between the fabrication parameters and the quality of products in order to be able to engineer the properties of laser manufactured components containing micro features such as lattice structures.

This thesis was designed to develop two main laser aided additive manufacturing methods (DMD and SLM) for fabrication of micro features through optimization of process parameters. Shape memory NiTi alloy system was selected as the main material since the production of this interesting biomaterial with conventional methods such as casting and machining has many difficulties.

1.1 Micro manufacturing, classifications and methods

The second industrial revolution started in the 1960s and reached its maturity towards the turn of the millennium. Emergence of microelectronics, computers, communication systems, knowledge-based industry and the information technology transformed the society which we are lucky to experience personally. However, in the 2nd industrial revolution, miniaturization was restricted to only two-dimensional electronic circuits, the primary function of those being manipulation of information. But it is slowly being recognized that three-dimensional miniaturization of devices and systems which physically interact with objects in the surrounding has far more potential to bring revolutionary changes in our society. It is predicted by many that economically viable technology to minimize 3D objects will form the basic foundation for the forthcoming 3rd industrial revolution [2].

Micro manufacturing has been raised based on increasing demand on micro products/systems and components such as MEMS (micro-electric-mechanical systems), micro-reactors, fuel cells, micro-mechanical devices and micro-medical components. These systems and devices are now popularly used in vehicles, aircraft, telecommunication and IT facilities, home appliances, medical devices and implants. Micro-manufacturing engineering is a general term which concerns a series of relevant activities within the chain of manufacturing micro-products/features, including design, analysis, materials, processes, tools, machinery, operational management methods and systems [3]. Several micro and nano manufacturing technologies have been developed including: laser ablation, plating, photolithography, lithography, electroplating, molding and chemical etching.

1.2 Additive manufacturing

The term additive manufacturing (AM) introduces all manufacturing processes involving the construction of artifacts starting from 3D models and by joining the raw material layer by layer. The term additive manufacturing has been created to present an opposition to the subtractive technological processes. Additive manufacturing was born by introduction of a stereolithography (SL) machine by 3D system company in 1987. Firstly, SL method was being used only for the fabrication of prototypes and visualization of designed models to help designers in design promotion. By this way, the designers could understand whether the designed component is suitable for the final application. Progress in accuracy of processes and also materials allowed engineers to construct functional components using AM technologies. From 1987 up to now, many AM technologies have been developed and with them, a large number of companies have been created for production of polymer components and with a little delay for metal products.

Laser aided metal additive manufacturing (LAMAM) is a general term for various rapid manufacturing techniques that use a high power laser beam to build or repair three-dimensional (3D) components layer by layer. Some of these techniques use powder bed as feeding method such as selective laser melting (SLM) [4], [5] and selective laser sintering (SLS) [6], while some others use powder injection coaxial with laser beam such as direct metal deposition (DMD) [7] and laser engineered net shaping (LENS) [8]. All of these techniques have the capability of building 3D components directly from CAD file.

1.2.1 Basic principles of additive technologies

Additive manufacturing steps are highly dependents of component complexity and AM process. In general, AM is an iterative approach but the number of steps varies by the technology. Some steps that can be considered common between all AM process are listed below:

CAD: all components can be produced only starting from a three-dimensional model, which can be drawn directly by software or can be obtained by scanning the component.

STL: almost all additive manufacturing machines accept an STL format file. This type of file describes the three-dimensional drawing built at CAD only on a geometrical level, forgetting any information concerning the model's history and data concerning its construction. The surface of the component is approximated with many triangles of minimum and maximum size chosen by the user through the software (Figure 1.2); this dimension is defined as the minimum distance between the plane on which the triangle lies and the surface that the triangle must represent. To discretize the component in such a way that the triangles are not visible during production, their size must be smaller than the resolution of the machine used for additive production.

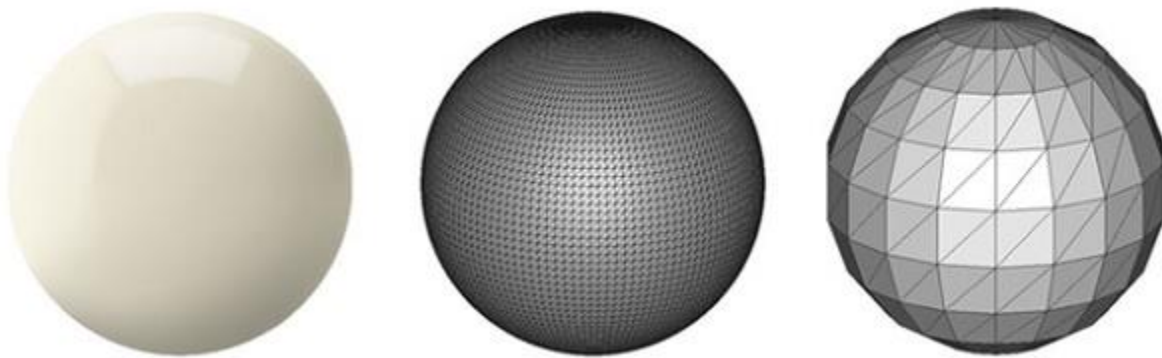


Figure 1.1– STL format designs with different dimensions of triangles [9]

Since the STL format is a pure geometric description of the surface, it is possible that during the conversion a series of errors occur, including:

- Incoming direction of the vectors identifying each triangle: this implies an incorrect distinction between the internal and external part of the component.
- Discontinuity between the triangles.
- Intersection between triangles.

These errors must be corrected before slicing. Many software, including those developed specifically for additive processes, can be used to correct the errors deriving from the

transformation into STL. Files that are not too corrupt can be automatically restored by the software, while in some cases it is necessary to correct the STL manually.

3. Machine instruction preparation: once the STL file of the component has been saved, it is necessary to define all the correct settings to proceed with the construction. Since this is a list of operations that is not same for all additive processes, we will not go into details, but in all cases, the parameters concerning the positioning of the component, making support structures, and the input energy must be defined. This step will be described in detail through the text for micro direct metal deposition and selective laser melting.

4. Construction: all the operations that must be performed once the STL file of the component is ready to be built. These operations are mainly carried out by an operator, even if many companies are trying to automate all the phases of pre and post process. At present, the operator will have to prepare the machine for a new process, for example cleaning, replacing the worn consumables components of the machine and positioning of the platform to build the new component.

5. Removal: after building the component, it must be extracted from the unmelted powders and support removal procedure from the sample and platform should be done.

6. Post-processes: the components obtained by additive manufacturing can be subjected to the subsequent finishing operations such as heat or thermochemical treatments or other specific operations for the final application.

Metal AM technologies have taken the manufacturing world over the last decade. Metal 3D printing is one of the most popular in the field of bioengineering. Unlike traditional manufacturing methods, which carve a product out of a block of material, additive manufacturing builds a solid and 3-D part layer upon layer. A CAD model guides the distribution of a layer of powder material, which is then fused together using a high energy source like laser or electron beam. Another layer is deposited on top of the first layer and fused, and the process is repeated until the formation of final part.

1.2.2 Additive Micro manufacturing

As the parts continue to become smaller and more complex (Table 1.1), it is harder for standard AM technologies to keep up with the more challenging shapes and tight tolerances. Therefore, manufacturers are eager to find additive manufacturing processes that can make high-precision parts at the sub millimeter scale, with tight tolerances.

Table 1.1 – Products/parts produced by different techniques of micro manufacturing [3]

Components/ Parts	Sample Geometry/ Features	Possible Enabling Techniques	Typical Part Materials	Processing Accuracy	Typical Products/ Applications
Surface 2.5D functionalized structures	Local features in hundred nanometers to 10s of microns	Hot embossing/coining/imprinting, ink-jetting, plating, direct writing, laser ablation, etc.	Polymers, glass, aluminum, copper, brass, steel, etc.	Several microns to nanometers	Micro-optical, fluidic devices, force transmit. surfaces, dies/molds, etc.
Lead frames	Various geometry, local features as small as ten microns, thicknesses vary, such as between 0.3 and 0.01 mm	Micro-stamping, with/without laser assistance, laser cutting, photo-chemical etching, etc.	Copper and alloys, nickel steel, etc.	Several microns or to 10% of the sheet thickness	Electronics products
Micro-pins	Diameters in 0.2–1 mm ranges, wall thickness in 50 to 200 microns possible, and tolerances <5 microns	Forward, and/or combined with backward extrusion, micro-shape rolling, micro-machining/EDM.	Various types of metals	Several microns to sub-microns	Various applications as IC carrier, micro-device assembly, electric contacts, etc.
Electro-thermal-mechanical actuator	2.5D/3D structural parts, various sectional geometries	Chemical etching and micro-stamping, laser cutting, efab.	SMA and other metal materials	Several microns	Micro-actuating devices
Micro-cups	Micro-cups, less than 1 mm in diameter, various thicknesses	Micro-deep drawing, micro-stamping, micro-spinning, micro-machining.	Molybdenum, copper, aluminum, steel	Several microns	Electron guns, pressure sensors, UV sensors, etc.
Micro-gears	Diameters of 1 mm or less, local features in 10s of microns	Micro-forging, micro-extrusion, micro-stamping, LIGA, micro-casting, PCE, micro-EDM, efab., etc.	Metals, polymers	Several microns to sub-microns	Micro-mechanical devices, watches
Shafts for micro-mechanical drivers	Less than 1 mm in diameters	Micro-extrusion, micro-machining/EDM.	Steels and alloys	Several microns to sub-microns	Micro-driving-devices, e.g. micro-spindles
Micro-screws, micro-cans	Diameters in 0.1–0.5 mm ranges	Micro-forging, extrusion, shape rolling, micro-machining.	Various metals	Several microns to sub-microns	Micro-devices, housing and assembly, etc.
Micro-gear shafts	Local features in 30–50 microns	Extruded with local heating, micro-radial extrusion, micro-machining, EDM.	Metals	Several microns to sub-microns	Micro-mechanical driving devices, watches

In old literature [3] and according to the way in which the components/products are to be made, micro manufacturing processes have been classified into subtractive, additive, forming, joining

and hybrid processes. In these classifications, micro additive manufacturing term has been applied to some surface coating and deposition processes such as CVD and PVD (Table 1.2).

Table 1.2 – Typical methods/processes of micro-manufacturing [3]

Subtractive processes	Micro-mechanical cutting (milling, turning, grinding, polishing, etc.); micro-EDM; micro-ECM; laser beam machining; electro beam machining; photo-chemical machining; etc.
Additive processes	Surface coating (CVD, PVD); direct writing (ink-jet, laser-guided); micro-casting; micro-injection molding; sintering; photo-electro-forming; chemical deposition; polymer deposition; stereolithography; etc.
Deforming processes	Micro-forming (stamping, extrusion, forging, bending, deep drawing, incremental forming, superplastic forming, hydro-forming, etc.); hot-embossing; micro-/nano-imprinting; etc.
Joining processes	Micro-mechanical-assembly; laser-welding; resistance, laser, vacuum soldering; bonding; gluing; etc.
Hybrid processes	Micro-laser-ECM; LIGA and LIGA combined with laser-machining; micro-EDM and laser assembly; shape deposition and laser machining; efab.; laser-assisted micro-forming; micro-assembly injection molding; combined micro-machining and casting; etc.

Nowadays, term additive manufacturing is being used specifically for the processes that produce a 3D object directly from a CAD drawing layer by layer which is basically different to the processes dedicated to 2D or 2.5D fabrications such as surface coating. The majority of micro manufacturing techniques are mostly limited to 2D or 2.5D production, and do not provide the versatility necessary to produce three-dimensional objects. Additive manufacturing is an advanced process with the capability to manufacture small and complex 3D parts directly from CAD models [1]. Some of the additive micro manufacturing processes are listed below:

1.2.3 MICA process

MICA freeform is an additive manufacturing process that leverages aspects of semiconductor manufacturing and rapid prototyping. It can fabricate millimeter-scale metal parts with micron-size features. The process is also capable of combining different metals into micro-composite structures that outperform single metals or alloys.

The MICA Freeform process involves three primary steps per layer. First, a fully-dense structural metal is electrodeposited onto a substrate in selected regions corresponding to the desired cross section of the part to be fabricated. Deposition occurs through apertures in a photoresist patterned using a sub-micron resolution photomask, in a method similar to that used in semiconductor fabrication facilities. After removal of the photoresist, a sacrificial metal is blanket-electrodeposited over the structural metal. Finally, both metals are planarized to yield a layer that is flat, planar, and of precisely-controlled thickness. The three steps are then

repeated for all layers required, after which a chemical etchant is used to dissolve the sacrificial metal, releasing the parts [10].

MICA Freeform can fabricate holes of any shape into a part as small as 40 microns in diameter. One of the biggest differences between MICA Freeform and other AM technologies, is that the MICA Freeform process creates dense, precise parts that do not require any infiltration or other finishing processes. Some of the MICA process products are shown in Figure 1.2.



Figure 1.2– MICA Freeform metal products containing micro features

1.2.4 Micro direct metal deposition (μ DMD)

Additive manufacturing with direct metal deposition concept is a newly developed manufacturing process. High processing speeds, no requirement of tooling and possibility to fabricate complex shapes are three important capabilities of this method [11]. Generally, in additive manufacturing using DMD concept, moving laser head heats and melts powder grains delivered from a coaxial powder feeding system. The material is deposited layer by layer onto the previous solidified layer and 3D object forms according to CAD file [12]. A schematic of DMD process is shown in Figure 1.3.

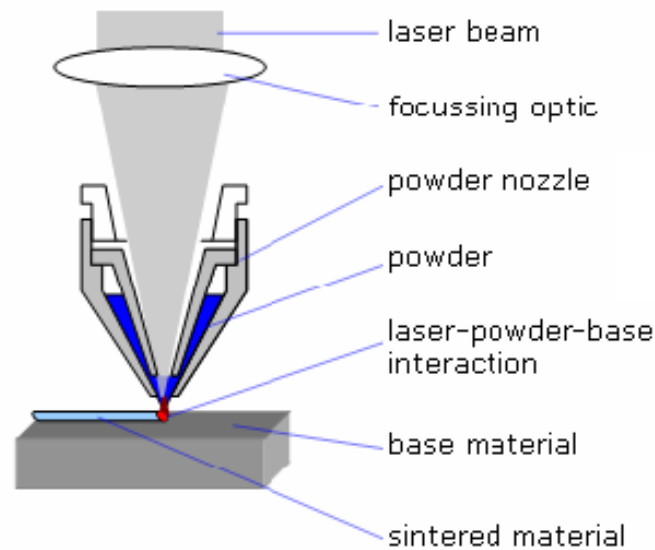


Figure 1.3– Schematic diagram of micro direct metal deposition system [13]

Much research work has been carried on the effects of DMD process parameters on dimensional accuracy and surface quality of additive manufactured parts [14]–[16]. The aim of those studies was to improve the quality of products and eliminate the successive subtractive processes. Power of laser, speed of scanning, powder feeding rate and z-increment are most important parameters that have been studied extensively. Moreover, there are two other important parameters that have significant influence on the quality of products. Zhu et al. [17] studied the effect of laser and powder defocusing on surface quality of thin walls produced by direct metal deposition. Reducing the scale of production from millimeter to micrometre can improve the quality of products, eliminate the post process machining and also increase the possibility to implement finer features.

Micro direct metal deposition (μ DMD) is an additive manufacturing process which uses DMD concept and can implement the smaller features thanks to specific process parameters such as a small laser spot diameter [13]. Micro direct metal deposition basically consists of melting and rapid solidification. Thus, porosity as well as heterogeneous microstructure are two main defects of μ DMD processed parts. In order to improve the mechanical properties of μ DMD processed parts, microstructure control should be considered [18], [19]. It is well understood that, strategy of scanning has a strong impact on grain structures of additive manufactured metallic parts produced by different processes [20]. A significant effect of tool path on grain

structure and texture of Nickel-based superalloy thin walls produced by DMD has been reported [21]. Texture and grain structure of the surface in additive manufactured metallic parts have the origin in heat transfer and related phenomena between the successive layers.

Increase in geometrical accuracy of an additive manufacturing method can create high quality products with fine features [22]. The diameter of laser spot usually controls the capability of a laser aided additive manufacturing process for micro manufacturing. Small laser spot may result in the formation of limited melt pool, which may in turn lead to fine and micro scale features in laser aided additive manufacturing [17]. On the other hand, decreasing the diameter of laser spot may inhibit 3D manufacturing due to insufficient melting rate. Micro manufacturing using SLM process has been examined by Hollander et al. [23]. By evaluating circular holes with a scanning electron microscope (SEM), they showed that there is about 30% deviation to designed models in Ti6Al4V components produced by SLM. Since metal powder is prepositioned in SLM method, the high level of laser input energy melts the excess powders inside the predesigned holes and decreases the accuracy of micro manufacturing. Using equiaxial powder injection coupled with narrow laser beam can increase the accuracy of laser aided additive manufacturing process.

1.2.5 Selective laser melting (SLM)

Selective laser melting is one of the new additive manufacturing techniques that emerged in the late 1980s and 1990s. During the SLM process, a product is formed by selectively melting successive layers of powder by the interaction of a laser beam. Upon irradiation, the powder material is heated and, if sufficient power is applied, melts and forms a liquid pool. Afterwards, the molten pool solidifies and cools down quickly, and the consolidated material starts to form the product. After the cross-section of a layer is scanned, the building platform is lowered by an amount equal to the layer thickness and a new layer of powder is deposited. This process is repeated until the product is completed (see Figure 1.4). This layer-by-layer process was first used to produce prototypes, but the trend is towards direct manufacture of components because of its ability to net-shape manufacture complex structures from a CAD model and a wide range of materials without the need of expensive tooling and machining so that the delay between

design and manufacture is minimised. Another advantage is that the powder is melted only locally by the laser and the rest of the powder can be recycled for further fabrication.

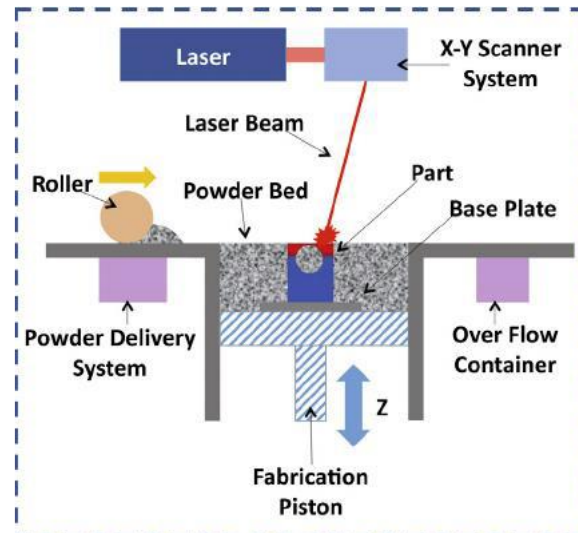


Figure 1.4– The schematic of powder bed fusion-laser process [24]

Development of SLM process for microfabrication is restricted by process parameters like laser spot diameter and materials specifications like powder size. Small laser spot diameter and fine powder particles facilitate microfabrication via SLM. Moreover, the nature of the SLM process causes melting of excess powders that exist near to laser scanning track. This phenomenon increases the deviation of SLM parts to predesigned models. Therefore, implementation of micro features needs an exact control of SLM process parameters.

1.3 Fabrication of NiTi component with micro features

1.3.1 History of shape memory alloys

Equiatomic phase of Ni-Ti alloy which named “Nitinol” has especial and unique physical and mechanical properties such as shape memory effect, superelasticity and excellent biocompatibility [25]. In the early 1960s, Buehler and his co-workers at the U.S. Naval Ordnance Laboratory discovered the shape memory effect in an equiatomic NiTi, which can be considered as a breakthrough in the field of shape memory materials [26]

1.3.2 NiTi shape memory alloy (shape memory effect, superelasticity)

Near equi-atomic phase of nickel–titanium alloy system has unique shape-memory and superelastic properties [27]. Good ductility, corrosion resistance and biocompatibility of NiTi introduce it as a functional material for many engineering applications including smart structures, dental and bone implants [28], [29].

Shape memory alloys (SMAs) are a unique class of metal alloys that are capable of converting thermal energy into mechanical work. After a mechanical deformation, SMAs can remember their original shape when they are heated to a certain temperature or they can recover a large amount of strain if they deform in a certain temperature range. SMAs in fact, undergo a solid to solid diffusion-less phase transformation and as consequences can produce very high recoverable shape changes [30]. Martensitic transformation is a solid-state transformation and an example of a displacive (diffusion-less shear transformation) transition, in which there is the cooperative motion of a relatively large number of atoms, each being displaced by only a small distance and atoms move in an organized manner relative to their neighbours.

1.3.2.1 Shape Memory Effect (SME) and superelasticity (SE)

As stated before, "Shape Memory" describes the effect of restoring the original shape of a plastically deformed sample by heating it. This phenomenon results from a crystalline phase change known as "thermoelastic martensitic transformation". At temperatures below the transformation temperature, shape memory alloys are martensitic. In this condition, their microstructure is characterized by "self-accommodating twins". The martensite is soft and can be deformed quite easily by de-twinning (Figure 1.5). Heating above the transformation temperature recovers the original shape and converts the material to its high strength austenitic condition [31]. The complete transformation cycle is characterized by the following temperatures: austenite start temperature (A_s), austenite finish temperature (A_f), martensite start temperature (M_s) and martensite finish temperature (M_f).

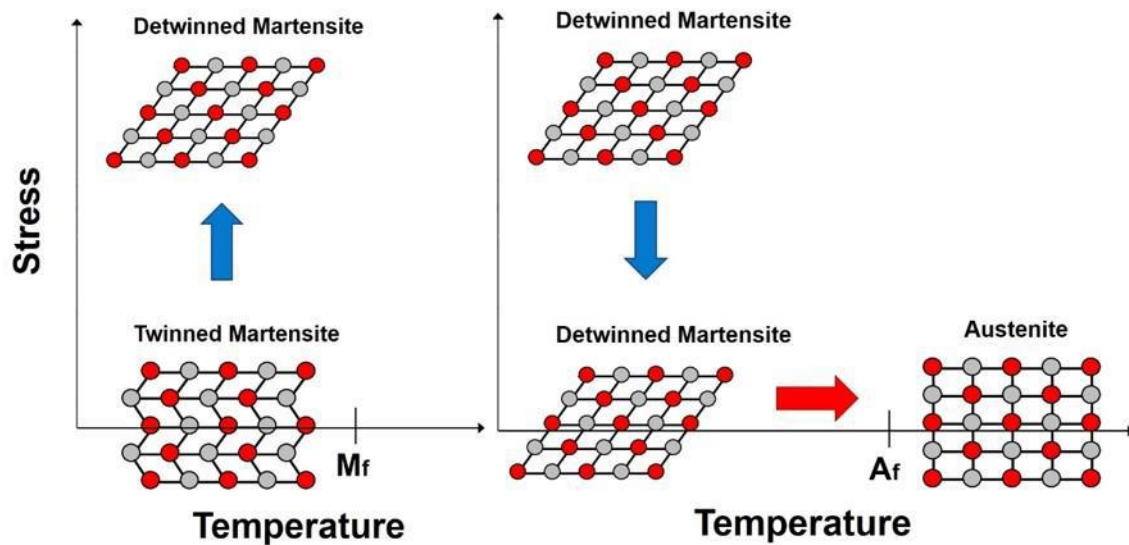


Figure 1.5– Schematic of shape memory effect of SMAs [32].

If a stress is applied to a shape memory alloy in the temperature range above A_f , martensite can be stress-induced. Less energy is needed to stress-induce and deform martensite than to deform the austenite by conventional mechanisms. Up to 10% strain can be accommodated by this process (single crystals of specific alloys can show as much as 25% pseudoelastic strain in certain directions). As austenite is the thermodynamically stable phase at this temperature under no-load conditions, the material springs back into its original shape when the stress is no longer applied. This extraordinary elasticity is also called pseudoelasticity or transformational superelasticity.

1.3.3 NiTi fabrication methods

Fabrication of NiTi alloys is exceedingly difficult, due to the compositional control requirements during the process. The structural, and functional properties of NiTi are highly fabrication and process parameter dependent since these properties are very sensitive to nickel-titanium ratio, picked up impurities and formed secondary phases. In addition, poor thermal conductivity and enormous elasticity of the alloy which leads to increase die or roll contact and eventually results in frictional resistance, make machining of the NiTi extremely challenging. Figure 1.6 shows major problems of NiTi machining. Therefore, each step in the fabrication of NiTi parts requires a deep understanding of its effects on performance and quality of final

Product. The most common fabrication routes for NiTi alloys will be discussed briefly in following sections.

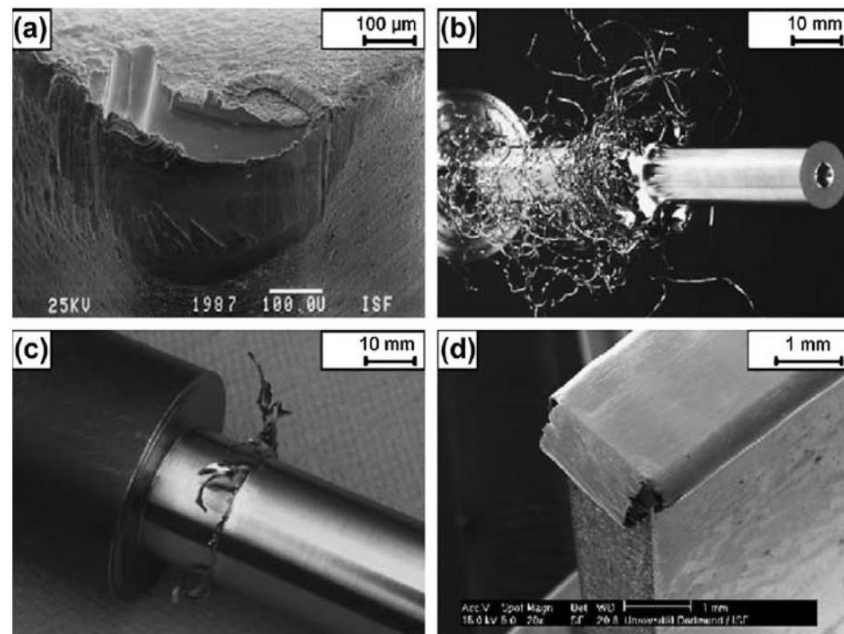


Figure 1.6– Major drawbacks in machining NiTi shape memory alloys: (a) high tool wear; (b) undesirable chip formation; (c) formation of burrs after turning (d) and grinding [33]

Although there is no single recipe for the production of NiTi ingots, conventionally Vacuum Arc Melting (VAM) or Vacuum Induction Melting (VIM) followed by a hot working process and machining to the final shape. To minimize the possibility of contamination during melting, an inert gas working atmosphere is used [34]. However, titanium is highly reactive, therefore, high-temperature processing such as melting and alloying is always accompanied by formation Ti-rich phases and higher impurity level. Figure 1.7 illustrates a laboratory setup for VIM processing of binary NiTi ingot metallurgy in a graphite crucible and starting with pure elemental Ni pellets and Ti rods.

After melting, the Nitinol ingot is usually forged and rolled into a bar or a slab at elevated temperatures. Extrusion of Nitinol billets and tubes at temperatures between 850°C and 950°C has been experimented [10]. Such hot working processes break down the cast structure and improve mechanical properties. Optimal hot working temperatures appear to be around 800°C where the alloy is easily workable and the surface oxidation in air is not too severe. Following

hot working, Nitinol alloys are cold worked and heat-treated to obtain final dimensions with desired physical and mechanical properties.

Cold working of Nitinol is quite challenging because the alloy work-hardens rapidly. It requires multiple reductions and frequent inter-pass annealing at 600-800° C until the final dimension is obtained. Round wires are produced by die drawing processes. Rectangular wires can be manufactured by drawing round wires while flat wires are typically produced by cold rolling. Comparing to those of rolled flat wire, the dimensions of drawn rectangular wire are much more tightly controlled [35]. Additionally, as it was mentioned, machining of NiTi is very challenging [26] and the significant heat generation throughout a machining process can affect the functional properties of fabricated parts, in addition, conventional processing routes do not allow for the production of porous NiTi [51]. Laser machining; electro-discharge machining (EDM) and photochemical etching processes are used to fabricate Nitinol components such as stents, baskets and filters. In particular, laser machining has become the preferred process for the manufacture of Nitinol tubular stents. Modern laser cutting machine using a pulsed Nd:YAG laser and equipped with a CNC motion control system offers high speed, high accuracy and the capability for rapid prototyping. Drawbacks are the occurrences of heat-affected zone (HAZ) and micro cracks. Powder metallurgy methods are generally used to fabricate porous NiTi components.

It can be concluded that, machining of NiTi by conventional methods is difficult due to rapid work hardening and superelasticity of Nitinol [36]. Therefore, powder metallurgy methods, such as conventional powder sintering [37] and self-propagating high temperature synthesis (SHS) [38] are utilized to fabricate NiTi parts.

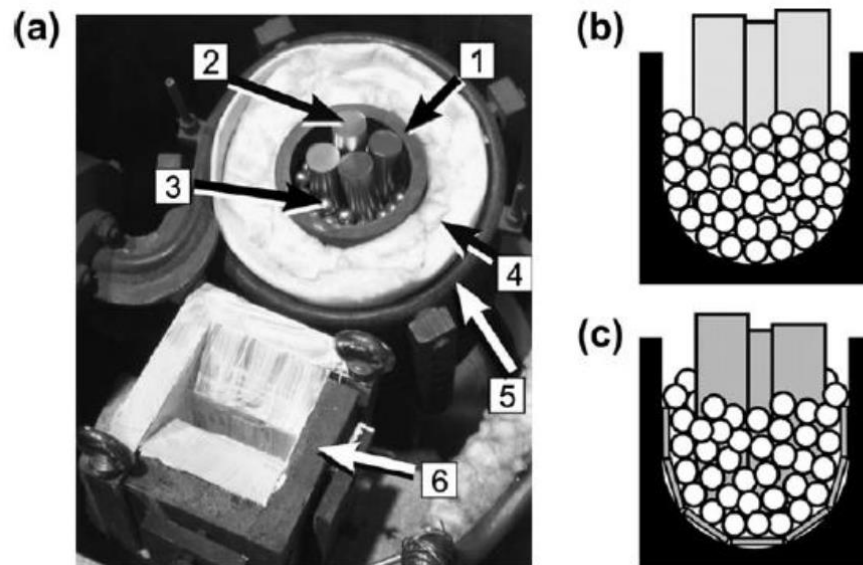


Figure 1.7– (a) Laboratory setup for VIM processing of binary NiTi (1: graphite crucible; 2: Ti rods; 3: Ni pellets; 4: isolation; 5: water cooled copper coil; 6: mold); (b) schematic illustration of the crucible filling with Ni pellets in contact with the Graphite

1.3.4 Additive manufactured NiTi alloys

Recently, additive manufacturing has been applied to produce NiTi parts from NiTi powder. AM is able to make three-dimensional objects from CAD models. Bormann et al. [39] used SLM to produce complex-shaped NiTi micro-structures. Shishkovsky et al. [40] obtained optimized process parameters to produce NiTi bulk samples with relative bulk density above 97% of the solid state. Two main approaches have been studied to fabricate single phase NiTi by laser melting. The former approach utilizes pre-alloyed nitinol powder, which is quite expensive. With the latter approach, Ni-Ti powder mixture is utilized and due to reactions almost out of control developing during the laser melting, unwanted intermetallic compounds such as NiTi₂, NiTi₃ and Ni₃Ti can be generated. Shishkovsky et al. [40] produced NiTi+Ti₂Ni mixture after laser controlled synthesis and then they transformed it into NiTi phase after additional thermal heating. Mechanical alloying as a well-known, simple and affordable powder metallurgy method is one of the successful fabrication methods of intermetallic

compounds. Mousavi et al. [41] reported that B2–NiTi phase can be obtained by high energy mechanical alloying of equi-atomic Ni-Ti powder mixtures.

Saedi et al. [42] reported the effects of solution annealing and subsequent aging on shape memory response of Ni-rich Prealloyed Ni_{50.8}Ti_{49.2} alloys fabricated by selective laser melting. They found that transformation temperatures, transformation behavior, strength, and recoverable strain are highly heat treatment dependent. Superelasticity with 95% recovery ratio with 5.5% strain in the first cycle and stabilized superelasticity with a recoverable strain of 4.2% after 10th cycle has been achieved by Saedi et al. in 2016. In another research, Saedi et al. [43] presented the shape memory behavior of SLM fabricated and solution annealed Ni_{50.8}Ti_{49.2} alloys. Results were compared to the initial ingot that was used to fabricate powders. They revealed that that SLM method and post heat treatments can be used to tailor the microstructure and shape memory response.

Most of the processes which have been used up to now have limitations to reduce the edge size of products because of the nature of lasers such as the diameter of focal point and consequently the width of the melt pool. The second problem is related to the nitinol powder as a starting material. In some previous researches, commercially pre-alloyed nitinol powders were used which is quite expensive and in some others, simply mixed Ni and Ti powder were used which caused to produce unwanted intermetallic compound such as NiTi₂, NiTi₃ and Ni₃Ti [40], [44].

1.3.5 NiTi porous scaffolds for biomedical application and bone printing

1.3.5.1 Macro structure of bone

The adult skeleton contains 206 bones, and has a dry fat-free mass 6-7% of total body mass. There are two main types of bone based on the amount of porosity. Dense bone which has low-porosity (5-20%) and forms the outer layer of bones and usually called cortical bone because it is located at the cortex. Moreover, Cancellous (spongy or trabecular) bone forms the internal part of bone. The porosity cancellous bone is typically 75-95%. The space is filled with red marrow, which is responsible for the creation of blood cells. Cancellous bone looks like a scaffold structure. The arms connecting the nodes of cancellous bone are termed trabeculae.

Trabeculae have a wide range of shapes, but are most often 0.1 to 0.2 mm of diameter and 1 mm of length.

1.3.5.2 Micro structure of bone

At the microscopic level cortical bone is composed of osteons running down the longitudinal axis of the bone. Each osteon is a cylindrical unit composed of concentric layers (lamellae) of bone tissue. At the centre of the osteon is a hollow core, the Haversian canal, which provides a passageway for blood vessels and nerves. The Haversian canals are connected transversely by Volkmann's canals, creating a network throughout the bone. Osteons have an outer diameter of roughly 0.2-0.3 mm, and an inner diameter of about 0.05 mm. The lamellae range in thickness from 3 to 10 microns. All of the structures are shown (not to scale) in Figure 1.8.

Compact Bone & Spongy (Cancellous Bone)

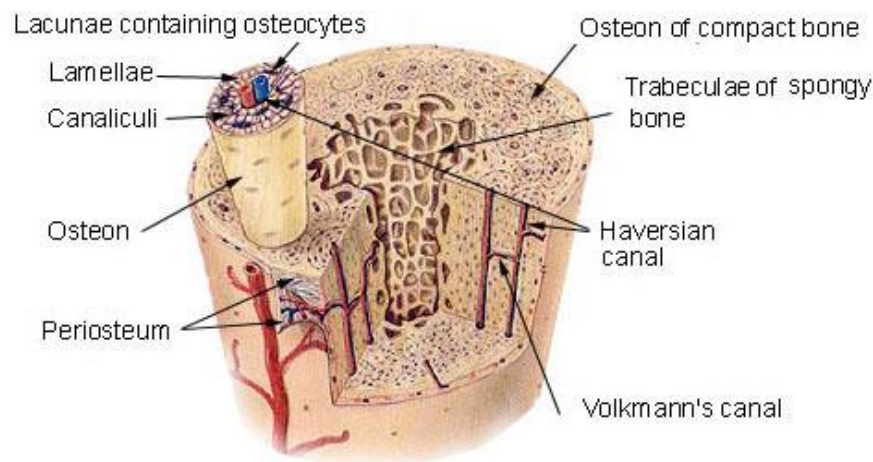


Figure 1.8– Macro and microstructure of cortical and cancellous bone

Trapped between the lamellae are osteocytes, mature bone cells. The space they reside in is called a lacuna, and is about 8 microns in the long axis, but varies from 3-20 microns. The lacunae are connected via a network of narrow passageways termed canaliculi. They are about 225 nm in width, and vary in size depending on whether they are circumferential (between lamellae) or radial (crossing lamellae). Cancellous bone, like cortical bone, is composed of lamellae. Unlike in cortical bone, the lamellae are not arranged into osteons. They form irregular patterns just a few layers thick. Aside from their arrangement, the lamellae themselves

are the same in trabeculae and osteons. The load-bearing extracellular material of bone is essentially the same regardless of where it is found. The material is a composite of organic proteins and inorganic mineral (hydroxyapatite: $\text{Ca}_{10}(\text{PO}_4)_6(\text{OH})_2$). The proteins are 90% collagen, with type I collagen fibers being the dominant variety. The fibers are oriented in the same direction within a given lamella, but lamella orientations differ, not unlike the layers in a sheet of plywood. Collagen has a low elastic modulus (around 6 GPa), but it has a large strain at failure, making it tough. Bone mineral is stiff and brittle, and it accounts for three fourths of dry-bone weight. Single crystals of hydroxyapatite have a modulus of 54-79 GPa. (For comparison, the Young's modulus of aluminum is 70 GPa.) The modulus of bone tissue fluctuates based on patient, anatomical site, and orientation, but generally falls around 10-20 GPa. The failure stress varies from ~50MPa in tension perpendicular to the collagen fibers, to ~190 MPa for compression parallel to the fibers. It is important to bear in mind that when mechanical properties are reported for cancellous bone they are often given at the apparent level, which treats the entire structure of the bone like its own homogeneous material. The resulting values for Young's modulus and strength are drastically reduced from the material level due to the reduced volume fraction.

1.3.5.3 Production of porous scaffolds mimicking the architecture of bone

Porous scaffolds based on biomaterials such as Calcium Polyphosphate (CPP) have been designed and produced using conventional powder metallurgy processes such as space holder sintering (SHS). Wang et al. [45] have designed a biodegradable scaffold based on mimetic a natural bone tissue morphology with a porosity gradient structure. They suggested that this biodegradable and porosity-graded scaffold may be a new promising scaffold for loaded bone implant. Figure 1.9 depicts that conventional powder metallurgy methods have limitations in mimicking the architecture of bone and consequently inhibits the bone ingrowth. It can be attributed to the difference of mechanical and microstructural properties of the SHS porous scaffolds to the real bone.

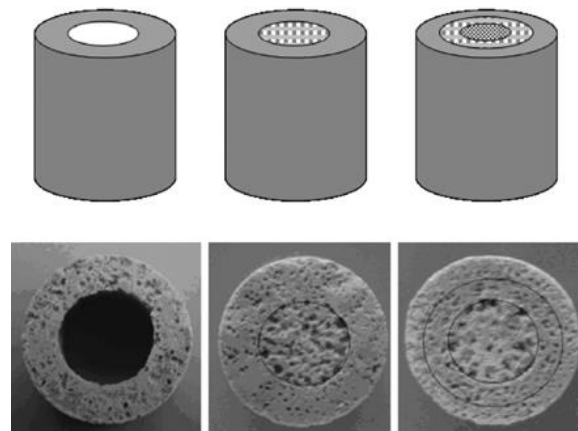


Figure 1.9– CPP porous scaffolds with a hollow centre and different graded porous layers [45]

Metal additive manufacturing processes can implement bio-inspired porous scaffolds thanks to versatility of such methods. Production of customized implants based on computed tomography of natural bone is known as a promising method [46].

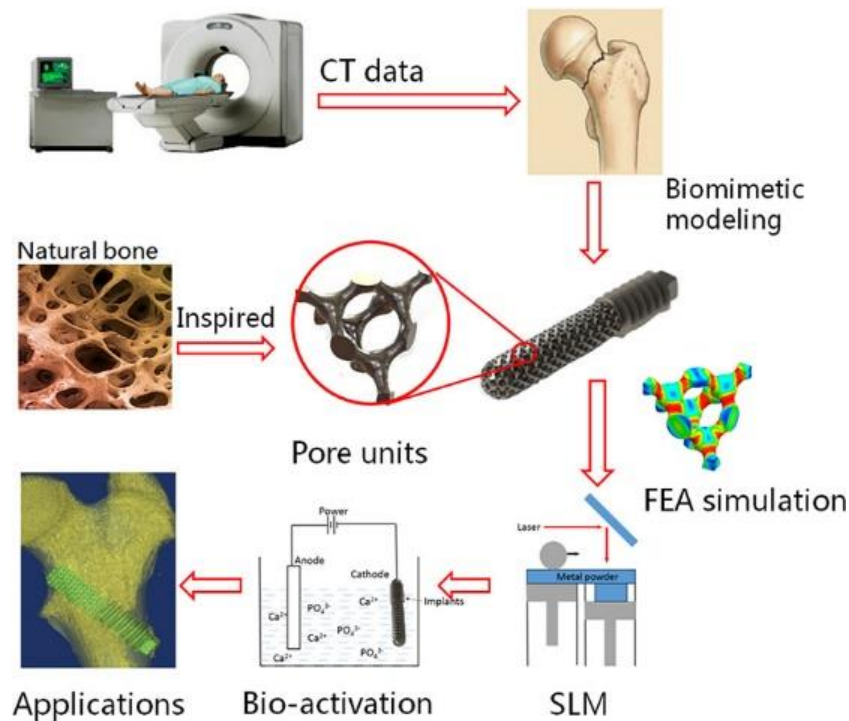


Figure 1.10– Process map for production of bio-inspired implants using SLM and regular unitcells

Zhang et al. [46] have produced novel porous architectures with diamond lattice pore structure from Ti6Al4V alloy by SLM. They examined the biocompatibility and repair effect of Ti porous implants by in vivo experiments. They reported new generated bones embedded and fitted into the designed porous implants after design optimization of scaffolds. Mohsen Taheri Andani et al. [47] produced near equiatomic NiTi shape memory alloys in dense and designed porous forms by SLM. They analysed the effects of regular pore's morphology on mechanical responses. They also reported good shape memory effect with a recoverable strain of about 5% and functional stability after eight cycles of compression in dense and porous NiTi alloys.

Porous metallic implants are promising due to their inherent low elastic modulus which is close to the stiffness of real bone. Moreover, porous structure promotes osseointegration in fabricated implants [48]. Generally, orthopaedic porous scaffolds should mimic the morphology, properties and microstructure of real bone which includes micro (<20 μm) and macro (>100 μm) pores [49].

Different methods exist for porous materials fabrication. Some methods such as casting, vapour deposition and especially additive manufacturing, allow a greater control over pore size and distribution. By these methods, open-cell porous structures are possible to be fabricated. On the other hand, there are other methods such as decomposition of foaming agents in either molten or powder metal matrices, which allow lower control over the characteristics of pores. Using these methods result in close-cell porous structures [50].

Many works have been conducted on production of porous scaffolds with macro pores using additive manufacturing methods such as selective laser melting [51], [52] and laser engineered net shaping [8], [53]. In additive technologies, macro pores are possible to implement using computer-aided designs. In addition, two different categories of micro pores can be obtained in laser melted parts. Melting process can cause the formation of the first category of micro pores. We use the term *inherent micro porosity* for the micro pores that are formed by melting process. This kind of porosity is non-controlled and substantial. Also, we use the term *controllable micro porosity* for pre-defined micro pores which can be manipulated by change in hatch distances or strategy of scanning as two main important process parameters in laser melting. Orthopaedic implants with inherent and controllable micro porosities can be fabricated by μDMD due to the specific process parameters of this technique. Control over the

architecture of micro pores is essential for porous scaffolds to serve as a bone implant [54], [55]. An evolution from random distribution of micro pores to pre designed porosity based on specific process parameters is important to control the functional behaviour of porous scaffolds. Regular architecture of micro pores permits cells to be seeded in the core much more readily than random architecture scaffolds [56]. Porosity, spatial distribution and morphology of micro pores have impact on mechanical and biological properties of porous implants. Design of micro pores inside the materials for biomedical application is still under research. It is possible to control micro pore's percentage by adjusting of process parameters. Despite there is no direct control on inherent micro pore's shape, it is possible to indirectly control the predefined micro pore's shape by changing process parameters such as hatch distance and scanning strategy as demonstrated in this research.

As stated before, production of micro features such as bony like porous structure with additive manufacturing is still under research [57], [58]. Porous nitinol with pore size of 100-500 μm is suitable for biomedical implants and allows human tissue ingrowth and body fluid transmission [59]. A great deal of researches has been conducted on production of porous nitinol by macro additive manufacturing processes such as selective laser melting [60], direct metal deposition [44], or laser engineered net shape [40]. There are two major problems in production of bone implants from nitinol by additive manufacturing. The first one is that, real bone structure consists of wide range of pore sizes from a few microns (micro pores) to some hundred microns (macro pores).

1.4 Objectives and technical approach

As stated before, essential modifications should be implemented to make AM technologies suitable for microfabrication. Primary objective of this thesis can be summarized in optimization of μDMD and SLM process parameters aiming fabrication of micro features and complicated parts.

Laser based metal AM systems still suffer by some difficulties for microfabrication as these technologies have been developed mainly for normal-size fabrication. Some limitations of this group are for elimination of unwanted microstructural phases in multi-phase materials.

Implementation of micro features needs different sets of parameters during the process. Optimization of process parameters of both techniques such as laser power, scanning speed and hatch distances for NiTi alloy system and quality control of NiTi parts were defined as secondary objectives.

NiTi has been presented as a promising material at porous implant application. Complicated architecture of porous biomaterials and NiTi current manufacturing difficulties makes this alloy an interesting candidate material for AM technology. This thesis was mainly defined based on the development of existing laser aided additive manufacturing processes for micro manufacturing of NiTi parts.

In the first part of this thesis, μ DMD with specific process parameters was developed to reduce the minimum size of additive manufactured features and make this method more suitable for implant production since a combination of macro and micro pores is needed. Mechanical alloying as a well-known, simple and affordable powder metallurgy method was used to produce NiTi alloy to overcome the problems of starting material. The development of texture and microstructure has been investigated in μ DMD processed NiTi cubes focusing on the influence of scanning strategy. For the first time and in this research, a comprehensive study was carried out on micro porosity analysis in μ DMD parts.

Selective laser melting is a robust metal additive manufacturing technique for generation of complicated geometry using a high-energy laser beam. Elimination of unwanted secondary phases after SLM of NiTi has always been an important research topic in recent years. In the second part of this research, the effect of SLM process parameters on phase composition, porosity and surface topography of NiTi parts has been studied using different techniques, such as X-ray diffraction, scanning electron microscope and micro X-ray computed tomography. Introduction of different SLM regimes to obtain the single phase B2-NiTi by SLM technique is one of the most important objective of this part. Finally, and based on the results, SLM technique was examined as a fabrication method for bone printing from metallic materials such as Ti alloys and NiTi.

This thesis includes four chapters. In chapter 1, an introduction and literature review about micro-manufacturing, additive micro manufacturing and different methods for fabrication of

NiTi parts are presented. Chapter 2 summarizes all experimental procedures used in this research. Obtained results of this thesis are divided into two main categories based on two different used techniques. Chapter 3 presents a comprehensive study on micro direct metal deposition of NiTi alloy including optimization of process parameters, quality control of products, design, and manufacture of micro features in NiTi and Ti parts. Chapter 4 is dedicated to the results and discussions on selective laser melting process in terms of quality control of products, optimization of process, design, and manufacturing of lattice structures from NiTi and stainless steel 316L alloys. Chapter 4 ends with a presentation of a novel technique for bone printing using SLM technique.

Chapter 2 Experimental procedure

This chapter describes details on the fabrication methods and experimental procedures employed for investigation of the μ DMD and SLM NiTi samples. All of the presented results of the current work have been performed at the Te. Si Laboratory at the Industrial Engineering Department of the University of Padua.

2.1 Experimental procedure of μ DMD process

2.1.1 Preparation of NiTi alloy powder

For μ DMD process, Nickel-Titanium alloys were produced by high energy mechanical alloying of the pure Ni and Ti elemental powder as presented in Table 2.1. Characteristics of the elemental powders used to manufacture alloy powder are given in Table 2.2.

Table 2.1– Stoichiometry ratio and specifications of NiTi alloy powders

Powder	Ni (at %)	Ti (at %)	Milling time (h)	Heat treatment
A	50	50	4	-
B	50	50	8	-
C	50	50	10	-
D	50.8	49.2	10	-
E	50.8	49.2	10	1050°C, 8h

Table 2.2– Characteristics of initial powders used for μ DMD of NiTi

Powder	Nickel	Titanium
Particle size [μm]	10-100	200-800
Purity [%]	99.99	99.95

Figure 2.1 shows the morphology of Titanium and Nickel starting powder materials respectively. The Ti powder particles were irregular and Ni powder particles had near spherical shape.

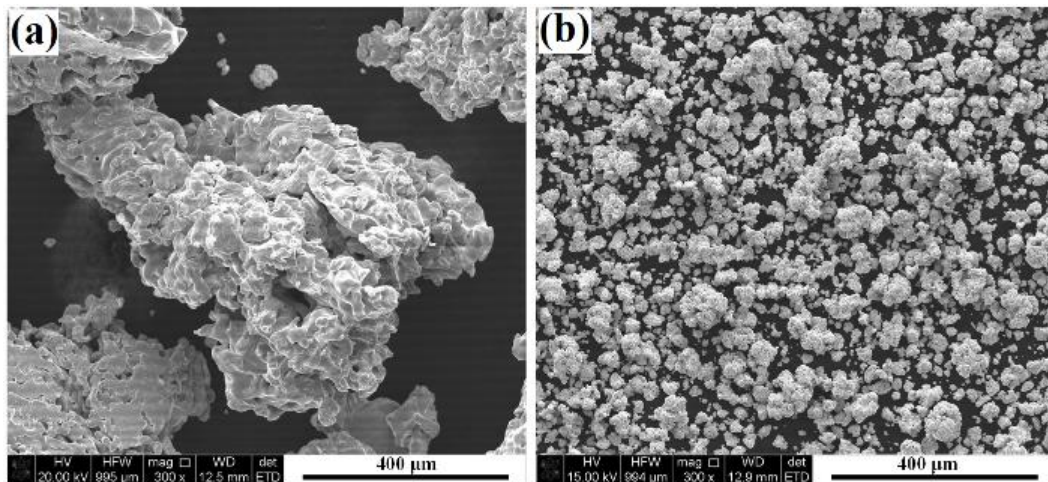


Figure 2.1– Scanning electron micrographs of starting materials, (a) Titanium powder particles, (b) Nickel powder particles

Mechanical alloying (MA) was carried out in a SPEX high energy shaker mill (8000M mixer/mill). In all MA runs, the ball to powder weight ratio was 10:1 and the bowl rotation speed was approximately 1200 rpm. Ni and Ti powder mixtures were milled under Ar atmosphere nominally at room temperature. Mechanical alloying produced flatten powder particles which weren't suitable for laser melting due to the problems associated with flowability. Therefore, after milling up to 8h, sieving process was carried out on milled powders and rounded powder particles in the range of 35 ± 5 microns were obtained. X-ray diffraction analysis depicted that, a semi amorphous structure with chemical composition near to austenitic NiTi forms after 8h of milling time (see Figure 2.2).

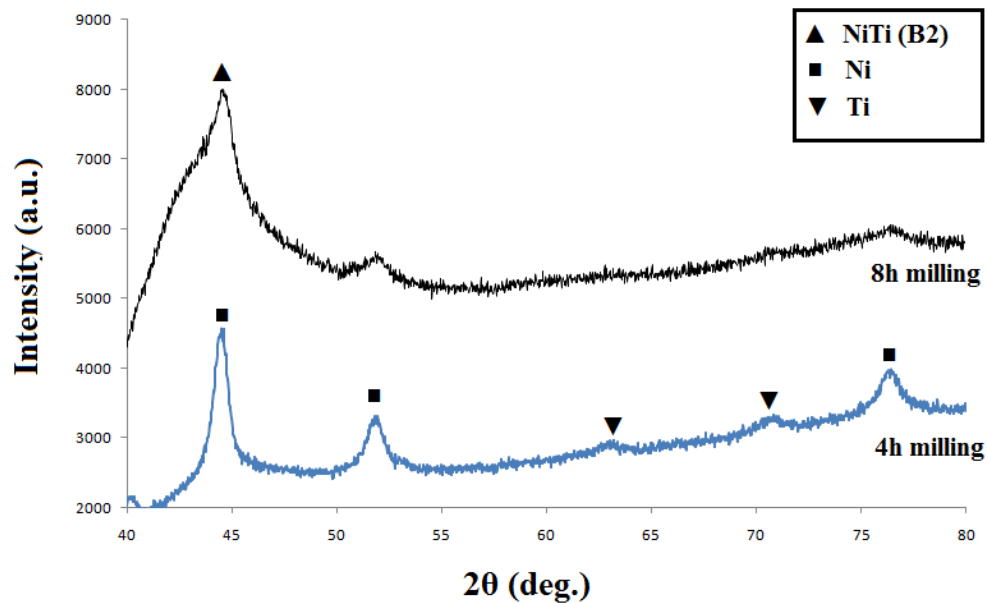


Figure 2.2– X-ray patterns of $\text{Ni}_{50}\text{Ti}_{50}$ after 4h and 8h of milling

2.1.2 Aluminium-Titanium-Niobium alloy powder

Mechanically alloyed Al-Ti-Nb powder with irregular shape and 28-35 μm of powder particles was used as a starting material for μ DMD of multi-section structures. The powder was Al 40-48 at%, Nb 3-5 at %, balance Ti 47-57 at% from MBN company, Italy.

2.1.3 Micro direct metal deposition process

MSL50 micro direct metal deposition machine (Manudirect company, Italy) with a continuous fiber laser (YLM-100-WC, IPG, wavelength: 1070 nm), maximum power of 100 W and 30 μm laser spot diameter was used in this project to produce NiTi objects. The schematic diagram of the μ DMD system and MSL50 machine are presented in Figure 2.3. This machine is equipped with a coaxial powder feeder system controlled in real time with 11 powder injectors, a three axis worktable and an atmosphere control processing chamber. Small heat affected zone is one of the advantages of coaxial injection systems and also using coaxial injection, multidirectional production will be possible due to the radial symmetry between the laser beam and the powder flow. The powder particles are delivered to the molten pool through the 11-line coaxial powder streams using Argon carrier gas.

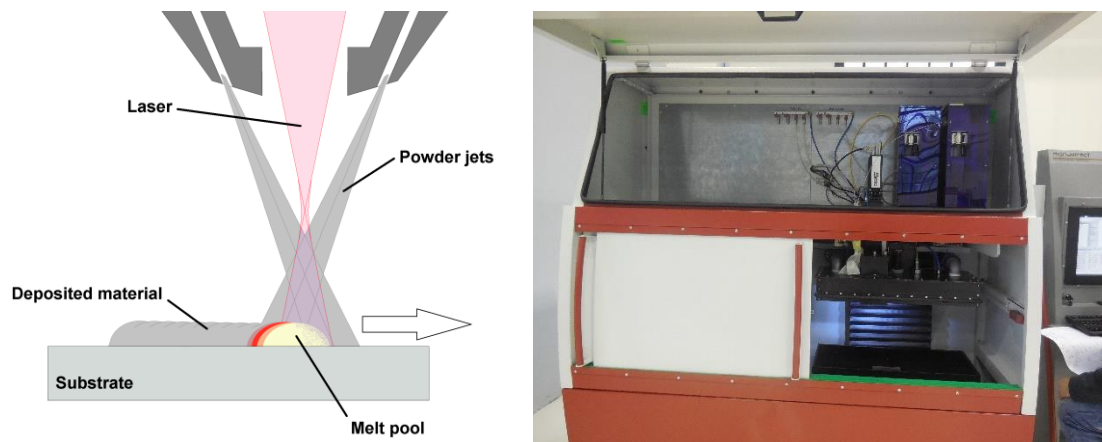


Figure 2.3– Schematic diagram of μ DMD process (nozzle shape: conic, lower width of the nozzle: 6 mm, number of injectors: 11, injector’s diameter: 0.5 mm)

2.1.3.1 Powder feeding system

The powder feeding systems (called “micro-LS” powder feeding system) installed on the MSL50 machine is a pneumatic feeding system and it was designed to ensure a constant low powder supply on the sintering area during the micro DLMD process. The concept of the system is suitable to create a homogeneous fine solid gas dispersion of the powder particles (called “particle aerosol”) on the carrier gas (see Figure 2.4).

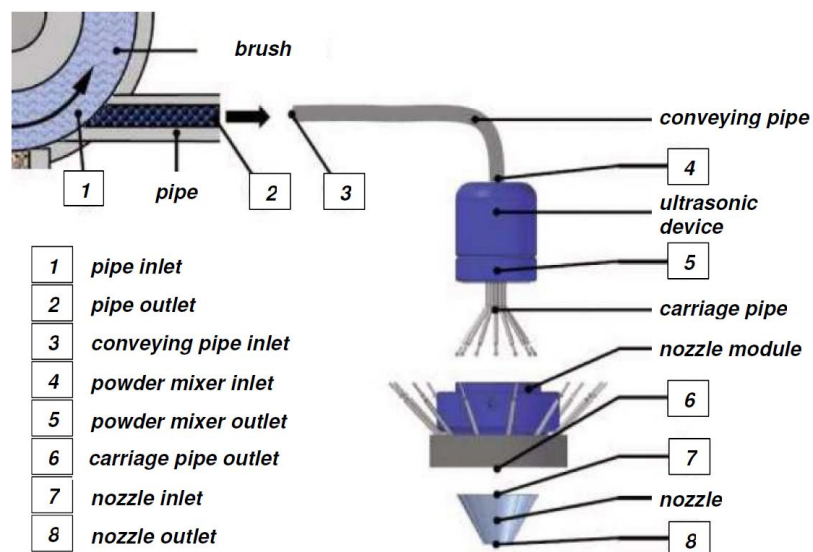


Figure 2.4- Components of powder feeding system, MSL50 machine, Manudirect

The nozzle installed in the MSL50 has a special design that ensures a powder deposition coaxial to the laser source employed during the process (see Figure 2.5). The conical shape of the nozzle gives to the powder-gas mixture coming out from the outlet a nominal inclination that allows the formation of a powder cone.



Figure 2.5- Coaxial nozzle used for powder injection in MSL50 machine, Manudirect

A new control software (CALD) has been developed in the new version of micro direct laser deposition machine of Manudirect company. Assignment of process parameters, placement of CAD designs, slicing the CAD file, control of chamber atmosphere and powder feeding system are accessible through CALD software. The interface of CALD software is shown in Figure 2.6.

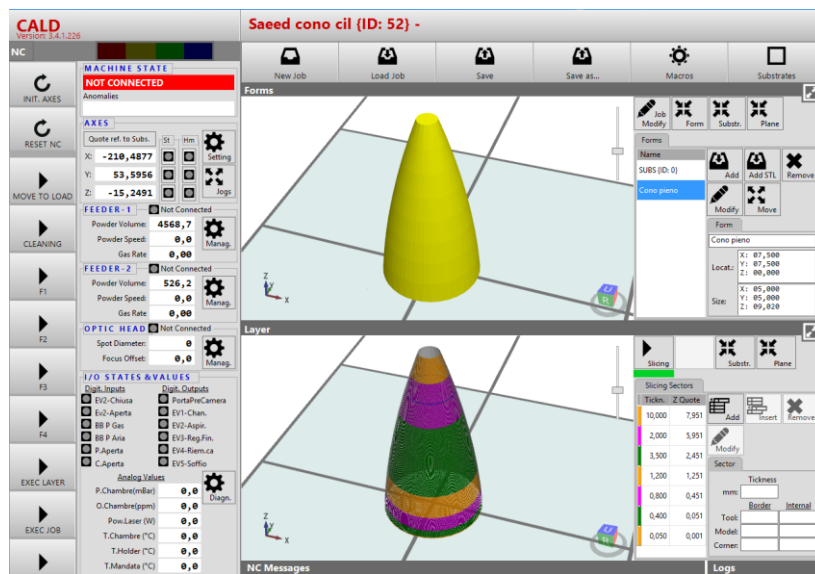


Figure 2.6- Interface of CALD software, Manudirect company

2.1.4 Micro direct metal deposition samples

As shown in Figure 2.7, single tracks with 3mm in length, walls with the same length and different heights, cubes (3mm××3mm××1mm), predesigned porous samples and products containing micro features were prepared by different μ DMD parameters which are concluded in Table 2.3. Experiments were implemented on stainless steel 316 and Ti substrates at room temperature (Figure 2.8). For implementation of single tracks, thin walls and cubes, specific G-codes were written and presented in Appendix B to Appendix E.

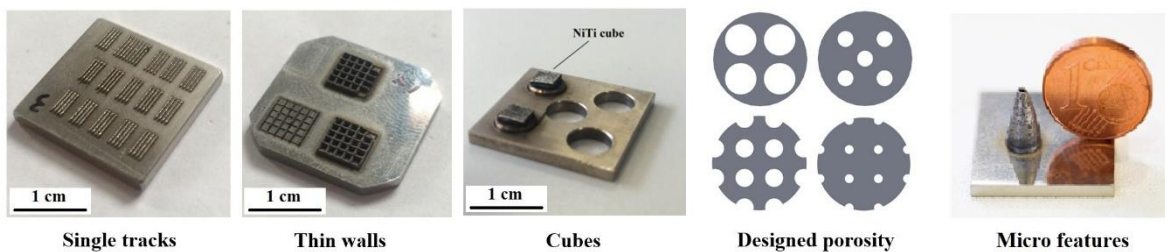


Figure 2.7– Micro direct metal deposition process samples in this project

Table 2.3 – μ DMD process parameters used in this research

P (W)	V (mm/min)	RF _n (mg/min)	T(°C)	E (kJ/mm ²)	t (mm)	O ₂ %
20-40	70- 200	0.76, 1.26	200- 400	0.3-0.85	0.005-0.02	<200 ppm

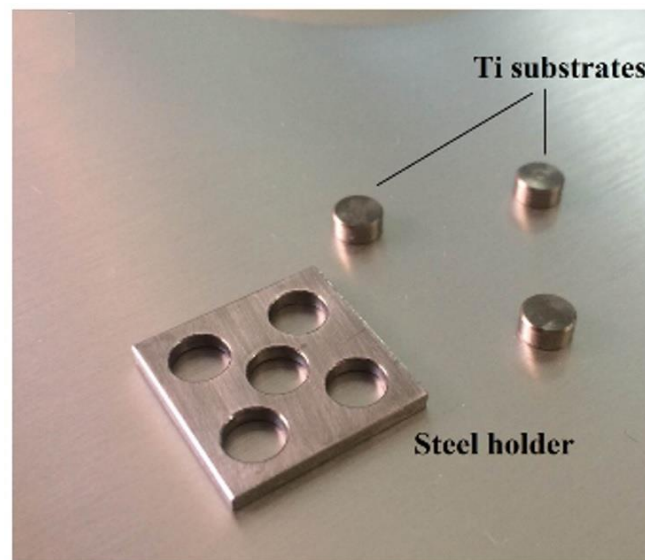


Figure 2.8– Steel 316L substrate holder and Ti pellet substrates

Fabrication of single tracks and thin walls with different process parameters is the easiest way to investigate the effect of process parameters on microstructural characteristics such as micro pore's morphology and distribution in μ DMD parts. To achieve the thickness of each layer (t) produced by a single laser scan, a series of single tracks were processed using different scanning speeds (V), powder feeding rates (RF_n) and substrate temperatures (T) as shown typically in Figure 2.9 (a). The heights of single tracks were measured using a state-of-the-art 3D optical profiler operating in confocal mode by calculating of arithmetic mean values of heights from horizontal sections on each single track (Figure 2.9 (b)).

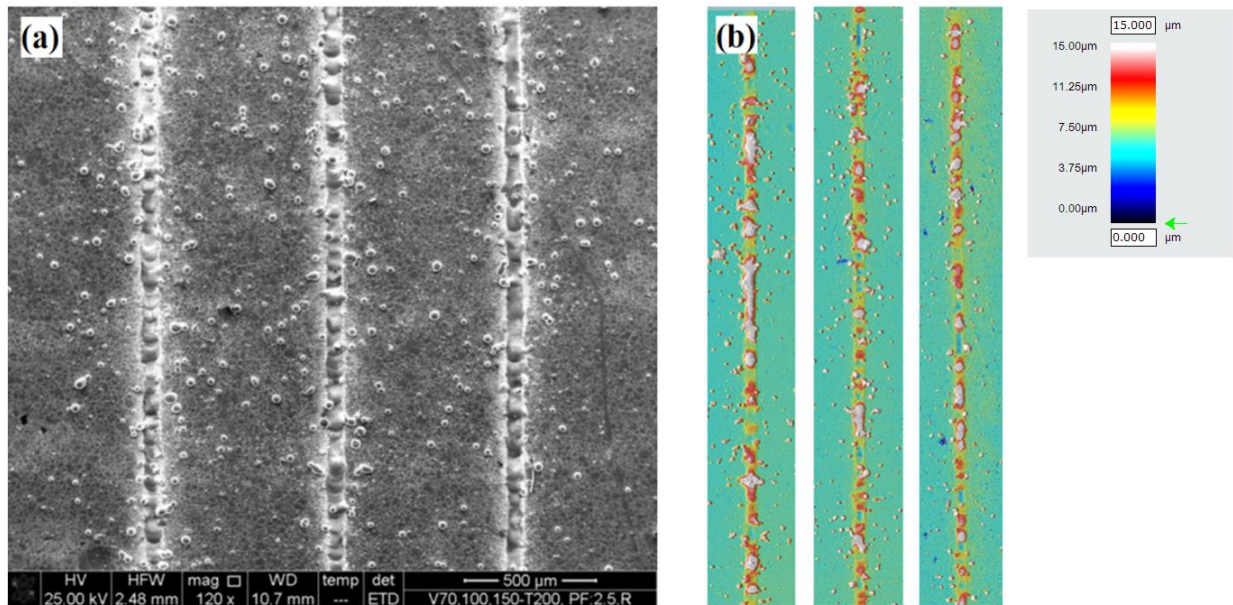


Figure 2.9– SEM image of NiTi single tracks produced by μ DMD (RF_n : 1.26 mg/sec), (b): 3D optical profiles of NiTi single tracks

To produce thin walls, the overlap percentage should be defined for all successive layers. In this project, the layer thickness was considered constant in each wall and was driven from (2.1).

$$\text{Overlap\%} = \frac{\text{Overlap length}}{\text{Layer thickness}} \times 100\% \quad (2.1)$$

Figure 2.10 schematically shows the overlap between the successive layers. The heights of thin walls were measured by 3D optical profilometry, using the same procedure of single tracks.

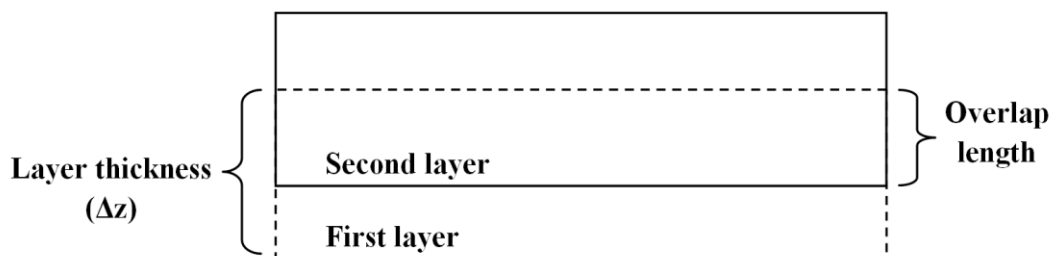


Figure 2.10– Schematic of layer array and overlap between layers.

Controllable micro pores were implemented by varying μ DMD process parameters. To analyse the effect of scanning strategy on controllable micro pore's morphology and distribution, different strategies based on the angles between tracks (θ_T) and layers (θ_L) were examined in this research to produce NiTi cubes. According to Table 2.4, five different strategies were employed to produce 5 NiTi cubes on titanium substrates (Figure 2.8). Shape, sizes and distribution of micro pores in NiTi cubes were analysed using the scanning electron microscope. Porosity measurements were conducted on polished specimens, by performing image analysis of SEM micrographs. Also, the effect of hatch distance (d_H) on micro pore's morphology was investigated using this technique. To investigate the surface quality of micro laser melted NiTi cubes, roughness was measured using 3D optical profilometry. Different scanning strategies produce different cooling regimes and consequently different microstructures are obtainable. The effect of deposition path on the microstructure and texture evolution was also studied keeping the other μ DMD process parameters constant (laser power (P) of 25 W, laser scanning speed (V) of 150 mm/min, distance between the single tracks (d_H) of 100 μ m, substrate temperature (T) of 200 °C and nominal powder feeding rate (RF_n) of 0.76 mg/sec).

Table 2.4– Scanning strategies used to produce NiTi cubes

Strategy	Track's angle (θ_T)	Layer's angle (θ_L)	1 st layer	2 nd layer	3 rd layer	4 th layer
Strategy A	0	0	↓↓↓↓	↓↓↓↓	↓↓↓↓	↓↓↓↓
Strategy B	0	90	↓↓↓↓	←←←←	↓↓↓↓	←←←←
Strategy C	0	180	↓↓↓↓	↑↑↑↑	↓↓↓↓	↑↑↑↑
Strategy D	180	0	↓↑↓↑	↓↑↓↑	↓↑↓↑	↓↑↓↑
Strategy E	180	90	↓↑↓↑	←→←→	↓↑↓↑	←→←→
P=25 W, V=150 mm/min, $d_H=100 \mu\text{m}$, T=200 °C, $RF_n:0.76 \text{ mg/sec}$						

NiTi samples with parallel identical holes and different size below 1 millimeter were produced by μDMD , according to the two different designs illustrated in Figure 2.11. The aim of these designs was to investigate the geometrical accuracy and repeatability of μDMD technology to produce parts with micro features. These types of micro features are of great interest for design and manufacture of bone scaffolds. Making identical holes at different positions was done to examine the repeatability of μDMD process. CAD files were produced using Solidworks commercial computer aided design software and were exported into Power SLICE software installed on the MSL50 machine. The main differences between the two designed parts are the size (i.e. dh = hole diameter) and spatial distribution of holes. In addition, μDMD process parameters related to laser beam movement according to Table 2.5 should be considered.

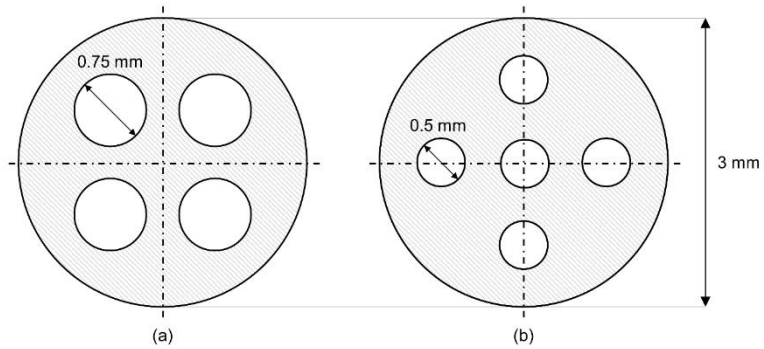


Figure 2.11– Design nr.1 (a) and design nr. 2 (b) of hollow samples with internal holes (top view)

Table 2.5– μ DMD process parameters input

Parameter	Definition
Strategy	Offset/Raster
W_B	Border Width
T_B	Border Layer Thickness
S_B	Border Stepper
O_B	Border Offset
T_I	Internal Layer Thickness
S_I	Internal Stepper
A_R	Raster Angle

According to process parameters listed in Table 2.6, two NiTi samples (A and B) were produced based on design nr. 1 (Figure 2.11) by changing only the laser power (P), while another sample (C) was produced based on design nr. 2 (Figure 2.11) with the same process parameters used for sample B except for the scanning laser speed (V).

Table 2.6 – μ DMD process parameters used for fabrication of NiTi porous samples

Sample	dh (μm)	V (mm/min)	W_B (μm)	T_B (μm)	S_B (μm)	O_B (μm)	T_I (μm)	S_I (μm)	P (W)
A	750	120	250	5	125	125	5	125	20
B	750	120	250	5	125	125	5	125	25
C	500	150	250	5	125	125	5	125	25

2.1.5 Evaluation of μ DMD parts using micro computed tomography

Micro X-ray computed tomography (μ CT) is a three-dimensional (3D) non-destructive imaging technique that allows the investigation of internal and external structures of parts and small features, with micrometric resolution [61]. Metrological CT systems are being used in additive manufacturing research activities to conduct accurate dimensional measurements of both external and internal geometries, evaluation of internal defects (e.g. voids and micro pores) in terms of size, spatial distribution and morphology. For μ DMD samples, μ CT was then used to investigate the dimensional accuracy of the produced parts with respect to the nominal/desired geometry (CAD comparison) and to analyse internal structures and porosity. The samples were scanned using a metrological μ CT system (Nikon X-Tek MCT225, Nikon Metrology/X-Tek Systems Ltd., UK) with 225 kV micro-focus X-ray source, 3 μm focal spot size, flat panel detector with 2000×2000 pixels (16 bit), and temperature-controlled environment (Figure 2.12). The samples were placed on a rotating stage and a number of two-dimensional (2D) X-ray projections were acquired at various angular positions. Such projections were used to reconstruct a 3D model, by means of a filtered back-projection

algorithm. The used CT scanning parameters are listed in Table 2.7. Dimensional evaluations and analysis of internal defects were conducted using software VG Studio MAX (Volume Graphics GmbH, Germany).



Figure 2.12– Nikon MCT 225 micro computed tomography system

Table 2.7– CT scanning parameters for μ DMD parts

Parameter	Value
Voltage	170 kV
Current	36-59 μ A
Exposure time	2000, 4000 ms
Nr. of projections	1500
Filter	0.25 mm, Copper
Voxel size	3.3-6 μ m

Typical images of micro porosity measurements in NiTi thin walls are presented in Figure 2.13. The porosity percentage related to the central part of each wall (shown in red in Figure 2.13) was provided by calculating the total volume of pores against the total selected volume.

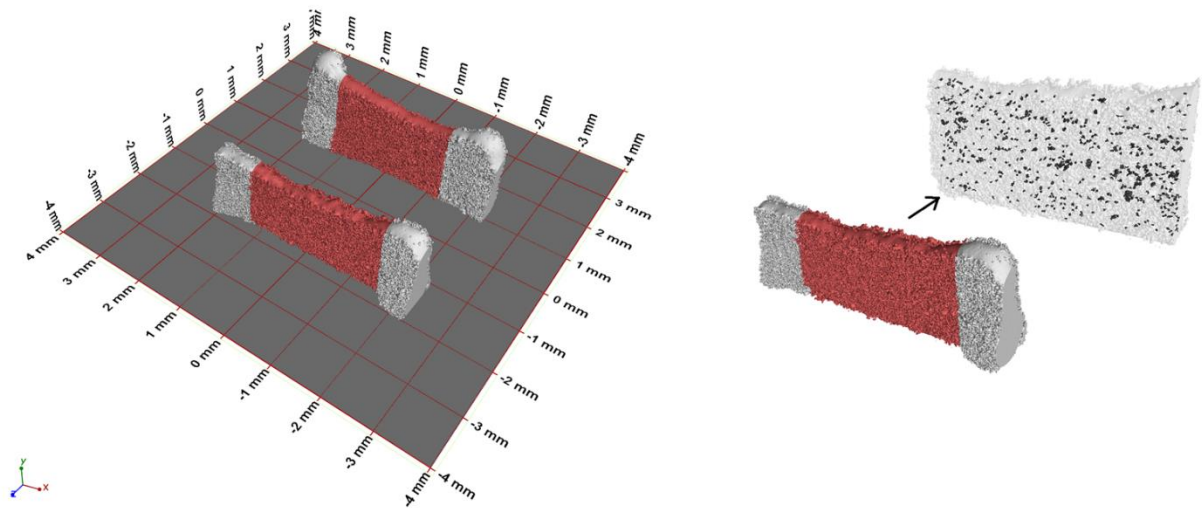


Figure 2.13– μ CT analysis of thin walls produced by μ DMD and inherent micro pore analysis at the central part (red shaded areas)

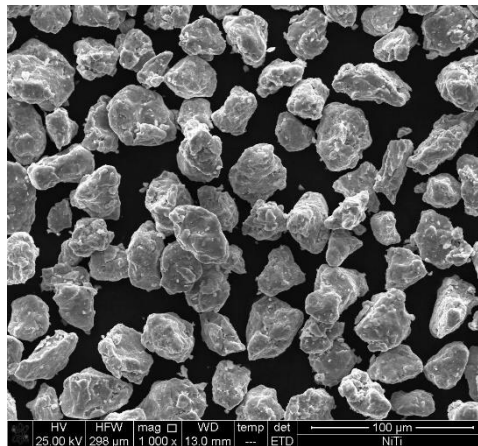
2.2 Experimental procedure of SLM process

2.2.1 Initial powders

Ni_{50.8}Ti_{49.2} (atomic%) pre-alloyed spherical powder produced using electrode induction melting gas atomization (EIGA) technique by TLS Technik GmbH (Bitterfeld Germany) was used in this project as an initial material for SLM. Level of impurities in powder particles is presented in Table 2.8. According to ASTM 2063-05, impurity content levels for medical NiTi are Oxygen < 0.05 wt% and Carbon < 0.05 wt%. Particle size was ranged between 15 μ m and 45 μ m. Figure 2.14 shows the SEM micrograph of initial powder.

Table 2.8- Gas atomized NiTi powder impurity level

Ch. Composition	Carbon (ppm)	Oxygen (ppm)	Nitrogen (ppm)
Ni_{50.8}Ti_{49.2}	50	280	10

Figure 2.14– SEM micrograph of pre-alloyed Ni_{50.8}Ti_{49.2} powder produced by gas atomization, TLS company

2.2.2 Selective laser melting process

NiTi samples were fabricated using MYSINT100 which is a selective laser melting machine of ManuDirect company in Italy (Figure 2.15). Schematic of SLM process in MYSINT100 machine is also presented in Figure 2.16.



Figure 2.15– SISMA MYSINT 100 selective laser melting machine

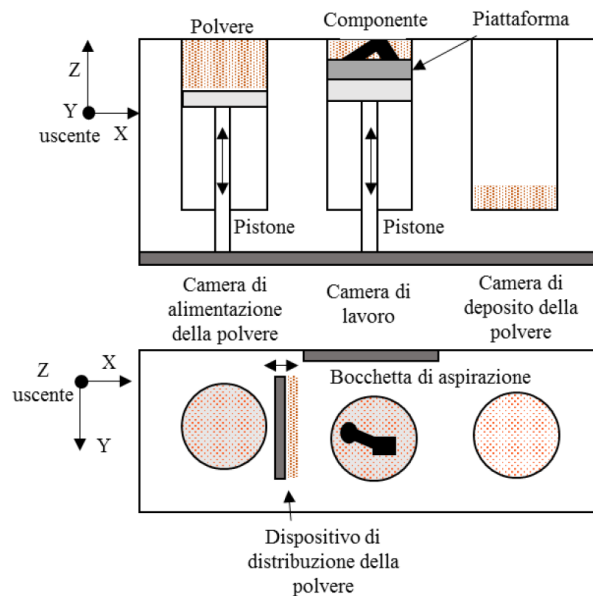


Figure 2.16– Schematic of SLM process in MYSINT100

Firstly, 3D CAD model was imported into the Magics software (Materialise) where the STL file was fixed and edited. In Magics, suitable supports were designed for the 3D models. Then the model and support were sliced into the requisite layers using SISMA build processor software (AutoFab). In Autofab software, process parameters such as laser power (P), scanning speed (V), hatch distance (dh), layer thickness (t) and scanning strategy were defined. MYSINT

100 machine is equipped with a 200 W Ytterbium fiber laser. The beam quality of the laser is $M2 < 1:2$, the beam profile is Gaussian (TEM00), and the beam diameter is $30 \mu\text{m}$. The machine uses a plastic coater roller to create the powder layer. The laser selectively scans and melts the powder according to the CAD model data provided by the machine control software. In SLM machine, the samples are produced on build piston surrounded with unmelted powder and excess powder is recycled using recycle piston. Different scanning strategies such as bidirectional, meander hatch, crossboard meander hatch with connected and crossboard meander hatch with disconnected lines. Figure 2.17 is the schematic representation of SLM roadmap in this research.



Figure 2.17– Roadmap in SLM process

2.2.3 Facilities for preparation and characterization of μDMD and SLM samples

2.2.3.1 Heat treatment

Carbolite CWF furnace was used to implement heat treatment of the samples which is shown in Figure 2.18. The maximum temperature that furnace can reach is 1200°C . The heat treatment temperatures were selected based on the binary NiTi phase diagram. The furnace has been equipped with a sealed atmosphere control chamber.



Figure 2.18– Carbolite CWF furnace

2.2.3.2 Differential scanning calorimetry

A DSC Q200 (Figure 2.19) was used to measure the transformation temperatures in NiTi samples. Temperature range of $-150\text{ }^{\circ}\text{C}$ to $200\text{ }^{\circ}\text{C}$ with the $10\text{ }^{\circ}\text{C}/\text{min}$ heating and cooling rate in a nitrogen atmosphere were utilized. A small quantity of the material (15-35 mg) was used for DSC analysis. The samples were weight measured and encapsulated in an aluminium pan before placing in the DSC analyser. In DSC analysis, the sample is thermally cycled and the difference of the supplied heat power to the reference is measured.



Figure 2.19– Differential scanning calorimetry (DSC Q200)

2.2.3.3 Microstructural Analysis

All μ DMD and SLM samples were cleaned in Acetone ($(\text{CH}_3)_2\text{CO}$) and deionized water solution using ultrasonic cleaner. For polishing, first samples mounted using epoxy resin and hardener. Different grinding papers (400-2500) and diamond suspensions ($9\mu\text{m}$ – $3\mu\text{m}$) were utilized for samples preparation. Finally, alumina suspensions of $1\mu\text{m}$ and $0.5\mu\text{m}$ were used to produce a smooth surface.

Microstructural investigations were performed using a scanning electron microscope (SEM) (Quanta 450, FEI) equipped with an X-ray detector for energy dispersive spectroscopy (EDS), an electron backscattered electron (BSE) detector, and an AMETEK electron backscattered diffraction (EBSD) detector, with TSL OIM data collection software for EBSD acquisition and analysis (Figure 2.20). Image analysis on a series of SEM backscattered images taken from the surface of samples was used to measure the porosity of μ DMD and SLM processed NiTi cubes.



Figure 2.20– Scanning electron microscope (Quanta 450, FEI) equipped with EDS and EBSD

The crystallographic structure of the samples cross-sections was detected by means of x-rays diffraction with a Bragg-Brentano camera (XRD, X'Pert Pro MRD, Panalytical) and the PCPDF database was used for the phase analysis (Figure 2.21). The XRD machine had a $\text{CuK}\alpha$

X-ray source to analyse the phase composition of samples. Scanning was done from 40° to 80° (2θ) at a 0.025° step size.



Figure 2.21– X-ray diffractometer X'Pert Pro MRD, Panalytical

2.2.3.4 Topography assessment using optical micrograph

Optical measurements were performed as they are commonly utilized to evaluate additively manufactured surfaces [62]. In particular, a Sensofar S Neox optical 3D profiler as shown in Figure 2.22 was used in focus variation mode with a $20\times$ objective lens (NA 0.45, field of view $877\times 660\ \mu\text{m}$, spatial sampling equal to $0.65\ \mu\text{m}$ and optical resolution $0.31\ \mu\text{m}$). For each SLM sample, the total measured area is a circle with diameter equal to 5 mm, obtained by stitching a number of single topographies (size $0.5\times 0.5\ \text{mm}$). three surface profiles were then extracted to compute the parameter Pa (on the primary profile, after removing the form error by fitting of the mean line), according to ISO 4288 [63]. Optical profilometer was used to capture 3D images of single tracks, thin walls and bulk NiTi samples produced by μDMD . SensoSCAN neox 3.2.3 software was utilized to measure the dimensions and survey the surface quality of products.



Figure 2.22– Optical profilometer (Sensofar Plu Neox)

2.2.3.5 Hardness measurement

Five Vickers micro-indentations were performed to evaluate the hardness of the samples' cross-sections with a load of 100-200 g for 15-20 s. Samples were mounted and mirror polished prior to the test.

2.2.3.6 Compression tests

Compression tests were conducted by the 100 kN MTS Landmark servo-hydraulic test platform. A strain rate of 10^{-4} sec^{-1} was employed during loading while unloading was performed under force control at a rate of 100 N/sec. The strain was measured by an MTS high-temperature extensometer which was attached to the grips.

Chapter 3 Results and discussion: μ DMD

The aim of this research is the evaluation of recently developed laser aided additive manufacturing method named micro direct metal deposition (μ DMD) [64] for fabrication of components with micro features. Improvement of geometrical accuracy and repeatability of micro features implementation in additive manufactured parts were defined as the main goals. Considering the perspective of biocompatible porous scaffolds design and manufacture for hard tissue replacement, decrease in minimum achievable hole size makes possible to design and manufacture controlled porous scaffolds mimicking the internal architecture of real bone. Such porous structures enhance bone ingrowth [65]. In this research, μ DMD process was used to produce NiTi parts with predetermined cylindrical holes via tuning of process parameters such as hatch distances and laser spot diameter. To characterize the produced parts, scanning electron microscopy and micro X-ray computed tomography (μ CT) were used in this work. On one hand, SEM allowed analysing their external surface, including the presence of partially melted powder particles. On the other hand, μ CT allowed geometrical measurements on both external and internal features. In particular, μ CT was selected because of its capability of obtaining a holistic 3D reconstruction of the scanned workpiece [66], as well as of measuring size, morphology and distribution of internal porosity in a non-destructive way [67].

3.1 APP (Aiming to Process Parameters) procedure

Preliminary investigation of μ DMD process parameters via production of NiTi single tracks and thin walls was done through APP process. The effects of powder and laser defocusing distances and also process parameters on the surface quality of single tracks and thin walls are presented in this section. A modified model is described to estimate the height of thin walls. The main objective of the results presented in this section is to find the preliminary parameters of μ DMD process and assess whether this process is a suitable method to produce complex structures with micro scale features from NiTi. To achieve this objective, single tracks and

small thin walls were selected to implement. Single tracks were used to find the best positions of working plane and laser focal plane during the process and also to find basic process parameters such as power of laser and scanning speed. Small thin walls were implemented to survey the capability of μ DMD process in production of small 3D parts.

3.1.1 μ DMD process parameters

Total input energy produced by moving laser beam can be calculated using equation [68]:

$$E_L = \frac{P}{dl \times V} \quad (3.1)$$

Where P is the laser power, dl is the diameter of laser focus point and V is the scanning speed. When the total input energy by the laser is too low, in the other word, when the power of laser is low or the scanning speed is too high, the produced energy is not enough to form a proper melt pool. By increasing the power of laser or reducing the scanning speed, powder particles absorb more energy and the track forms. But, when the total energy produced by the laser goes too high (when the power of laser is too high or the scanning speed is too low), vaporized metal atoms form low temperature plasma. This plasma has an impact force on melt pool. In μ DMD process, because of small diameter of laser beam (30 μm in this research); the input energy produced by moving laser is too high according to equation (3.1). Therefore, during the μ DMD process the impact force would throw the molten or partially melted particles out of the melt pool and disturb the track formation even in low laser powers (see Figure 3.1). This phenomenon is called *baling effect* which is shown in Fig using red arrows.

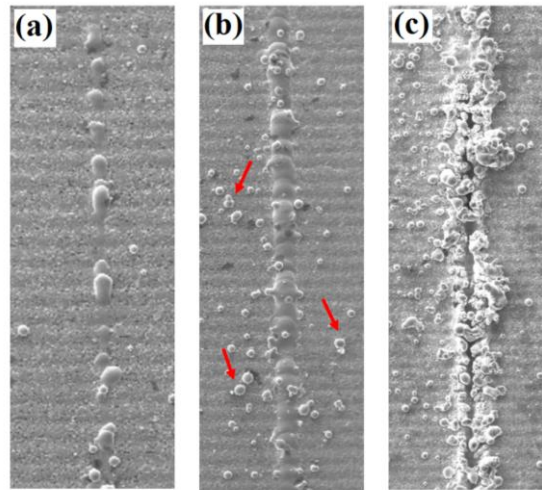


Figure 3.1– NiTi single tracks, (a) $P= 20 \text{ W}$, $V= 20 \text{ mm/min}$, $d_l= 30 \mu\text{m}$, $E= 2 \text{ KJ/mm}^2$, (b) $P= 30 \text{ W}$, $V= 20 \text{ mm/min}$, $d= 30 \mu\text{m}$, $E= 3 \text{ KJ/mm}^2$, red arrows show baling effect (c) $P= 50 \text{ W}$, $V=20 \text{ mm/min}$, $d= 30 \mu\text{m}$, $E= 5 \text{ KJ/mm}^2$

Low laser powers reduce the heat affected zone (HAZ) and improve the quality of final products. Surface analysis of single tracks produced by μ DMD using SEM revealed that, increase in power of laser causes to slightly increase in the area of HAZ region (

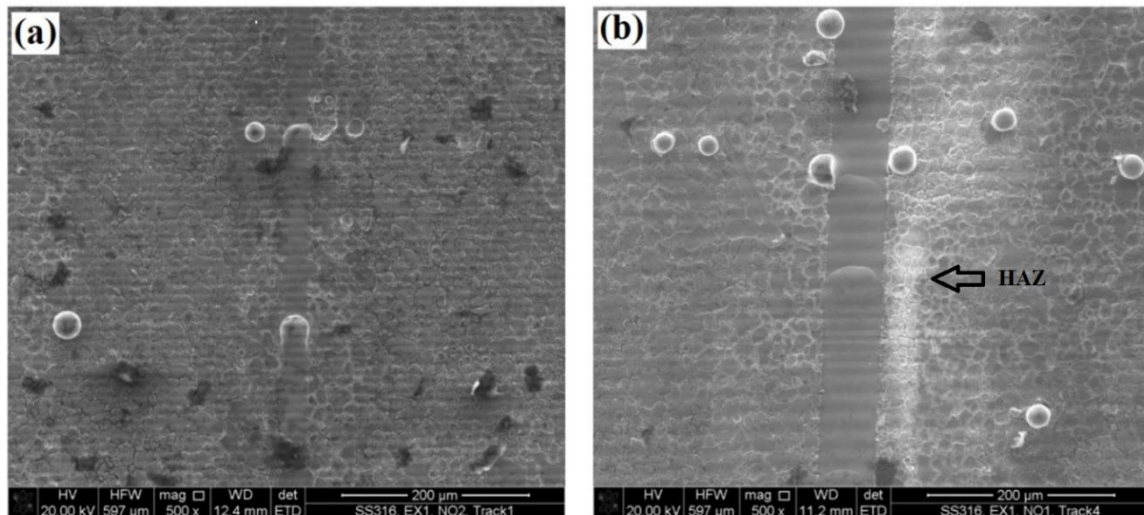


Figure 3.2). It can be attributed to the small laser spot diameter in μ DMD process.

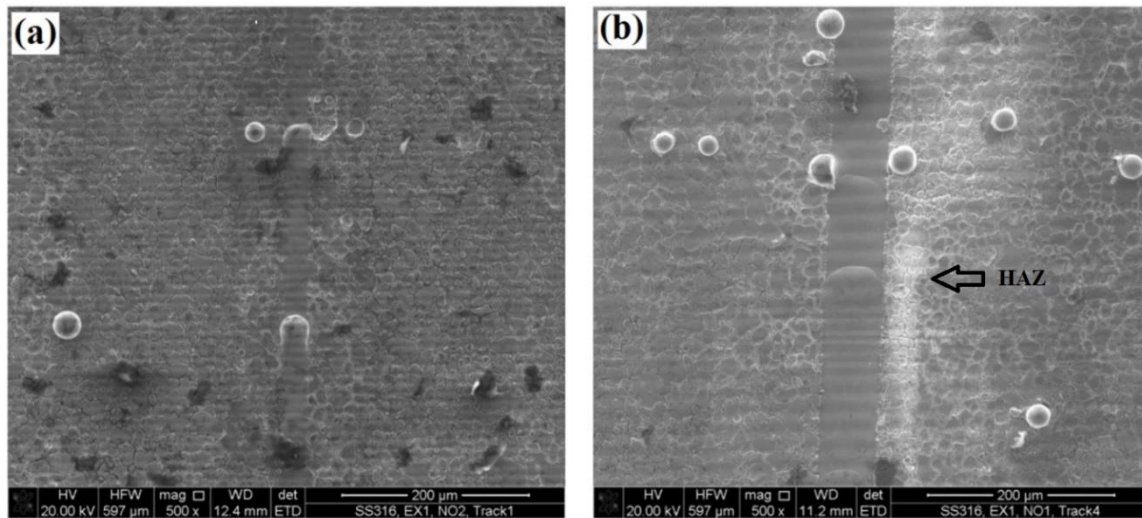


Figure 3.2– Scanning electron micrographs of single tracks using (a) P= 15 W, (b) P= 40 W of laser power

3.1.1.1 Laser and powder defocusing distances

The governing equations for the Argon carrier gas are described in a Eulerian reference frame (Appendix A). The position of powder focus point was calculated as a function of powder feeding parameters [69]. As can be seen in Figure 3.3, the powders which are injected by the 11 injectors form a dense powder column. The distance between the nozzle and the centre of this powder column has been measured using image analysis method. S2 is an assumptive plane which has 2.57 mm distance from the nozzle (zero point); this plane was used to simplify the calculations and also programming in MSL50 machine. Experiments showed that, the position of dense powder column would be constant as long as the flow of carrier gas is constant.

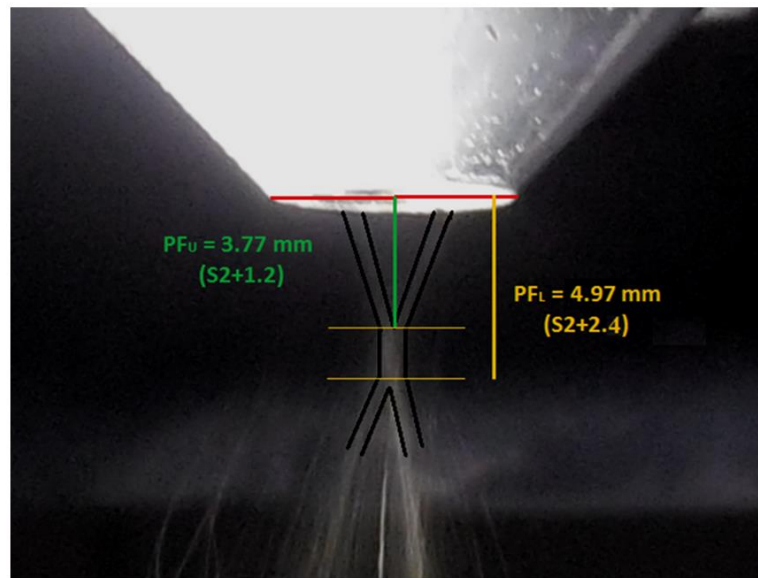


Figure 3.3– Coaxial powder feeding system in micro laser melting machine, RFn= 0.76 mg/sec, carrier Argon flow= 0.7 lit/min, (S2= 2.57 mm)

Figure 3.4 (a) schematically presents the geometry of dense powder column. As can be seen in this image, the bottom of the nozzle was defined as zero point; d_{LF} is the laser defocusing distance, d_{PF} is the powder defocusing distances and d_{WP} is the distance between the working plane and zero point (bottom of the nozzle). The dimensions of dense powder column at 0.7 lit/min of carrier gas flow rate and 3 different regions of dense powder column are also presented in Figure 3.4 (b). According to the Figure 3.4 (a):

- If $(d_{WP}-d_{LF}) < 0$, Laser is in negative defocusing and the laser is focused below the working plane.
- If $(d_{WP}-d_{LF}) > 0$, Laser is in positive defocusing and the laser is focused above the working plane.
- If $(d_{WP}-d_{PF}) < 0$, Powder is in negative defocusing and the centre of dense powder column is focused below the working plane.
- If $(d_{WP}-d_{PF}) > 0$, Powder is in positive defocusing and the centre of dense powder column is focused above the working plane.

When the laser is focused on working plane ($d_{LF}=d_{WP}$), laser defocusing is zero; Also, when the working plane is at the centre of the dense powder column, the powder defocusing is zero.

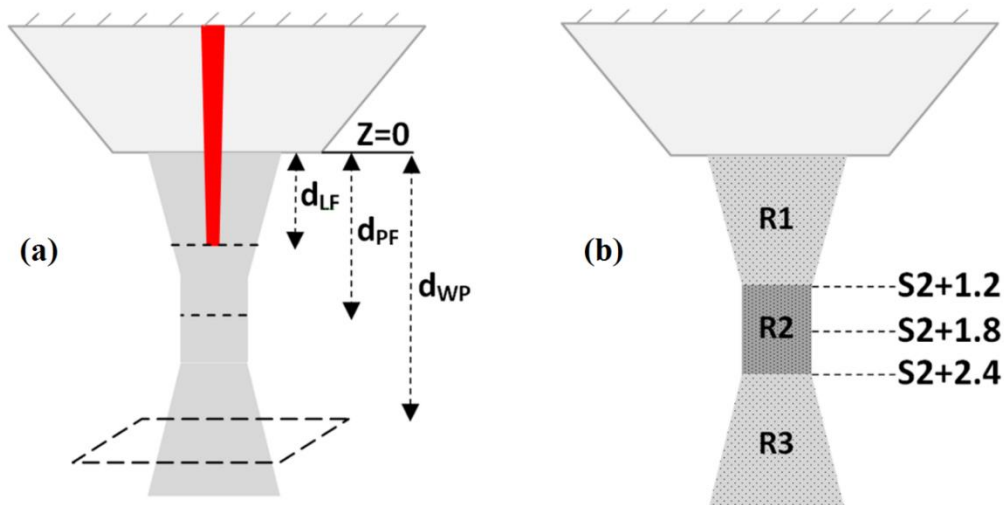


Figure 3.4– (a) Positions of laser focus point (d_{LF}), middle of dense powder column (d_{PF}) and working plane (d_{WP}), (b) different regions of dense powder column (Ar flow: 0.7 lit/sec), ($S_2 = 2.57$ mm), (all dimensions in mm)

To analyse the effects of laser and powder defocusing distances on continuity and quality of micro laser melted parts, single tracks were implemented by varying the laser and powder defocusing distances at constant process parameters (P : 30 W, V : 50 mm/min, RF_n : 0.76 mg/sec). All experiments were implemented in two repetitions to cover whole region 2 in Figure 3.4 (a). In all sets of laser and powder defocusing distances, the distance between the laser focus point and the working plane was kept below 0.6 mm. Figure 3.5 shows an APP procedure roadmap find the best positions for laser and powder defocusing distances. Scanning electron microscope was used to determine the quality of single tracks and depends on this approach; the tracks were divided to 3 categories: high (continuous melting), medium (partial melting) and low quality (no melting).

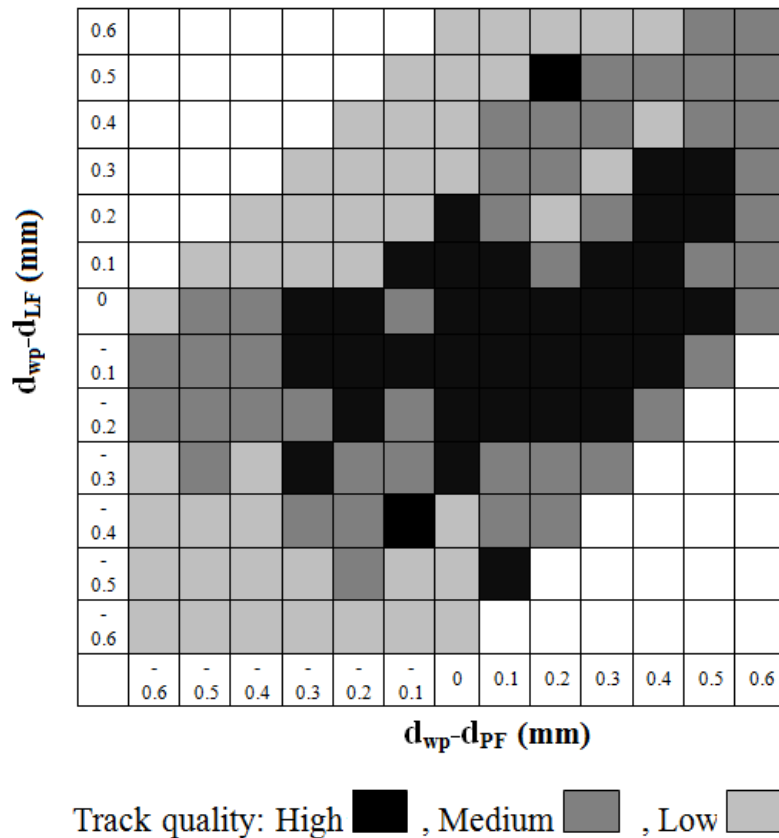


Figure 3.5– Road map for finding the best positions of working plane and laser focus in μ DMD process

Figure 3.5 illustrates that when the working plane was placed in lower half of region 2 ($d_{WP}-d_{PF} \geq 0$ and $S2+1.8 \leq d_{WP} \leq S2+2.4$) and laser was in positive defocusing ($d_{WP}-d_{LF} \geq 0$), higher number of high quality NiTi single tracks were produced. Figure 3.6 shows the effect of working plane's position on the quality of single tracks when the laser focus was placed in the upper half of the R2. Track A in Figure 3.6 (a) was implemented while the laser focus point and the working plane were placed at the same position of $S2+1.5$ mm which is the upper half center in R2 region. In this plane, the quantity of powder flow was not at maximum value; However, because of the same positions for the laser focus point and the working plane, high portion of laser energy was transferred to the existing powder particles and a continuous track was implemented. In tracks B to D, the position of the laser focus point was constant at $S2+1.5$ mm and the working plane went down gradually of 0.1 mm steps. As can be seen, increasing distance between the laser focus point and the new positions of working planes degraded the

quality of single tracks. It is because of lower energy absorbed by constant powder flow. When the working plane reached to S2+1.9 mm and S2+2 mm, the quality of tracks increased again while the positions of laser focus point was constant S2+1.5 mm. It means that, with lower energy absorption, more melting occurs when the working plane is placed at the position that the maximum powder flow exists. Therefore, it seems that, the maximum powder flow rate exists in lower half of R2 (S2+1.8 mm to S2+2.4 mm) and below the center of dense powder column (S2+2 mm). To prove this theory, the laser focus point was placed on S2+2 mm and the working plane went down gradually of 0.1 mm steps. As can be seen in Figure 3.6 (b), near all tracks are continuous and with increasing the distance of laser focus point and working plane, the regularity of single tracks degrades.

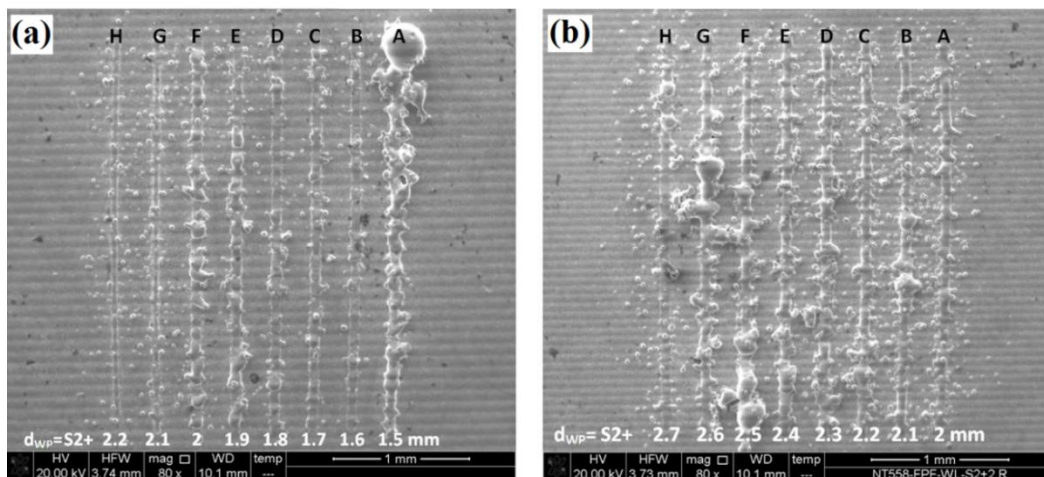


Figure 3.6– (a) NiTi single tracks produced by different working plane positions, same laser focus point (S2+1.5mm) and same process parameters (P= 30 W, dl= 30 μ m, V= 50 mm/min, RFn= 1.26 mg/sec), (b) NiTi single tracks produced by different working plane positions, same laser focus point (S2+2 mm) and same process parameters (P= 30 W, dl= 30 μ m, V= 50 mm/min, RFn= 1.26 mg/sec)

It was concluded that the best position for working plane was the center of lower half of dense powder column (S2+2.2 mm). In this position, the powder is in 0.4 mm positive defocusing. In fact, this plane has maximum powder flow rate. Selection of suitable laser defocusing can ensure surface quality of products. For this purpose, 3 different thin walls with same powder defocusing (+0.4 mm), same process parameters and different laser defocusing were implemented. From

Figure 3.8 it can be understood that when the laser was placed at positive defocusing of 0.2 mm, a regular thin wall with minimum surface roughness was implemented. In DMD process, a slight unevenness usually exists on the top layer of thin-walled metal parts in building height due to the fluctuation of process parameters (laser power and powder mass flow rate) [17]. When the laser is placed slightly upper than working plane, the area of dense powder column which has incident with laser beam increases. Therefore, powder quantity raises and consequently more melting occurs. Also, when the laser is focused above the working plane, unevenness of surface can be solved by self-regulation or automatic compensating phenomenon. In the other world, melting rate decreases at convex positions and increases at concave positions. It can be attributed to small area of laser spot at convex positions and large area of laser spot at concave positions. Surface roughness measurements of walls using optical profilometry are summarized in Table 3.1 for walls (a)-(c) according to Figure 3.7. It can be seen that the minimum surface unevenness is for the wall which has positive defocusing for both laser and powder.

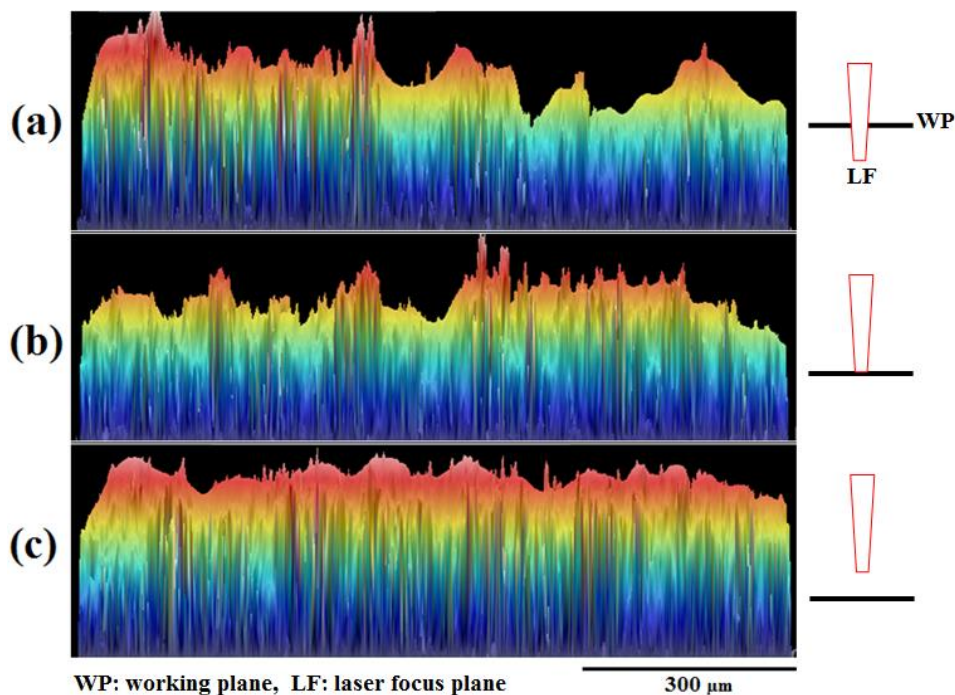


Figure 3.7– Optical profiles of thin walls produced by μ DMD, working plane: S2+2.2 mm, laser focus plane (a): S2+2.4, (b): S2+2.2 and (c): S2+2 mm.

Table 3.1– Surface roughness of thin walls

	Laser defocusing distance (mm)	Number of layers	Ra (μm)
Wall (a)	S2+2.4	30	28.9
Wall (b)	S2+2.2	30	22.8
Wall (c)	S2+2	30	16.8

3.1.2 New approach to calculate the height of single tracks and thin walls

The height of a single track (H) produced by laser melting can be calculated by equation [70]:

$$H = \frac{\eta \cdot RF_n}{dl \cdot \rho_p \cdot V} \quad (3.2)$$

where η is the melting efficiency of powder, RF_n is the nominal powder feeding rate, dl is the diameters of laser spot, ρ_p is the powder true density and V is the speed of scanning. In DMD process, this equation will be valid until the ratio of laser spot diameter to the diameter of the dense powder column is near to 1. In μ DMD, this ratio has very low values. Therefore, the effective feeding rate should be defined as:

$$RF_e = RF_n \cdot \left(\frac{dl}{D}\right)^2 \quad (3.3)$$

where RF_e is the effective feeding rate applied on melt pool, and D is the diameter of dense powder column. The height of thin walls produced by μ DMD can be calculated by a modified model:

$$H_{\mu DMD} = \frac{n \cdot \eta \cdot RF_n}{d \cdot \rho_p \cdot V} \left(\frac{dl}{D}\right)^2 \quad (3.4)$$

Where $H_{\mu DMD}$ is the height of single track and n is the number of single tracks in a thin wall. Unlike the classical DMD processes, in μ DMD, the height of thin walls raises with increasing in laser spot diameter when the laser spot diameter is very small in comparison to dense powder

column. To examine this modified model, 4 different thin walls according to Table 3.2 were produced.

Table 3.2– Overview of process parameters used for NiTi thin walls production ($\Delta Z=t$: layer thickness, NH: nominal height of thin wall)

	P (watts)	V (mm/min)	RFn (mg/sec)	ΔZ (μm)	NH (mm)
Wall (1)	30	20	1.26	10	0.1
Wall (2)	30	50	1.26	10	0.1
Wall (3)	30	70	1.26	10	0.1
Wall (4)	30	100	1.26	10	0.1

Figure 3.8 shows the scanning electron micrographs of the walls (1), (2) and (3) presented in Table 3.2.

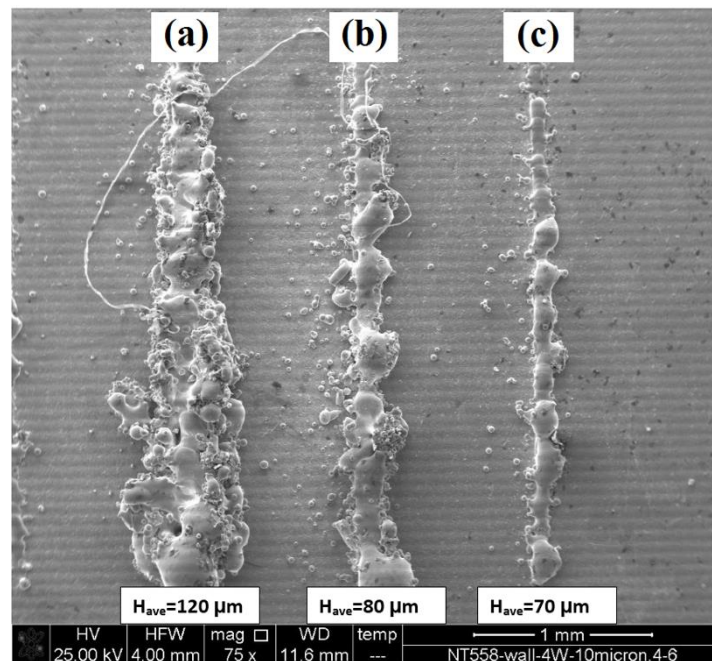


Figure 3.8– NiTi thin walls produced by μ DMD and $P= 30$ W, $\Delta Z= 10$ μm , $\text{RFn}= 1.26$ mg/sec, $\text{NH}= 100$ μm , $V=$ (a, Wall 1): 20, (b, Wall 2): 50, (c, Wall 3): 70 mm/min

The heights of these walls were measured using focus variation method. Figure 3.9 (a) shows the top view of the walls and Figure 3.9 (b) illustrates a typical NiTi thin wall 3D image taken by optical profilometer.

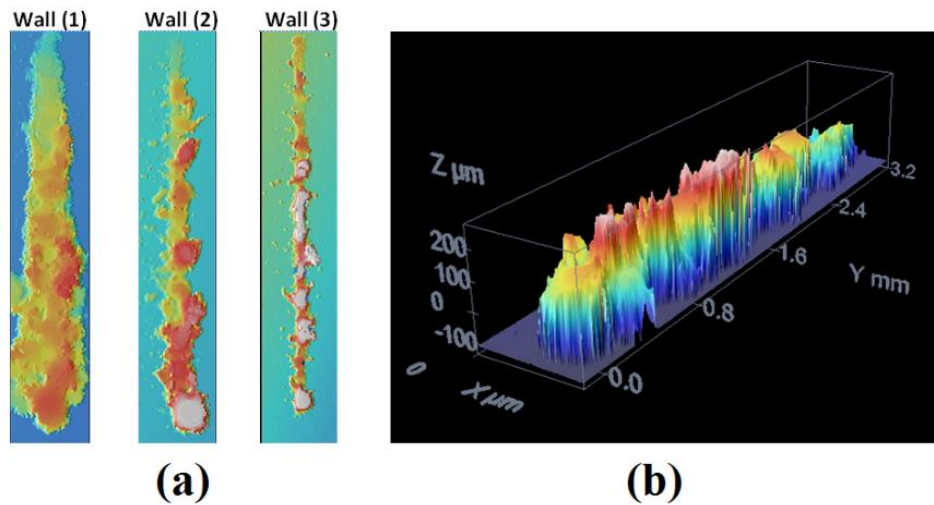


Figure 3.9– (a) 2D optical profiles of NiTi thin walls (1) to (3) according to Table 3.2, (b) 3D image rendering of wall (2).

As can be seen in Figure 3.8, increasing in scanning speed, improved the quality of wall surface. Thin wall implemented using 70 mm/min of scanning speed was almost uniform and smooth (Figure 3.8 (c)). Raise in scanning speed from 20 to 100 mm/min, decreased the height of thin walls from 120 μm to 47 μm . The nominal height (NH) of all walls is 100 μm .

As can be seen in Figure 3.8 (a), at lower scanning speeds, there were more partially melted particles around the wall as a result of baling effect. It is because of the long-time laser exposure. Figure 3.10 (a) illustrates a good agreement between the calculated heights by modified model and the experimental measurements carried out using focus variation method and optical profilometer. Thin wall height estimation using classical approach is not presented in this graph since the calculated values were out of range (20-100 mm).

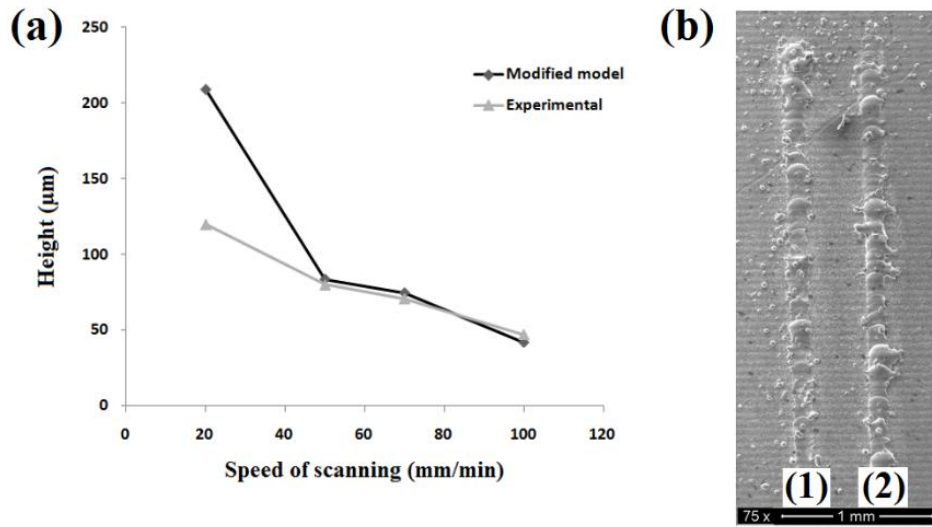


Figure 3.10– (a) the effect of scanning speed on the height of NiTi thin walls produced by μ DMD ($\eta=0.5$), (b) NiTi single tracks, $P= 50$ W, $RFn= 1.26$ mg/sec, $V= (1): 20$ mm/min, (2): 40 mm/min.

Figure 3.10 (a) depicts that, in low speeds of scanning, the estimated height by modified model has a significant variation as compared to the experimental value. In fact, when the laser scanning speed is too low, such as 20 mm/min in this experiment, the melt pool absorbs more energy per unit time. However, this phenomenon does not increase the melting efficiency. In the other word, it is true that decreasing in scanning speed raises the quantity of melted powder and consequently the height single tracks. However, it does not mean that the efficiency of melting process has increased. Reduction in speed of scanning accelerates the evaporation reaction and the gas pressure produced around the melt pool inhibits the powder particles to enter the melt pool. Moreover, formation of gas bubbles inside the melt pool because of high temperature at low velocity, throw the droplets out of the track.

M_a is Reynolds number which is a parameter to describe the ratio of surface tension gradient force to viscous force and can be calculated by equation (3.5) [71]:

$$M_a = \rho L_R \Delta T \left| \frac{\partial \gamma}{\partial T} \right| / \mu^2 \quad (3.5)$$

Where ρ is the density of melt pool, L_R is the radius of melt pool, ΔT is the temperature difference, μ is the viscosity of molten metal and γ is the surface tension of liquid metal. It should be mentioned that, according to equation (3.5), surface tension changes with temperature. At low scanning speeds, there is a sharp temperature gradient (high ΔT) and consequently a sharp surface tension gradient from the centre of the melt pool to the edges. This surface tension gradient induces a force that makes Marangoni effect in melt pool. As stated before, low scanning speeds lead to high ΔT , high surface tension gradients and also intensive Marangoni effect. Therefore, low scanning speeds accelerate swirling flow and cause to splash more molten particles out of the melt pool on the surface. As can be seen in Figure 3.10 (b), with low scanning speed of 20 mm/min, more powder particles were around the single track (1) than the single track (2) produced by 50 mm/min scanning speed. It can be concluded that, decreasing the scanning speed degrades the melting efficiency (η) and causes more deviations of modified model to experimental values since in the model the melting efficiency (η) was kept constant.

3.2 Single phase NiTi by μ DMD of elemental powder mixtures

As stated before, unwanted secondary phases are unavoidable in DMD of NiTi from (Ni+Ti) elemental powder. In this section, the combination of high energy mechanical alloying and micro direct metal deposition techniques is experimented with the aim of assessing the feasibility of synthesizing single phase NiTi from elemental Nickel and Titanium powders. Therefore, different powder batch and cubic samples have been produced according to Table 3.3 and Table 3.4.

Table 3.3– NiTi powder batches produced by mechanical alloying of elemental powders.

Powder	Ni (at %)	Ti (at %)	Milling time (h)	Heat treatment
A	50	50	4	-
B	50	50	8	-
C	50	50	10	-
D	50.8	49.2	10	-
E	50.8	49.2	10	1050°C, 8 h

Table 3.4– NiTi cubes produced by μ DMD and alloy powders presented in Table 3.4.

Cube	Powder	Power (W)	Scan speed (mm/min)	Powder rate (mg/sec)	Layer thickness (μ m)
1	B	30	50	1.24	10
2	D	30	150	1.24	10
3	E	30	150	1.24	10

3.2.1 High energy mechanical alloying of (Ni-Ti) mixtures

The effects of milling time and initial Ni-Ti atomic ratio on phase composition and morphology of Ni-Ti powder mixtures were investigated before and after μ DMD process. Figure 3.11 depicts the XRD patterns of equiatomic Ni₅₀Ti₅₀ after different time of milling. It can be observed that, after 8h of milling time, Ti peaks disappeared and a Ni supersaturated solid solution and NiTi (B2) are formed. After 10 h of milling, the Ni diffraction peak is partially substituted with the NiTi (B2) phase which is the predominant phase. However, it should be considered that phases with fraction <2-3% can hardly be detected with XRD, especially when the ration between maximum peak intensity and background is poor.

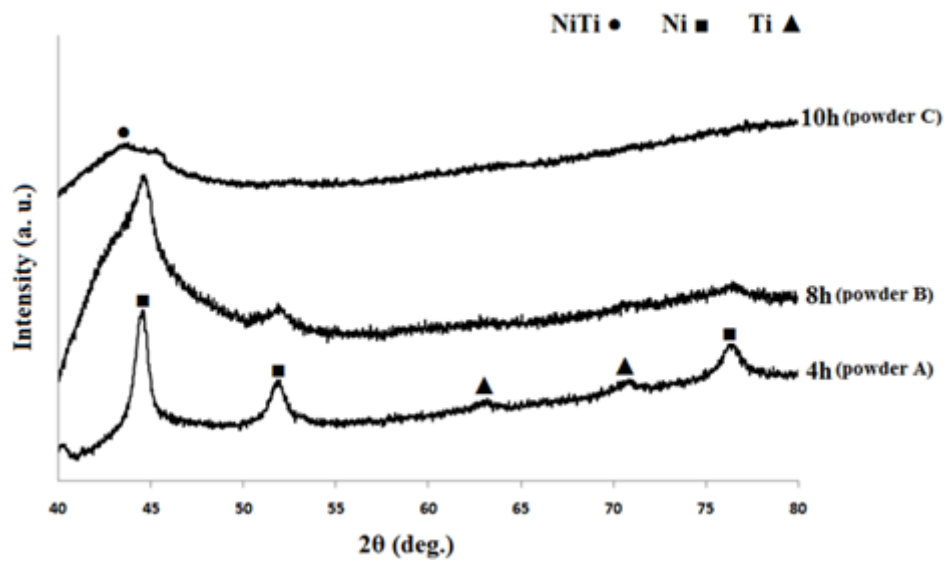


Figure 3.11– X-ray diffraction patterns of Ni₅₀Ti₅₀ alloy powder after different time of milling (powders A, B and C).

Figure 3.12 show the morphology of milled powders at two different milling times. With increasing milling time, fragmentation of alloyed powder particles resulted in fine particles. As shown in Figure 3.13 (a), two different colors in grey scale after 4h milling of Ni₅₀Ti₅₀ alloy and a lamellar composite structure of the Ni and Ti were observed. By increasing the time of milling from 4h to 8h, the lamellar structure has been changed to a single color and bright region in grey scale. Therefore, it seems that after 8h of milling (Figure 3.13 (b)), a single phase Ni-Ti has been developed.

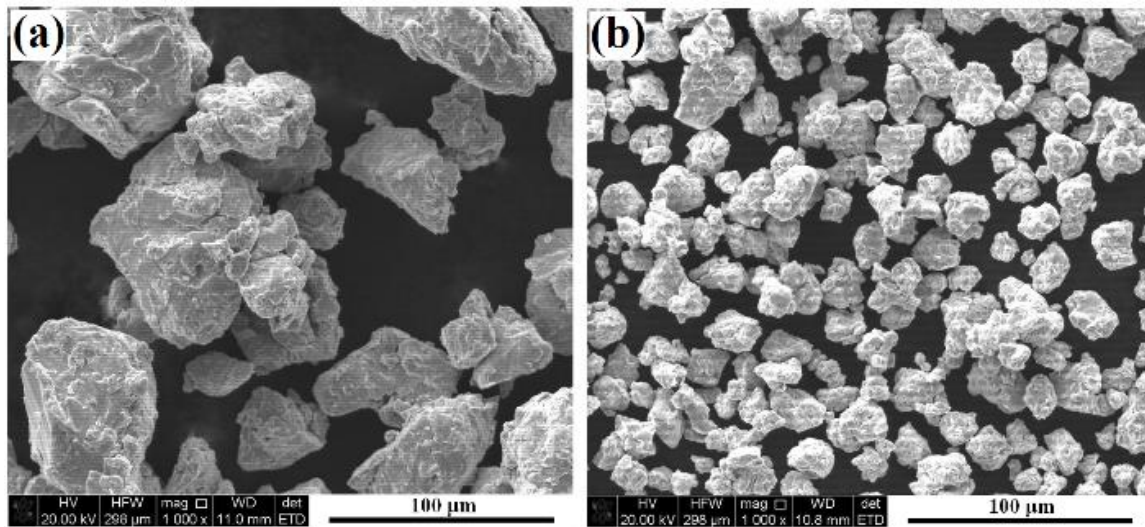


Figure 3.12– Morphology of Ni₅₀Ti₅₀ alloy powder particles after (a) 4h (powder A) and (b) 8h (powder B) of milling time

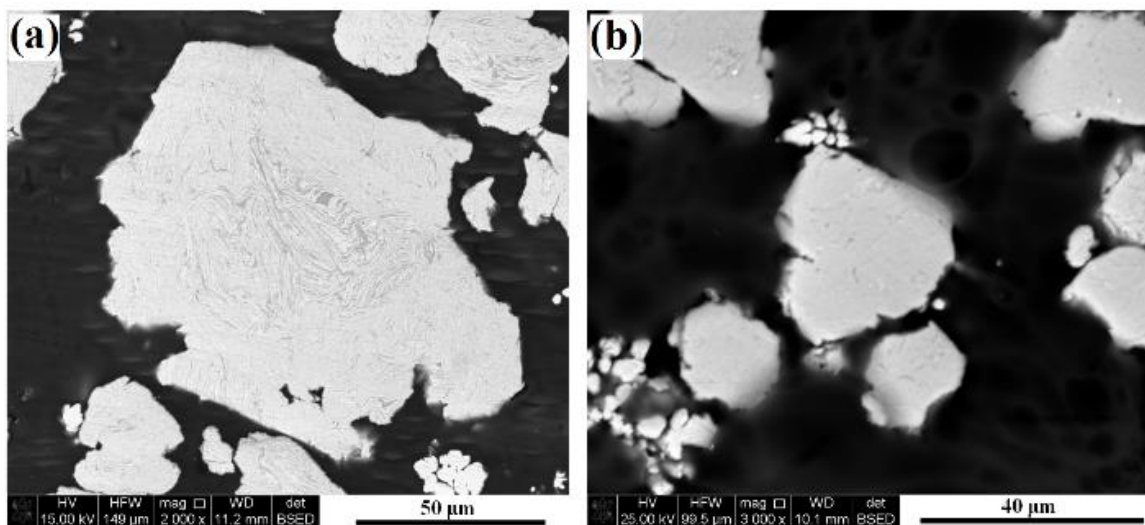


Figure 3.13– Backscattered electron micrographs of Ni₅₀Ti₅₀ powder particles after (a) 4h of milling (powder A) and (b) 8h of milling (powder B)

Ni-Ti is a ductile-ductile binary system where, in the early stages of milling, the ductile components are flattened by a micro-forging process [41]. In the next stage, these flattened particles are cold welded together and form a composite with lamellar structure of the constituent metals. This phenomenon can be seen in Figure 3.13 (a) where the darker shaded area is Ti. It means that the structure is not homogenous after 4h milling. By increasing the

milling time to 8h, the cross section of powder particles shows near one gradation in the grey scale (Figure 3.13 (b)). As presented in Figure 3.11, X-ray diffraction pattern showed that after 8h of milling, near single phase structure has been formed. As can be seen in Figure 3.11, increasing in milling time from 4h to 8h causes to broadening and significant decrease in peak intensity of Ni and elimination of Ti peaks. After 8h of milling, Ni peaks moved towards lower angles. This phenomenon can be attributed to the formation of Ni (Ti) solid solution. In fact, diffusion of larger atoms of Ti into the Ni lattice increases the lattice parameter of Ni and shifts the Ni peaks to the lower angles.

Figure 3.14 shows the line scan elemental analysis at cross section of powder particles. Microstructure becomes more homogenous when milling time increases from 4 to 8 h.

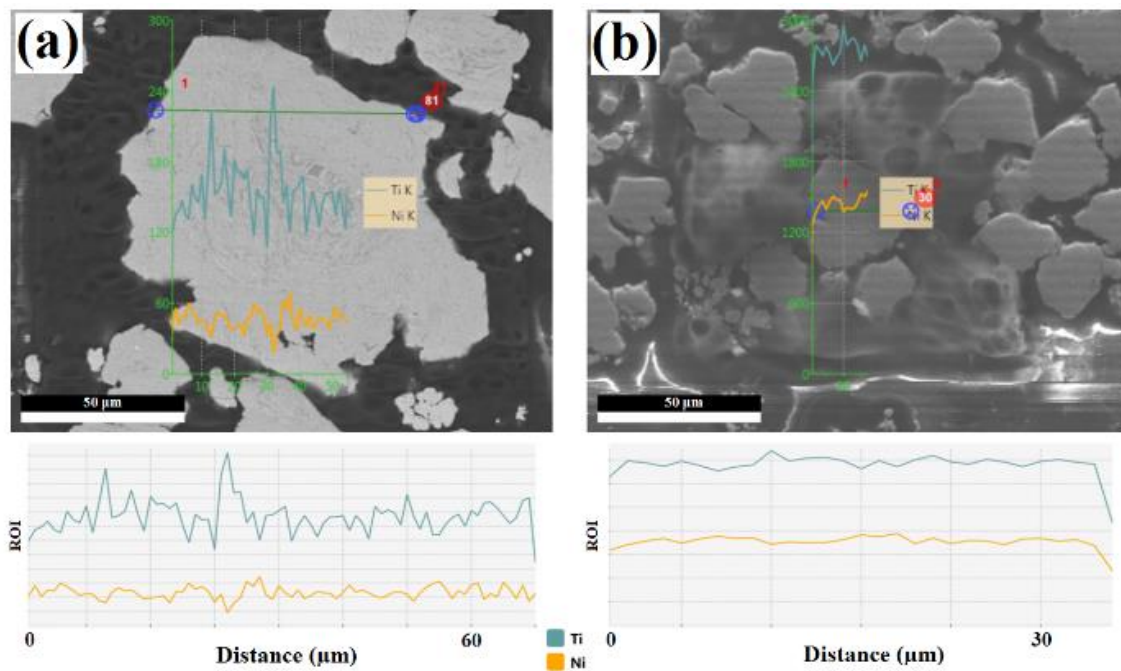


Figure 3.14– EDS analysis in line scan mode of Ni₅₀Ti₅₀ powder particles after (a) 4h of milling (powder A) and (b) 8h of milling (powder B)

3.2.2 Micro direct metals deposition of mechanically alloyed NiTi alloy

Figure 3.15 shows the X-ray graph of cube 1 (Table 3.4) which is the product of μ DMD on Ni₅₀Ti₅₀ powder. The phase constituents are NiTi (B2), NiTi₂ and NiTi (B19'). Figure 3.16 depicts that, after laser deposition of powder B (Table 3.3), Ti rich NiTi appeared. By increasing the milling time, homogeneity of Ni-Ti composite increases and it may facilitate development of single phase NiTi after laser melting.

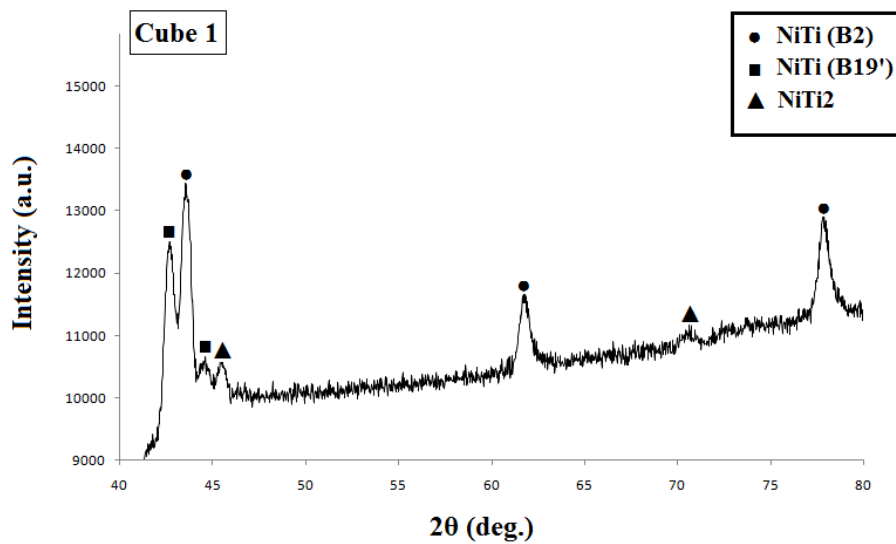


Figure 3.15– X-ray diffraction pattern of laser melted Ni₅₀Ti₅₀ (cube 1, Table 3.4)

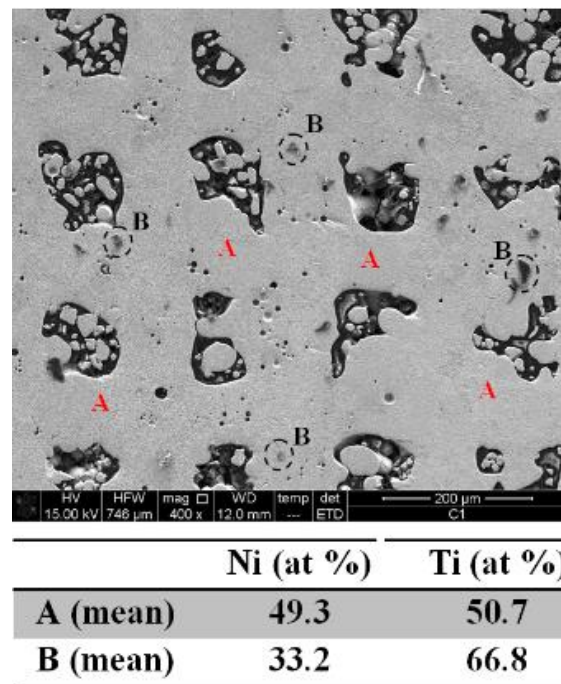


Figure 3.16– Chemical composition of phase constituents in laser melted Ni₅₀Ti₅₀ powder (Cube 1, Table 3.4)

Total input energy produced by μ DMD can be calculated using Equation (3.1). Figure 3.15 shows the X-ray pattern of laser deposited cube 1. According to Table 3.4 and Equation (3.1), the input energy density in micro direct metal deposition of cube 1 was 1.2 kJ/mm². XRD pattern of cube 1 shows major NiTi (B2) peaks and minor NiTi₂ and NiTi (B19). EDS analysis confirms the XRD result (Figure 3.16).

The fundamental and superlattice peaks of B2–NiTi are shown in Table 3.5. No superlattice line can be seen in XRD patterns of cube 1 and disordered B2–NiTi phase appears. This can be attributed to the defects induced by high-energy ball milling and rapid solidification [72]. Formation temperature of NiTi (1310 °C) is higher than NiTi₂ (984°C) according to the Ni-Ti phase diagram shown in Figure 3.17. XRD pattern of cube 1 shows that; to obtain single phase NiTi more input energy is necessary. In fact, high input energy increases the melt pool temperature and causes melting of Ti-rich intermetallics such as NiTi₂.

Table 3.5– The fundamental and superlattice peaks of NiTi B2 phase, Cu $K\alpha$ radiation [72]

Fundamental peaks of NiTi		Superlattice peaks of NiTi	
Angle (2θ) (deg.)	hkl	Angle (2θ) (deg.)	hkl
42.6	1 1 0	29.7	1 0 0
61.8	2 0 0	52.9	1 1 1
78.3	2 1 1	70.1	2 1 0
93.44	2 2 0		

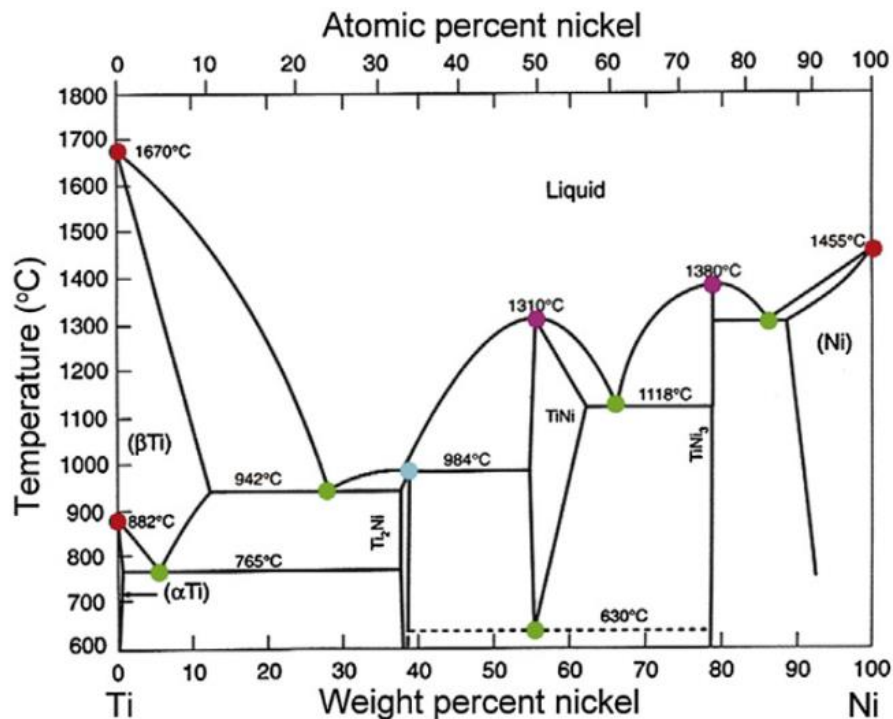


Figure 3.17– Ni-Ti phase diagram [73]

By increasing this energy, the temperature of melt pool increases and NiTi single phase is accessible. It is noteworthy to mention that heat treatment after laser melting such as solid solution heat treatment has been used to obtain single phase NiTi. However, in this thesis, the focus was on the elimination of unwanted secondary phases by manipulation of process parameters during the laser melting. According to equation (1), input energy is a function of power, spot diameter and scanning speed of the laser. An increment in the laser power increases the input energy and the experiments show that high power facilitates the evaporation and reduces the process efficiency. A reduction in scanning speed is another way to increase the

input energy. However, this reduction increases the process time, with a consequent reduction in the process efficiency. The increase of the internal energy of the initial powder due to the heating of the substrate is another way to increase the temperature of melt pool. During the laser deposition, the internal energy of milled powder particles is added to the input energy from laser deposition. It seems that longer milling times increase the energy from the mechanical alloying process and facilitate the NiTi formation. According to Figure 3.16, EDS analysis shows that, after laser deposition of Ni₅₀Ti₅₀ powder alloy, NiTi develops rich of Ti. The high temperature produced during the laser processing is responsible for the loss of nickel percentage after laser deposition. In fact, the evaporation temperature of Nickel (2732°C) is lower than that of Titanium (3287°C). According to that, powder D and cube 2 were produced by mechanical alloying and micro laser deposition respectively.

Based on the EDS results for laser deposition of cube 1 and unwanted Ni loss, the quantity of Ni in initial powder was raised from 50% to 50.8% in powder D to compensate the evaporation of Ni during laser deposition. Heating the substrate during the process may improve the homogeneity of product and facilitates the formation of NiTi as well.

Figure 3.18 shows that by increasing the time of milling from 8h to 10h, Ni percentage from 50 to 50.8 and the temperature of substrate from 25°C to 400°C, single phase NiTi develops as a predominant phase even at high scanning speed. An increase of the time of milling leads to a more homogeneous Ni-Ti composite and makes the development of single phase NiTi easier after laser deposition as a consequence both of the higher inner energy accumulated into the particles and of the decrease in diffusion distances (interlamellar spacing) as well. High temperature of melt pool inhibits the formation of NiTi₂ and other unwanted intermetallics. It means that, it is possible to increase the speed of production using mechanically alloyed powders.

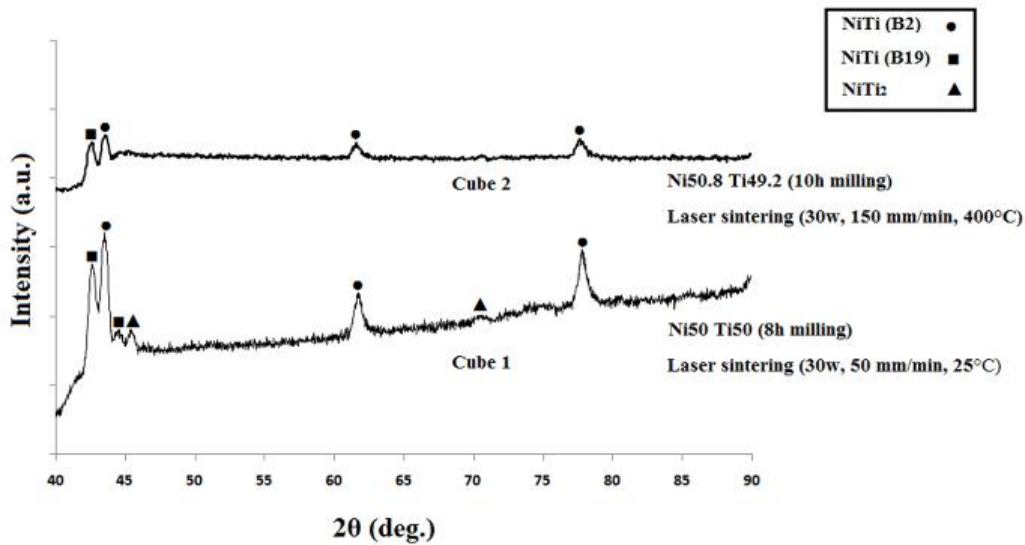


Figure 3.18– X-ray patterns of NiTi cubes 1 and cube 2 (see Table 3.4)

In order to analyse the effect of powder pre-heat treatment on phase composition of laser deposited NiTi alloy, powder E (Table 3.3) was prepared by heat treating of powder D at 1080°C for 8h. Figure 3.19 shows XRD pattern of 10h milled Ni_{50.8}Ti_{49.2} before and after heat treatment. It is clear that after heat treatment unwanted intermetallic NiTi₂ and Ni₄Ti₃ were formed. It can be attributed to high temperature and long process time.

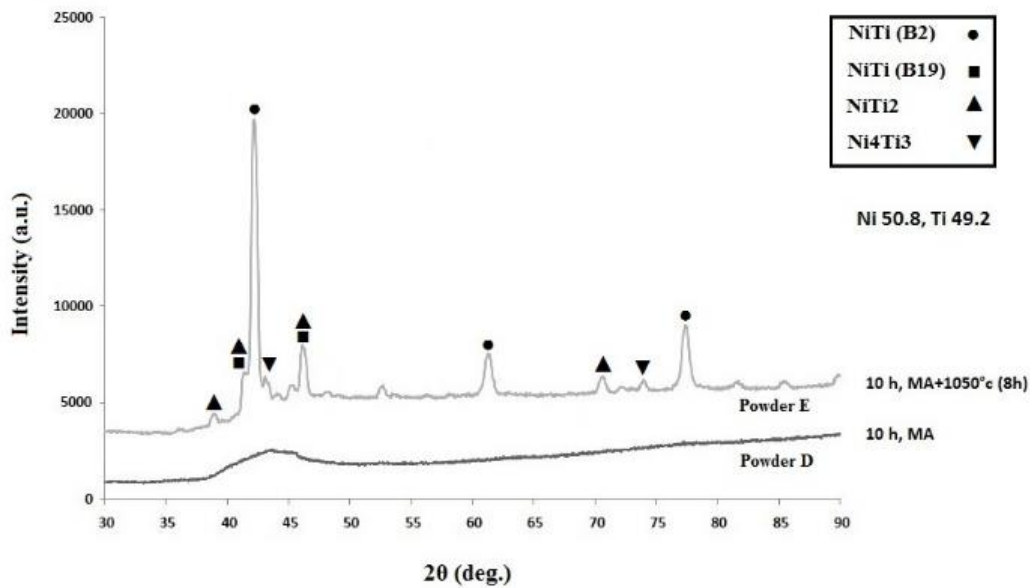


Figure 3.19– X-ray patterns of 10h mechanically alloyed Ni_{50.8}Ti_{49.2} before (powder D) and after (powder E) heat treatment

Figure 3.20 shows the morphology of powder particles before and after heat treatment. The surface of powder particles is smoother after heat treatment. Line scan analysis on cross section of powder particles before and after heat treatment revealed that the powder without heat treatment has higher homogeneity for both Ni and Ti than heat treated powder (Figure 3.21). This is due to the formation of different intermetallics after heat treatment of mechanically alloyed Ni_{50.8}Ti_{49.2}.

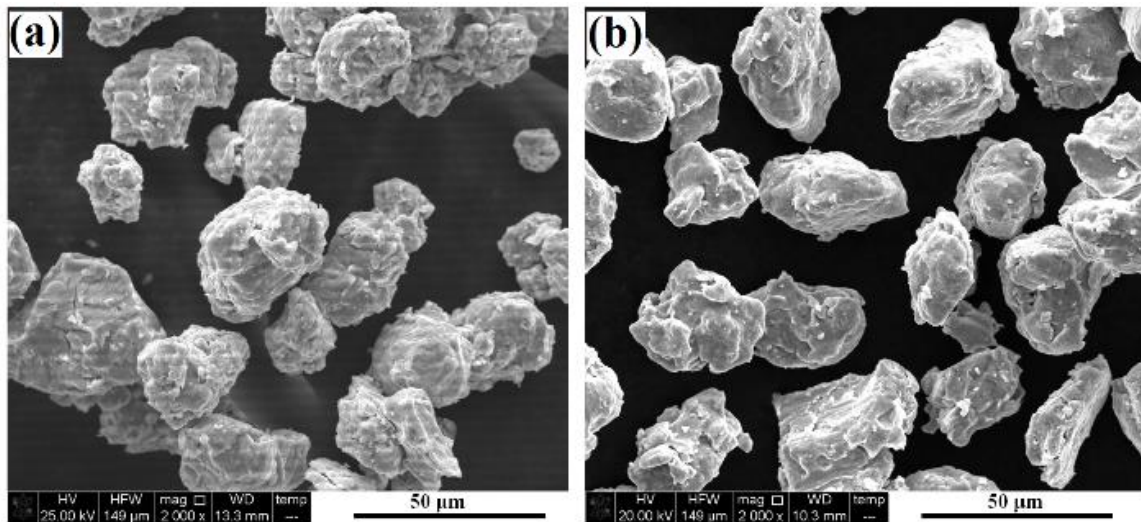


Figure 3.20– SEM micrographs of 10h mechanically alloyed $\text{Ni}_{50.8}\text{Ti}_{49.2}$ before (powder D) and after (powder E) heat treatment

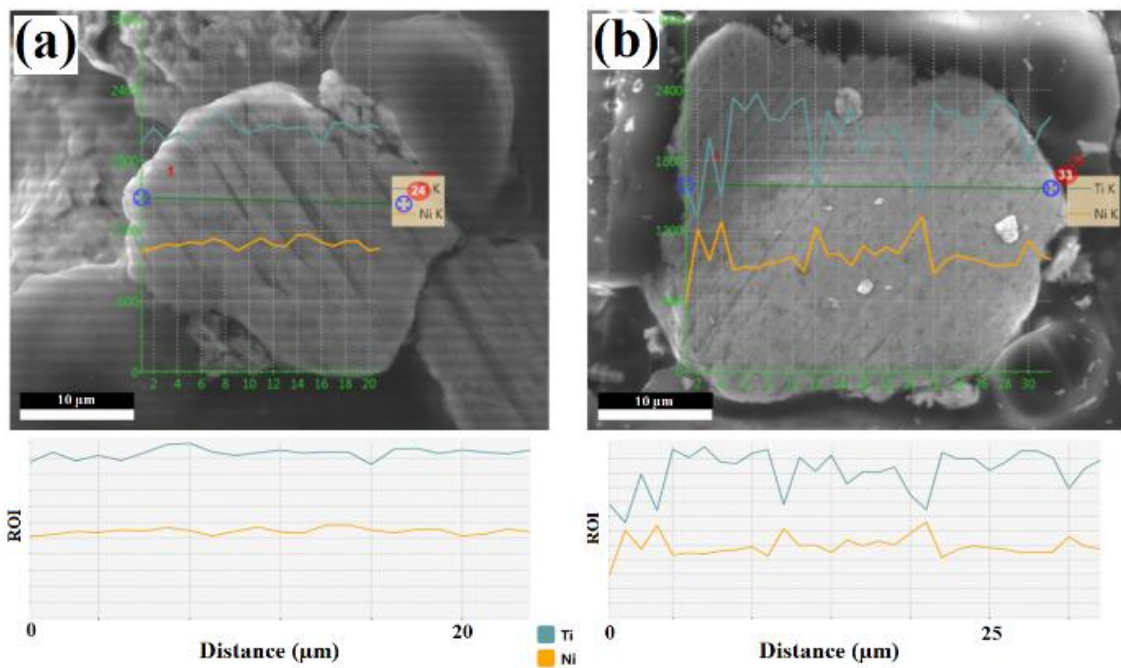


Figure 3.21– EDS analysis of 10h mechanically alloyed $\text{Ni}_{50.8}\text{Ti}_{49.2}$ powder particles (a): before heat treatment (powder D) and (b): after heat treatment (powder E)

Cubes 2 and 3 were produced by laser deposition respectively of powders D and E with the aim to investigate the effect of powder heat treatment on phase composition after μ DMD.

Figure 3.22 shows that heat treatment of mechanically alloyed powder has not significant effect on X-ray diffraction pattern of laser deposited samples. The patterns of both untreated and treated powders after laser deposition mainly consist of NiTi (B2) phase. It is despite of the existence of NiTi₂ and Ni₄Ti₃ in powder E before μ DMD. In fact, unwanted intermetallics are very fine and they can be easily melted thanks to the high temperature produced by micro direct metal deposition [44].

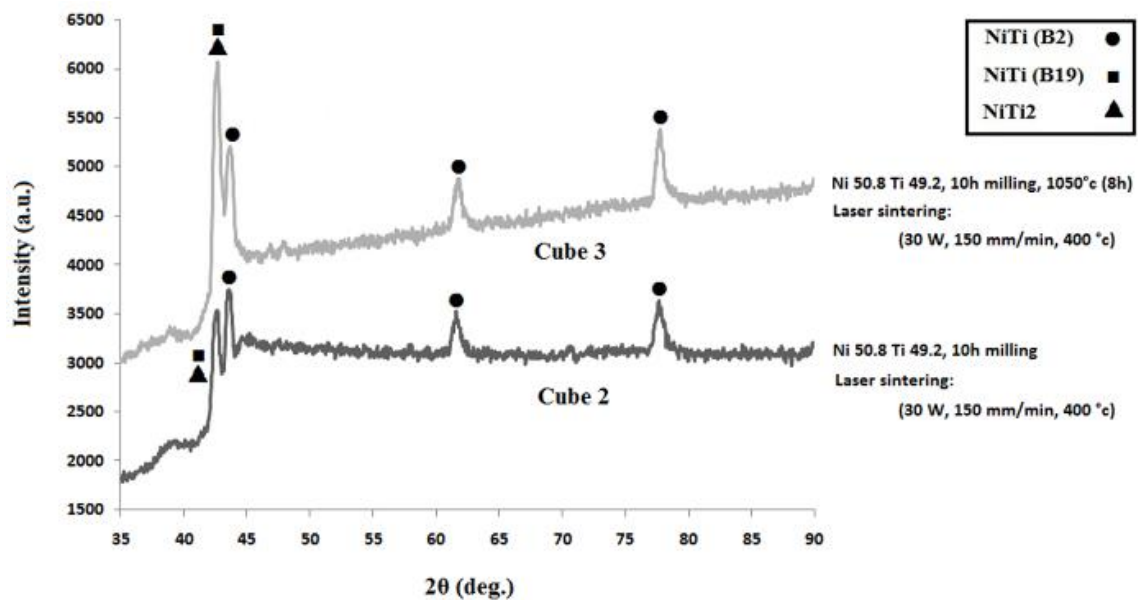


Figure 3.22– X-ray patterns of laser deposited cube 2 and cube 3 (Table 3.4)

3.3 Investigation of micro pores in μ DMD NiTi parts by means of micro computed tomography

Design and investigation of macro and micro pores is a crucial parameter in manufacturing of porous implants. As stated before, micro computed tomography is an interesting non-destructive technique internal defect assessment of additive manufactured parts. In this section, the effect of process parameters on formation and distribution of micro pores was analysed using micro computed tomography and scanning electron microscopy.

3.3.1 Inherent micro porosity in NiTi alloy fabricated by μ DMD

The effects of process parameters on quantity and distribution of inherent micro pores have been studied in this research. Total input energy produced by μ DMD can be calculated using equation (3.6) [74]:

$$E_L = \frac{P}{V \times \Delta z \times d} \quad (3.6)$$

Where P is power of laser, d is diameter of laser focus spot; V is the scanning speed and Δz is the pre-defined thickness of each layer. Increase in layer thickness and scanning speed as main μ DMD process parameters results in decrease of input energy. Low input energy causes discontinuous single tracks and inhibits the formation of 3D parts. On the other hand, at very high level of input energy, the temperature of melt pool increases and evaporation of material may occur. High surface quality and high level of densification are obtainable by adjusting the scanning speed and thickness of layers. Moreover, other parameters such as powder feeding rate and substrate temperature can affect the formation of 3D parts by μ DMD. Heating the substrate can accelerate the formation of melt pool even at low input energies. As it can be seen in Figure 3.23, when the powder feeding rate isn't enough to form a continuous single track, heating of substrate hasn't significant effect on 3D part formation especially at high velocities. But, by increasing the feeding rate from 0.76 mg/sec to 1.26 mg/sec (Figure 3.23 (b)), the effect of substrate's temperature is more sensible. From Figure 3.23 (b), it can be easily understood that an increase in scanning speed reduces the height of single tracks. Moreover, high temperature of substrates facilitates the formation of 3D parts and increases the height of single tracks. In other words, high temperature can compensate the effect of high scanning speed and maintain the rate of growth.

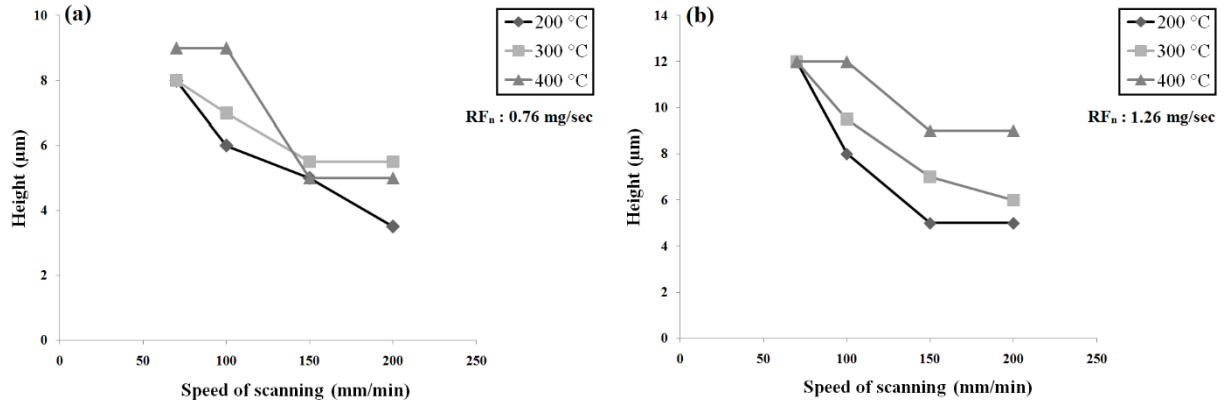


Figure 3.23– Effect of scanning speed and substrate temperature on the height of single tracks produced by μ DMD with (a) 0.76 mg/sec and (b) 1.26 mg/sec powder feeding rates

Single track's height can be considered as nominal layer thickness which is possible to produce with specific μ DMD process parameters. Nominal height (NH) of a thin wall which consists of successive single tracks can be simply calculated using equation (3.7):

$$NH = n \times H \tag{3.7}$$

Where NH is the nominal height of thin wall, n is the number of layers and H is the nominal thickness of single track. As can be seen in Figure 3.24, 10% overlap between the layers in thin walls decreases the difference between the nominal height and the experimental height.

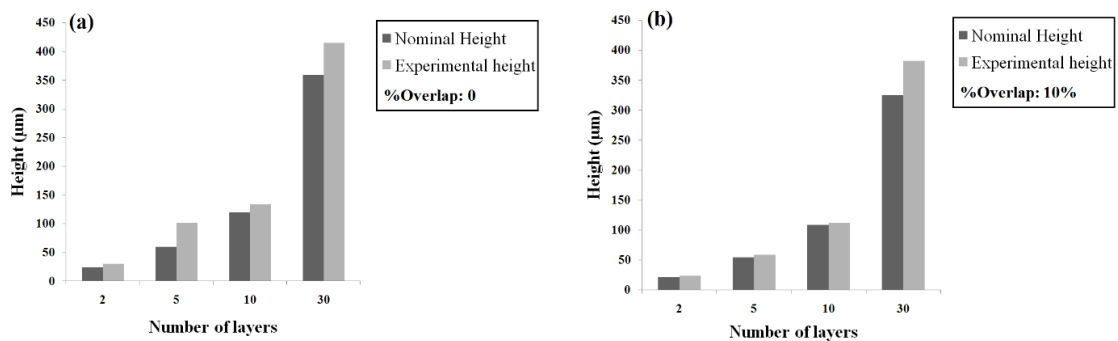


Figure 3.24– Effect of layer overlap in fabrication of NiTi thin walls by μ DMD (a) without overlap between layers, (b) with 10% overlap between layers.

It is notable to say that, the experimental heights are usually more than expected nominal heights driven from equation (3.7); this can be attributed to the temperature of substrate. In fact, accumulation of heat input, increases the temperature of melt pool and subsequently the rate of melting.

Figure 3.23 shows that by increase in substrate temperature, the height of single tracks and consequently the thickness of layers in thin walls increases. Geometry analysis using μ CT scanning revealed that, by inserting the overlap between the layers in μ DMD process, regular thin walls are obtainable (see Figure 3.25 (b, d)). The rate of growth at the beginning and the end of wall is more than in the central parts of the walls without interlayer overlap. This can be attributed to the layer thickness. As stated before, high pre-defined ΔZ for laser movement results in low input energy which inhibits 3D part formation (Figure 3.25 (a, c)). However, higher parts exist at the beginning and the end of thin walls because of more exposure time that occurs when the laser changes the direction of traveling between the layers. As it can be seen in Figure 3.25 (c, d), by increasing the temperature of substrate from 200 °C to 300 °C, the heights of thin walls totally increase. Similar heat treatment was proposed by Shishkovsky et al. [75] to obtain dense and crack-free NiTi parts by laser sintering. Twelve different thin walls were selected for inherent micro porosity analysis using μ CT. The results are included in Table 3.6 which shows that the mean size of inherent micro pores is almost the same for all thin walls (approximately equal to 20 μ m) and is independent of process parameters. As stated before, these micro pores are produced by melting and have spherical shapes. As it was observed by SEM analysis, which will be presented later, inherent micro pores have diameters in the range of 2-50 μ m. However, pores with diameters below 12 μ m (i.e. volumes below about 8 voxels) were not considered in the μ CT analysis, as they were considered too near the μ CT resolution limit and hence they could be influenced by the noise of μ CT data. Inserting the overlap between the layers at constant temperature decreases the inherent micro porosity percentage. The distribution of inherent micro pores in thin walls with 30% overlap between the layers is likely to be more homogenous in comparison with the walls without interlayer overlap, as it is shown for example in Figure 3.25 (a) and (b).

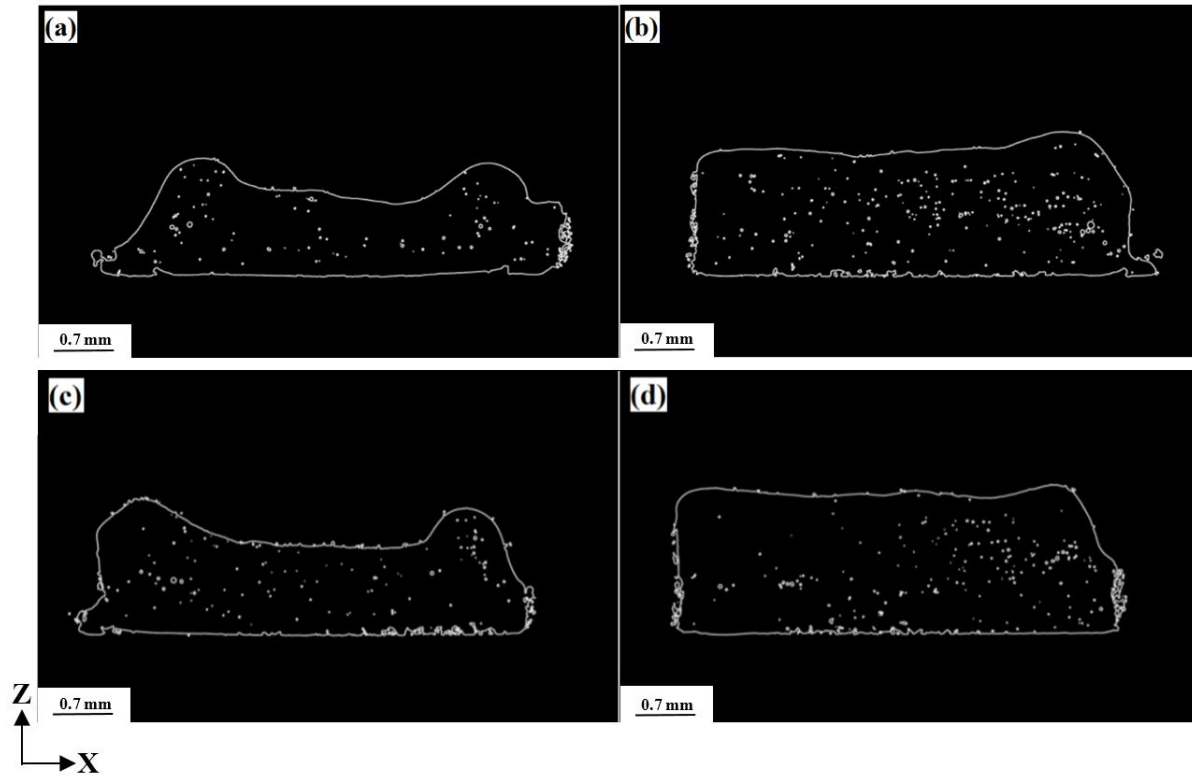


Figure 3.25– Effect of layer overlap and temperature of substrate on shape and inherent micro porosity distribution of thin walls (a): $T=200\text{ }^{\circ}\text{C}$, $V=150\text{ mm/min}$, $\%OV=0\%$, porosity =1.49%, (b): $T=200\text{ }^{\circ}\text{C}$, $V=150\text{ mm/min}$, $\%OV=30\%$, porosity = 0.98%, (c): $T=300\text{ }^{\circ}\text{C}$, $V=70\text{ mm/min}$, $\%OV=0\%$, porosity =1.01%, (d): $T=300\text{ }^{\circ}\text{C}$, $V=70\text{ mm/min}$, $\%OV=30\%$, porosity =0.79%

Table 3.6– Inherent micro porosity analysis of NiTi thin walls using μ CT scanning

wall	V (mm/min)	T (°C)	OV%	d _{IMP} (μ m)	Porosity (%)	Mean height (mm)
1	70	200	0	19.64	0.84	0.9
2	150	200	0	18.07	1.49	1.37
3	70	200	30	19.27	0.92	1.43
4	150	200	30	21.00	0.98	1.63
5	70	300	0	20.34	0.72	1.13
6	150	300	0	20.34	1.01	1.11
7	70	300	30	20.34	0.72	1.61
8	150	300	30	20.00	0.79	1.46
9	70	400	0	18.07	1.29	1.14
10	150	400	0	17.63	1.37	0.78
11	70	400	30	18.49	0.96	1.47
12	150	400	30	19.27	0.85	1.13

P: 30 W, NH: 1 mm, d_{IMP}: mean diameter of inherent micro pores, OV%: overlap.

From Figure 3.26 (a), it was concluded that heating the substrate up to 300 °C can reduce the inherent micro porosity percentage in NiTi thin walls. However, increasing the temperature of substrate up to 400 °C caused to increase in porosity percentage. This phenomenon can be explained by evaporation of NiTi because of high temperature of melt pool. This high temperature comes from the accumulation of input energy of μ DMD process and temperature of substrate. Same trend also exists for the walls with 30% overlap between the layers (Figure 3.26 (b)).

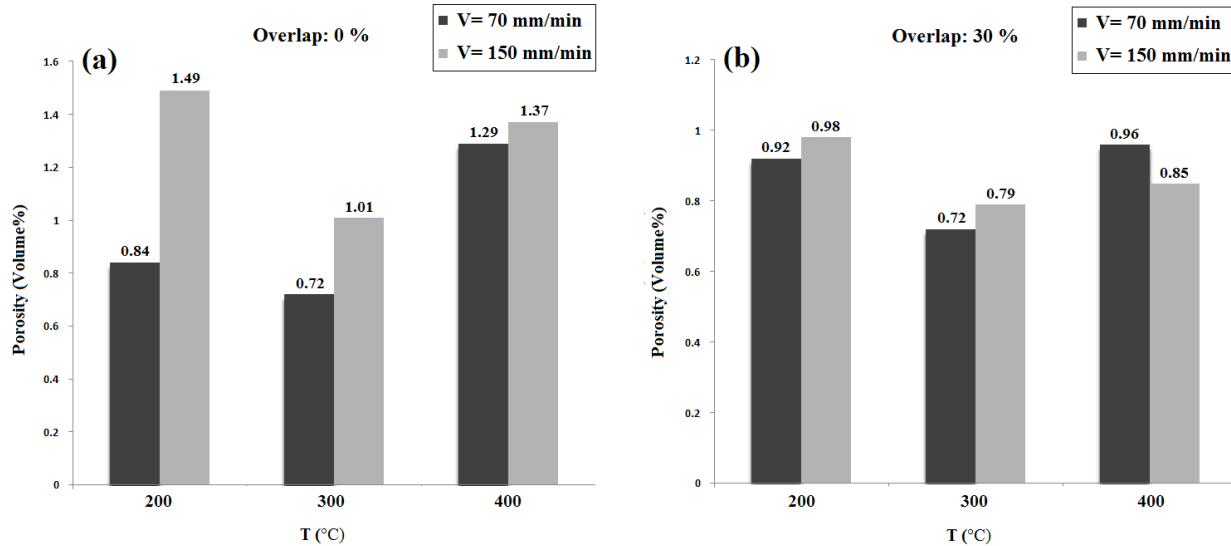


Figure 3.26– Effect of scanning speed and temperature of substrate on inherent micro porosity of NiTi thin walls produced by μ DMD (a): without overlap between the layers, (b): with 30% overlap between layers

According to Figure 3.27, remelting the previous layer in the wall with overlap can reduce the inherent micro porosity in these walls. In fact, the effect of temperature in μ DMD is twofold. Because of small laser focal spot in μ DMD, input energy and consequently melt pool temperature are so high. Moreover, overlap between the layers increases the input energy produced by μ DMD process and consequently increases the melt pool temperature. Generally, high temperature in laser melting process results in high density product formation that was reported by others [76]. But, using elevated temperature for substrate and overlap between the layers at the same time in μ DMD encourages evaporation in the melt pool and increases the porosity (see Figure 3.27).

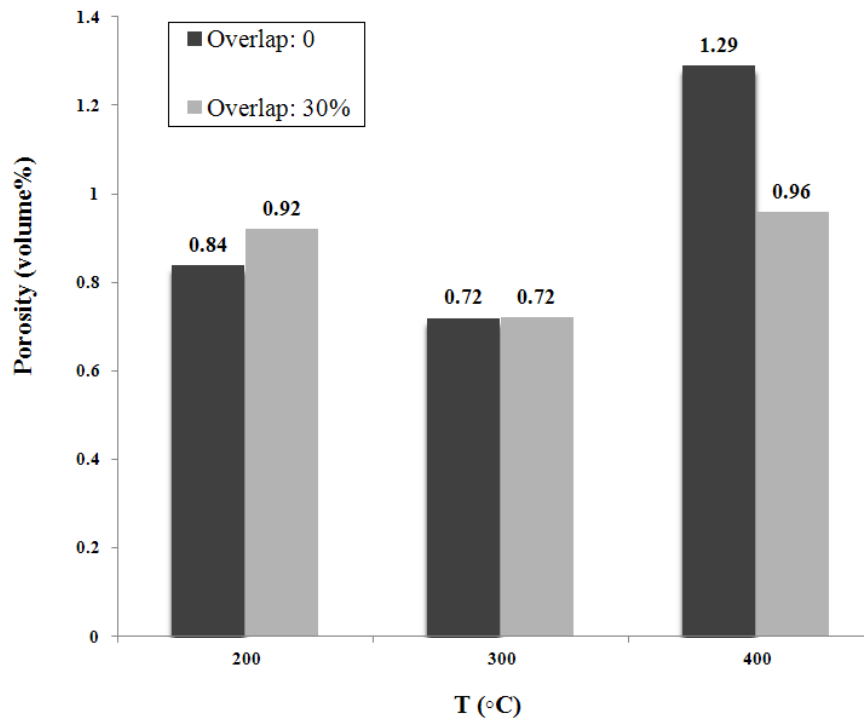


Figure 3.27– Effect of layer overlap and temperature of substrate on inherent micro porosity of NiTi thin walls produced by μ DMD

3.3.2 Controllable micro porosity in μ DMD NiTi parts

As presented in the previous section, melting can produce inherent micro pores with spherical shape and about 20 μm mean pore sizes. It is not easy to manipulate the size, morphology and distribution of inherent micro pores. In the other hand, controllable micro pores are possible to fabricate using specific process parameters and CAD models [77]. Hatch distance and strategy of scanning are two important parameters in μ DMD and their effects on micro porosity of NiTi cubes is discussed in this section. Strategy of scanning can affect the surface quality and pore characteristics of the parts produced by μ DMD. To evaluate the effect of hatch distances on micro porosity formation in micro laser melted products, 3 cubes were fabricated by 3 different hatch distances. As shown in Figure 3.28 (a), when the hatch distances are small, there are overlaps between the single tracks and consequently the micro pores are small and the distribution of pores is not homogenous. Increase in hatch distances decreases the overlap between the tracks. This makes the morphology of pores more regular. Figure 3.28 (a) shows

that near fully dense structure has been formed using 100 μ m hatch distance. For further investigation, five NiTi cubes with different scanning strategies were fabricated according to Table 2.4 using 100 μ m hatch distances.

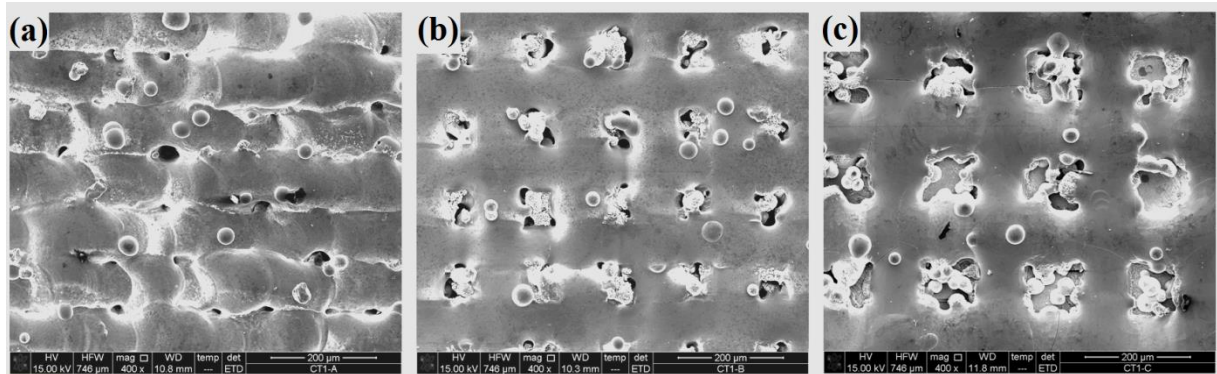


Figure 3.28– SEM micrographs of top surface of NiTi cubes produced by μ DMD with (a) 100 μ m, (b) 150 μ m, (c) 200 μ m hatch distances. ($T = 200$ °C, $P = 30$ W, $V = 100$ mm/min, $\Delta Z = 4$ μ m, RF_n : 1.26 mg/sec, strategy of scanning: strategy B according to Table 2.4)

Figure 3.29 shows the scanning electron micrographs after polishing of NiTi cubes produced by different strategies of scanning according to Table 2.4. As it can be seen in Figure 3.29, when a 90° rotation is applied between the layers (strategy B and E), the distribution of micro pores is more homogeneous and the pores are smaller and more rounded in comparison with the other strategies. Quantitative micro pore analysis of NiTi cubes produced by different scanning strategies is presented in Figure 3.30, which shows that different strategies of scanning produce different porosity percentages and different pore sizes. Also, the trends of both graphs related to porosity percentages and micro pore sizes are the same. It is noteworthy that in the data presented in Figure 3.30, both inherent and controllable micro porosity have been considered. So, it can be concluded that, using the same μ DMD process parameters and different scanning strategies it is possible to manipulate the micro pore's size and morphology, which can be used to produce porous scaffolds with specific porous structures.

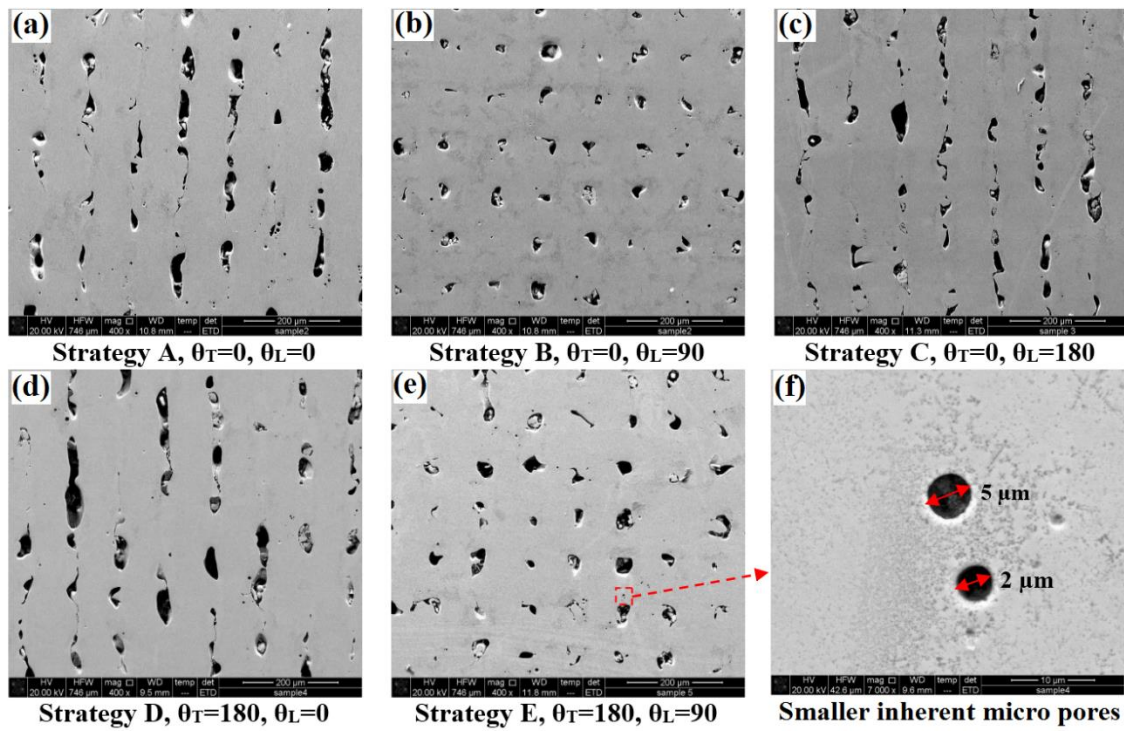


Figure 3.29– SEM micrographs were taken of top surface of μ DMD NiTi cubes produced by (a) strategy A, (b) strategy B, (c): strategy C, (d) strategy (D), (e) strategy E of scanning according to Table 5, (f) small inherent micro pores in higher magnification

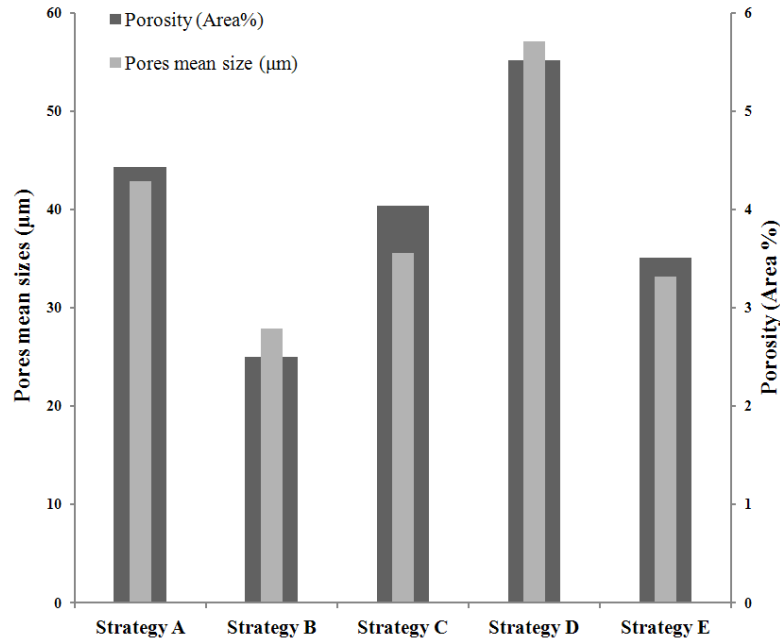


Figure 3.30– Total porosity percentages and mean value of micro pore's sizes in micro laser melted NiTi cubes produced by different strategies of scanning

Using image analysis method, it is possible to define pore's shape distribution in 2D images taken by SEM. P_C is the percentage of pores with specific range of circularity values (C) and can be written as:

$$P_C = (N_C/N_t) \times 100\% \quad (3.8)$$

Where, N_c is the number of micro pores with defined range of circularity and N_t is the total number of micro pores in selected 2D area. A circularity value of 1.0 indicates a perfect circle. As the value approaches 0.0, it indicates an increasingly elongated polygon. As shown in Table 3.7, the maximum number of rounded micro pores (circularity: 0.6-1) is related to strategy E that confirms the previous findings.

Table 3.7– Micro pore’s shape analysis of NiTi cubes (top surface) produced by different scanning strategies according to Table 2.4

Strategy	P_C: 0-0.3	P_C: 0.3-0.6	P_C: 0.6-1
Strategy A	55%	47%	18%
Strategy B	53%	50%	18%
Strategy C	56%	46%	14%
Strategy D	54%	45%	12%
Strategy E	44%	40%	27%

Surface roughness of NiTi cubes produced by different scanning strategies was measured using 3D optical micrographs that are presented in Table 3.8. Table 3.8 shows that despite of lateral irregularity of NiTi cubes which have 90° rotation between successive layers (strategy B and E), the surface roughness of these two strategies are lower than the other strategies. In other words, the quality of surface is better when the angle between tracks and layers are 0° and 90° respectively. Also, using strategies B and E, results in minimum porosity percentage and minimum average pore size as presented before in Figure 3.30.

Table 3.8– Surface quality of NiTi cubes

Strategy	Track's angle	Layer's angle	Ra (μm)	Total Porosity (%)
Strategy A	0	0	61.45	4.43 %
Strategy B	0	90	39.28	2.50 %
Strategy C	0	180	65.71	4.04 %
Strategy D	180	0	103.96	5.52 %
Strategy E	180	90	52.46	3.51 %

3.4 Textural evolution during μ DMD of NiTi alloy

The effect of scanning strategy on grain growth and textural evolution has been investigated using scanning electron microscope equipped with electron backscattered diffraction detector and presented in this section.

The microstructures of μ DMD fabricated NiTi cubes in scanning plane (RD-TD) are shown through EBSD inverse pole figures orientation maps (OIM) in Figure 3.31 (a), (b) and (c) for three different scanning strategies A, C and D according to Table 2.4. Selection of small regions of interest for microstructural investigation is due to the fine grains and almost same distribution of grain sizes on the surface of laser melted cubes. As shown before through XRD analysis, $\text{Ni}_{50}\text{Ti}_{50}$ (Nitinol) intermetallic phase is the predominant phase in μ DMD process of mechanically alloyed $\text{Ni}_{50.8}\text{Ti}_{49.2}$ powder mixture (see also Figure 3.31 (d), (e) and (f)).

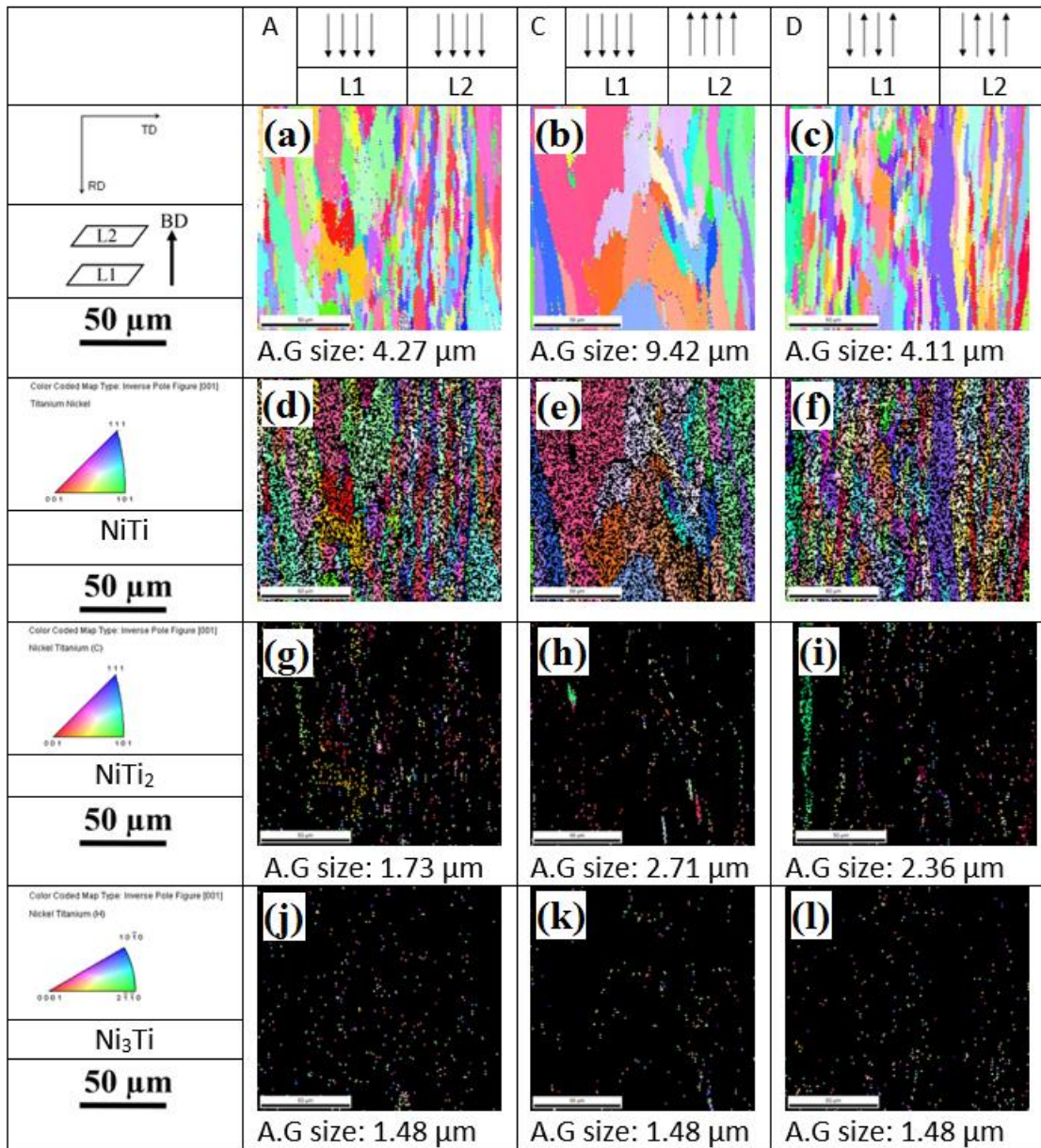


Figure 3.31– EBSD orientation maps from the top view of the μ DMD-processed NiTi samples representing three main phases distribution in three scanning strategies of A, C and D according to Table 2.4, (a, b, c): all phases, (d, e, f): NiTi, (g, h, i): NiTi₂, (j, k, l): Ni₃Ti. The scanning (RD-TD) and building (BD) directions are indicated by the black arrows on the top left

As can be seen in Figure 3.31 (g-i), small quantity of NiTi₂ intermetallic phase with the average grain size of 1-3 μ m presents in microstructure. Furthermore, Ni₃Ti intermetallic phase with the grain size of below 2 μ m was detected in all three samples (Figure 3.31 (j-l)). These findings also are consistent with previous results on phase composition of μ DMD processed NiTi parts that were based on X-ray diffraction analysis. It is well understood that laser melted builds have a banded grain structure with alternate coarse and fine grain bands due to different cooling rates, where the fine grains are typically found in the locations associated with rapid cooling rates [18], [78]. Overall overview of Figure 3.31 (a-c) depicts that, the average grain size of NiTi parts produced by μ DMD process is below 10 μ m which is smaller than previously obtained grain sizes in conventional DMD process of NiTi [79]. This difference may be ascribed to the smaller melt pool and consequently severe rapid solidification in μ DMD process with respect to conventional DMD process. Both elongated and equiaxed grains can be readily observed in three orientation maps taken from samples A, C and D (Figure 3.31 (a-c)). However, elongated grains are more and finer in samples A and D (produced by $\theta_L=0$) than sample C (produced by $\theta_L=180$). Additionally, the samples produced by strategies A and D have smaller grain sizes (average ~ 4 μ m) than sample produced by strategy C (~ 9 μ m) on RD-TD plane. It is also noteworthy to say that, there is no significant difference between samples produced by both strategies A and D with same θ_L in grain size distribution on RD-TD cross section. Neighbouring laser scanning paths in one layer are unidirectional and bidirectional for strategies A and D respectively. It can be concluded that, the angle between neighbouring laser scanning paths in RD-TD plane (θ_T) has not significant effect on the microstructure of μ DMD processed builds and the angle between neighbouring single tracks in successive layers (θ_L) may control the microstructure.

It has been reported that in thin walls produced by DMD process and unidirectional single tracks ($\theta_L = 0$), the morphology of grains in building direction (BD) is columnar and the main axis of almost all grains are aligned [79]. Dinda et al. [21] showed that bidirectional movement of laser ($\theta_T = 180$) in production of thin walls by DMD led to a microstructure with coarse grains due to epitaxial growth phenomenon. According to Table 2.4, NiTi cubes fabricated by scanning strategies A and D consist of thin walls and these thin walls likewise consist of unidirectional single tracks. In the other hand, strategy C produces NiTi cube that is made of

thin walls with bidirectional single tracks. As shown in Figure 3.31 (a, b and c), the surface microstructures of NiTi cubes produced by μ DMD and strategies A, C and D are in agreement to the findings of others in thin wall production by DMD process. Hufmeister et al. [80] concluded that the grain structure gets coarser with increase in build height due to the reduction of the heat sink effect of the substrate. The same interpretation can be attributed to surface microstructure of sample C in this study which contains bidirectional neighbouring single tracks in successive layers (Figure 3.31 (b)).

In direct metal deposition process, substrate or previous layer act as a heat sink and the heat flow is almost unidirectional. Hence, in BD cross-section, the majority of grains have same axis which is parallel to the heat flow direction and lead to columnar microstructure. This preferential growth direction is $\langle 100 \rangle$ in cubic crystallographic systems. Generally, solidification occurs through nucleation and growth. Occasionally, the nucleation or growth can control the solidification phenomenon (predominant phenomenon). For instance, if DMD process is implemented on a single crystal substrate while the $\langle 100 \rangle$ axis of the substrate is parallel to heat flow direction, solidification occurs through epitaxial growth of substrate and single crystal microstructure continues to the surface of build. In the other hand, when DMD process is carried out on a polycrystalline substrate, only those grains that have at least one $\langle 100 \rangle$ crystallographic direction parallel to heat transfer direction, will participate in growth phenomenon. In this step, if no grain has a $\langle 100 \rangle$ crystallographic direction parallel to heat transfer direction, nucleation of new grains happens and solidification continues through these new grains. It can be concluded that, in μ DMD process, when neighboring single tracks in successive layers are unidirectional ($\theta_T=0$, strategies A and D according to Table 2.4), considering the polycrystalline nature of substrate, columnar grains grow opposite to heat transfer direction and polycrystalline microstructure develops. Considering the small size of melt pool in μ DMD process and consequently rapid solidification of the melt pool, the angle between the neighbouring single tracks (θ_T) in on layer has not significant effect on the surface microstructure.

As stated before, sample C consists of thin walls with bidirectional single tracks. It should be mentioned that this rotation between successive single tracks leads to the change in main axis of grains in each layer. Dinda et al. [21] showed that in DMD process of Ni superalloy, the

change in main axis is about 90° and the grain sizes in BD increase significantly by approaching to the surface. As can be seen in Figure 3.31 (b), strategy C with 180° rotations between the layers led to equiaxed grains of two times bigger than the mean grain size in samples produced by strategies A and D. In thin wall fabrication using DMD concept and unidirectional strategy of scanning (same as strategies A and D in this study, see Table 2.4), the dendrites are unidirectionally oriented at an angle of $50\text{-}60^\circ$ to the substrate. In the other hand, the dendrites are oriented in a zigzag model when bidirectional scanning strategy is used (same as strategy C in this study, see Table 2.4). Thus, dendrites have intersection at the interface between the layers by an angle of $90\text{-}100^\circ$ [6].

Moreover, a banded fine grain structure exists between the successive layers in DMD processed builds. This fine grained region can act as nucleation sites for the dendrites in following layers and leads to fine equiaxed grains in the next layers. It should be mentioned that the heat input of μ DMD process is high enough for epitaxial growth from the previous layer instead of re-nucleating. However, the orientation of dendrites in previous layer inhibits epitaxial growth when there is a unidirectional scanning strategy (strategies A and D).

The orientation colors in Figure 3.31 (a, b and c) are related to surface normal-projected inverse pole figures (IPFs). In these figures, the crystals on the surface which have a $\langle 111 \rangle$ axis parallel to the surface normal are blue. Red and green points are related to the crystals that have $\langle 100 \rangle$ and $\langle 110 \rangle$ directions parallel to surface normal. Intermediate orientations are coloured by an RGB mixture of the primary components. As stated before, in contrast to sample C, mainly elongated grains can be seen in RD-TD cross section of both samples A and D. However, these elongated grains didn't show a strong crystallographic texture as evidenced by the different colors in OIMs (Figure 3.31 (a, c)). In the other hand, when there is a bidirectional laser path for neighbouring single tracks in successive layers (strategy C), secondary dendritic arms act as nuclei and instead of nucleation of new grains, the growth phenomenon continues through these arms [21]. It can be attributed to this fact that the free energy of growth phenomenon is lower than that for nucleation. In this case and considering the cubic lattice of NiTi, majority part of the growth phenomenon will be in epitaxial form from those crystals which have $\langle 100 \rangle$ direction parallel to heat transfer direction. Consequently, the number of grains decreases and the grain size on the sample surface increases (see Figure 3.31 (b)).

Keeping this hypothesis, the corresponding pole figures (PFs) derived from the IPFs are presented in Figure 3.32. Investigation of the pole figures indicates a strong $\langle 100 \rangle \parallel$ RD fiber texture of 11.5x random for μ DMD processed NiTi sample using strategy C (Figure 3.32 (f)). It has been reported that [79] directionally solidified structure with epitaxial growth parallel to the (001) planes presents in DMD processed In718. (001) is the direction of the maximum thermal gradient, as this is the crystallographic favoured orientation for cubic metals. Moreover, the fine grain regions were generally found to have a more random texture than the columnar grains thus the intensity of texture in NiTi cube produced by strategy C is much higher than strategies A and D. Additionally, Figure 3.31 (b) related to NiTi cube produced by strategy C shows that a majority of the grains have $\langle 001 \rangle$ direction and less frequently $\langle 101 \rangle$ direction along the RD direction which is parallel to the under investigation plane.

Orientation distribution functions (ODFs) as presented in Figure 3.33 depict a strong but discontinuous β fiber texture for μ DMD processed NiTi samples from strategies A (Figure 3.33 (a)) and D (Figure 3.33 (c)) containing unidirectional neighbouring single tracks in consequent layers. The discontinuous β fiber texture [81] indicates some rotational orientation clustering about the texture peaks. These features of the ODF are consistent to nonuniform $\{111\}$ peak distribution in the ring structure in the (111) pole figures as presented in Figure 3.32 (a, d and g). Similar findings have been reported by Dinda et al. [21] for thin walls. They concluded that unidirectional laser beam scanning pattern ($\theta_L=0$) developed a fiber texture; conversely, a backward and forward scanning pattern ($\theta_L=180$) developed a rotated cube texture in the deposit.

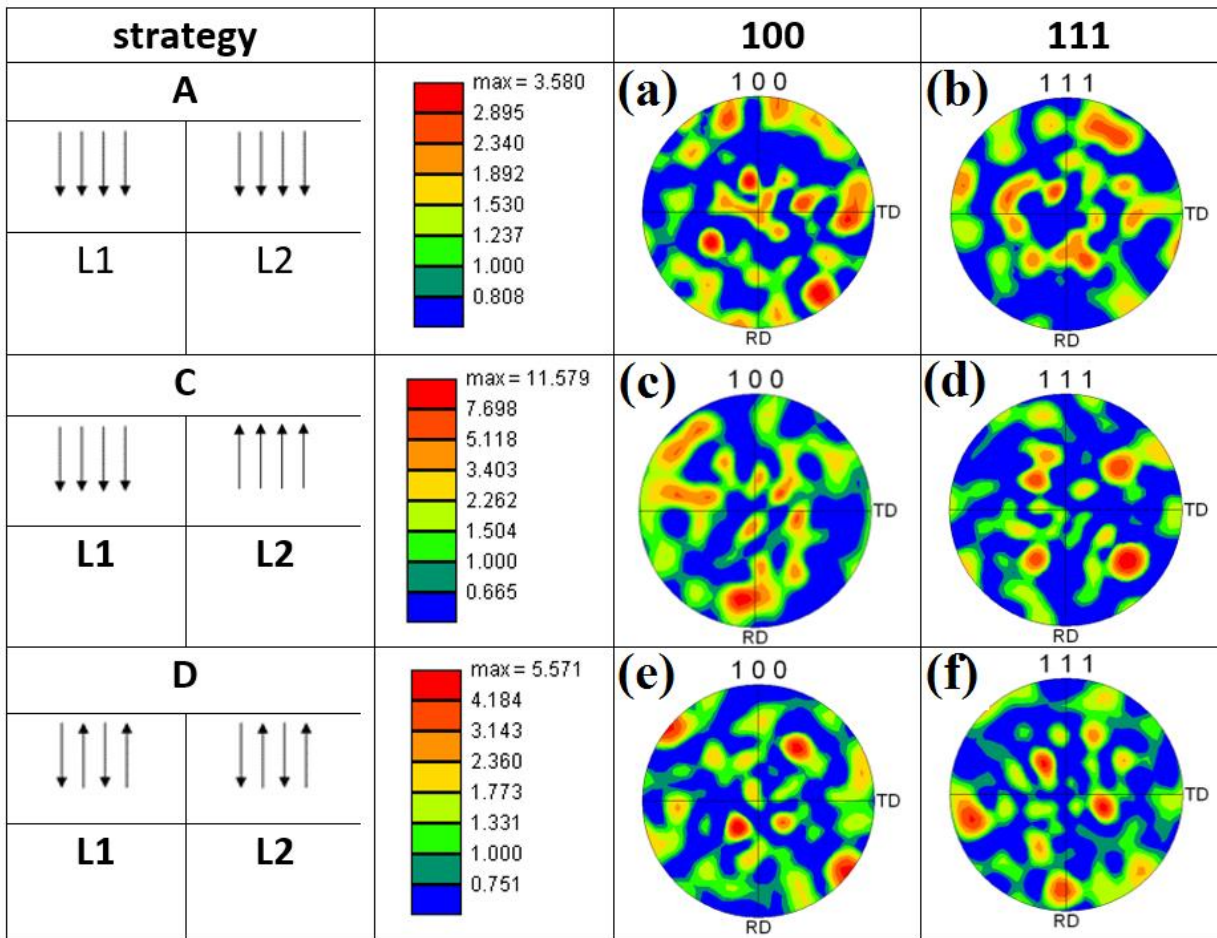


Figure 3.32– The corresponding (100) and (111) pole figures (PFs) of NiTi cubes produced by strategies A (a, b), strategy C (c, d) and D (e, f) according to Table 2.4

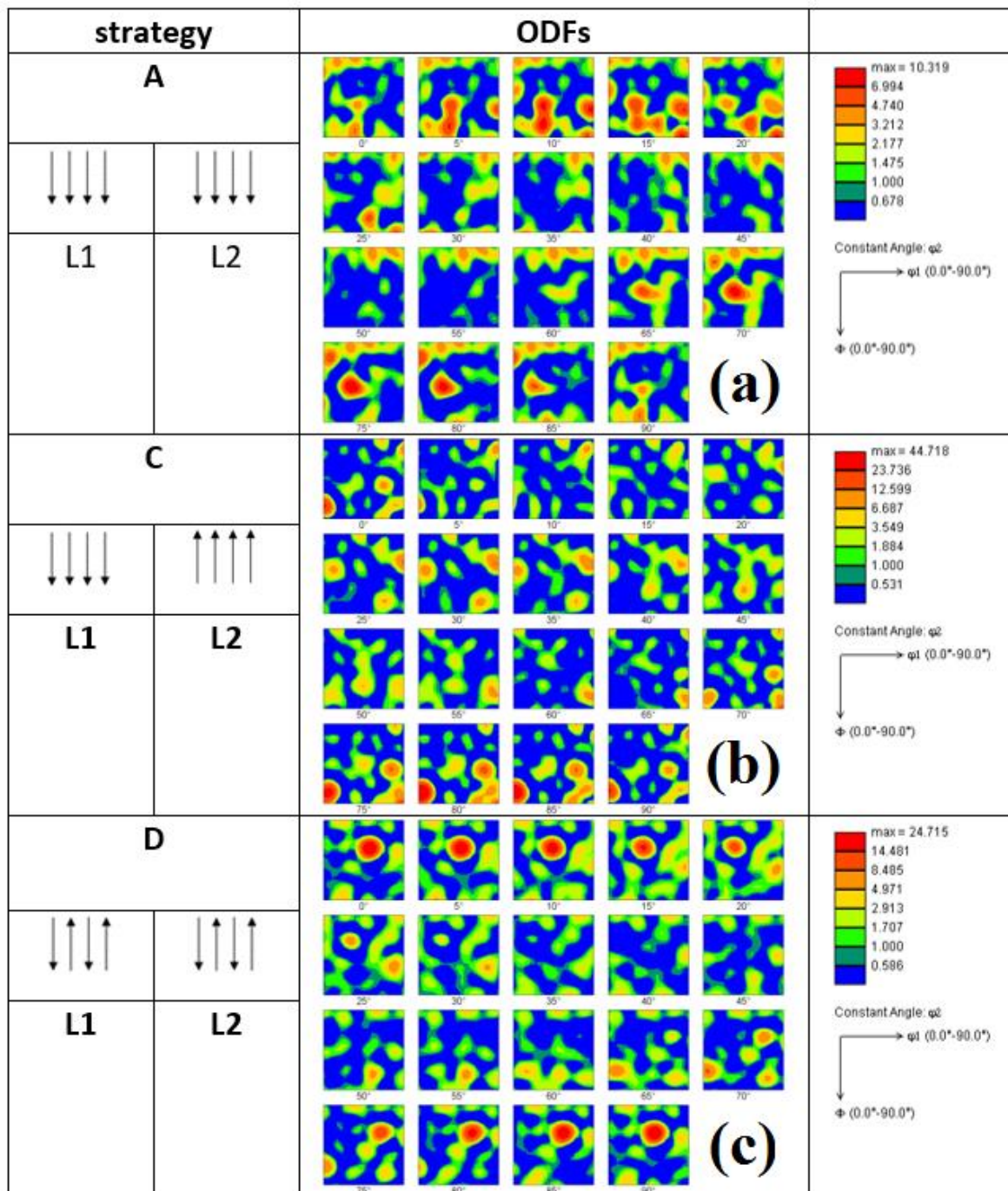


Figure 3.33– orientation distribution function (ODF) plots of the μ DMD fabricated NiTi samples corresponding to the EBSD scans shown in Fig. 4, (a) strategy A, (b) strategy C and (c) strategy D according to Table 2.4

3.5 Microfabrication of NiTi parts using micro direct metal deposition

In this section, micro manufacturing of NiTi powder alloy using micro direct metal deposition is presented. Micro direct metal deposition has been optimized through a set of process parameters and designed experiments to improve the geometrical accuracy and repeatability of micro fabrication.

As presented in section 2.1.4, two different geometries (nr 1 and nr 2) have been designed and produced (see Figure 2.11). Design nr 1 was fabricated using two different laser powers 20 W (sample A) and 25 W (sample B).

As it can be seen in Figure 3.34 (a) and (c), when the power of laser is 20 W (sample A), micro porosities exist between single tracks. In this case, the laser beam does not form suitable melt pool because of a low input energy density. The classification and the formation mechanism of micro porosities were presented in section 3.3. The term inherent micro porosity was used for the micro pores that are created by melting process due to shrinkage and localized evaporation phenomena. This kind of porosity is non-controlled and substantial.

In addition, the term controllable micro porosity was used for micro pores that can be manipulated by changing either the hatch distances or the strategy of scanning (which are mentioned here as two main important process parameters in laser melting). Moreover, Figure 3.34 (b) shows that partially melted powder particles exist between single tracks due to the low power of laser and consequently low input energy. As stated before, an increase in the power of laser and a decrease in the scanning speed lead to higher input energy density (E_L) and thicker single tracks [82]. Figure 3.34 (e) shows that with an increase in power of laser from 20 W (sample A) to 25 W (sample B), the melting rate rises and causes a reduction in micro porosity between tracks of sample B. However, Figure 3.34 (f) illustrates that high power of laser and consequently high input energy density result in a more irregular surface. It can be concluded that an increase in the power of laser has a twofold effect: at the same time, it worsens the surface morphology and it decreases the micro porosity between single tracks. It is notable to say that a bad surface finish can increase the dimensional deviations between as-

produced and nominal parts. Deeper investigations were carried out by means of μ CT, focused on internal regions of the NiTi sample produced with 25 W laser power (sample B).

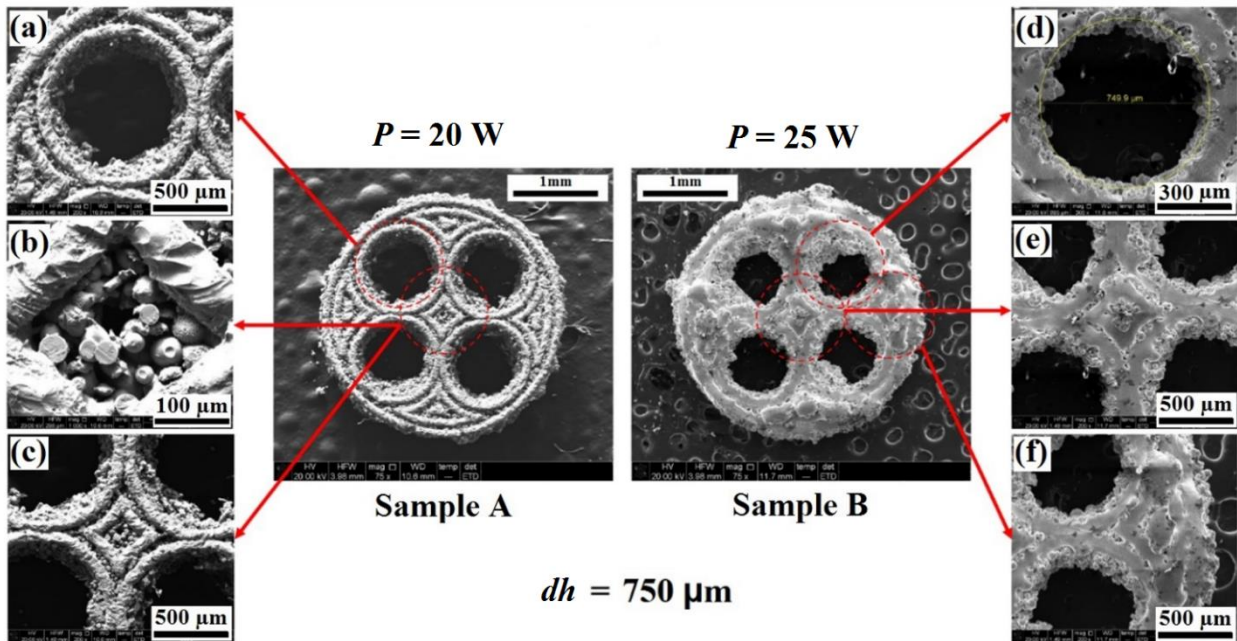


Figure 3.34– Scanning electron micrographs of NiTi samples A and B

According to Figure 3.35, despite the near dense surface of sample B (Figure 3.34 (f)), micro porosity is present within internal regions of the sample. For this reason, μ CT porosity analysis was performed to quantify the percentage content of inner voids. The analysis resulted in 6.35 vol% of internal porosity caused by the manufacturing process.

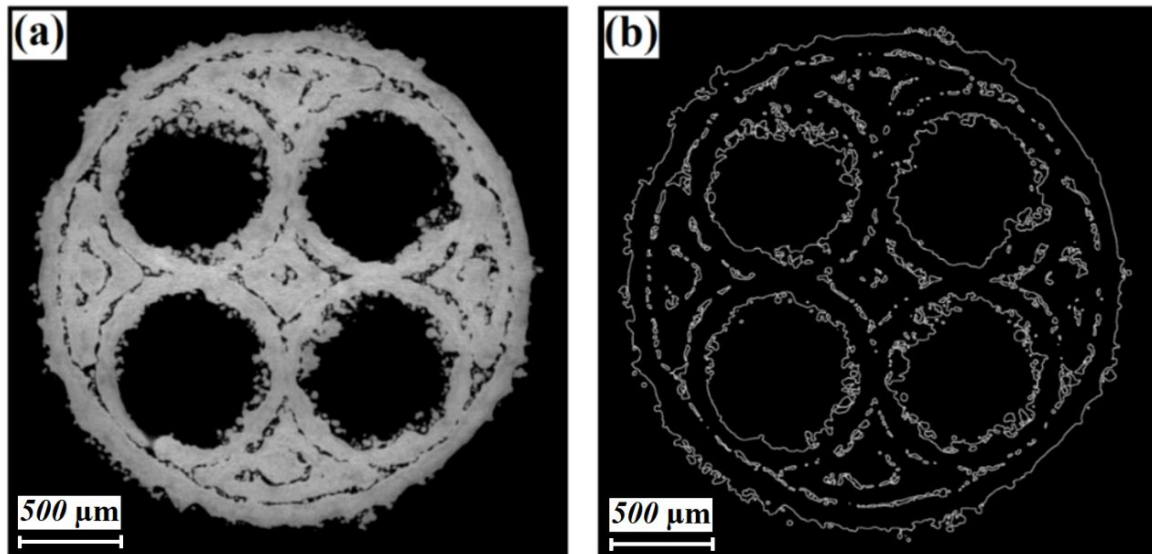


Figure 3.35– (a) Cross section of sample B obtained by μ CT and (b) determined surface (white contour). Controllable micro porosity distribution between single tracks can be observed

The dimensional accuracy of the produced NiTi part was at first investigated through the distribution of deviations between sample B (as measured by μ CT) and corresponding CAD model shown as false-colour coded map in Figure 3.36. As seen in Figure 3.36 and confirmed by the diagram in Figure 3.37 (a), the measured deviations between the as-produced and nominal part are mainly negative. This means that the internal cylindrical holes of sample B are larger than nominal values. This type of deviations analysis includes also the contribution of possible positional errors of the cylindrical inner holes. Actual positional errors, which are illustrated in Figure 3.37 (b) were calculated by generation of least-squares cylindrical elements on each inner hole and were determined to be 0.024 mm on average. For this reason, each feature was individually evaluated and a mean diameter error of 10 % (positive) was measured with standard deviation of 1.1 %. Moreover, the mean form error is 0.22 mm.

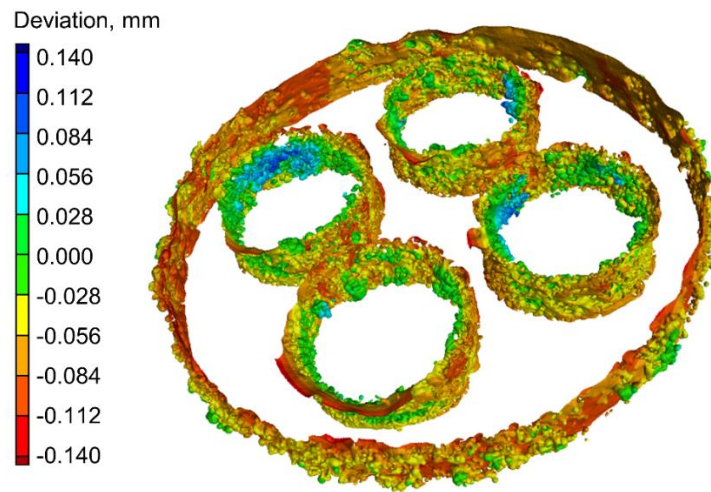


Figure 3.36– Distribution of the deviations of sample B (measured by μ CT) with respect to the CAD model shown as colour-coded map of deviations

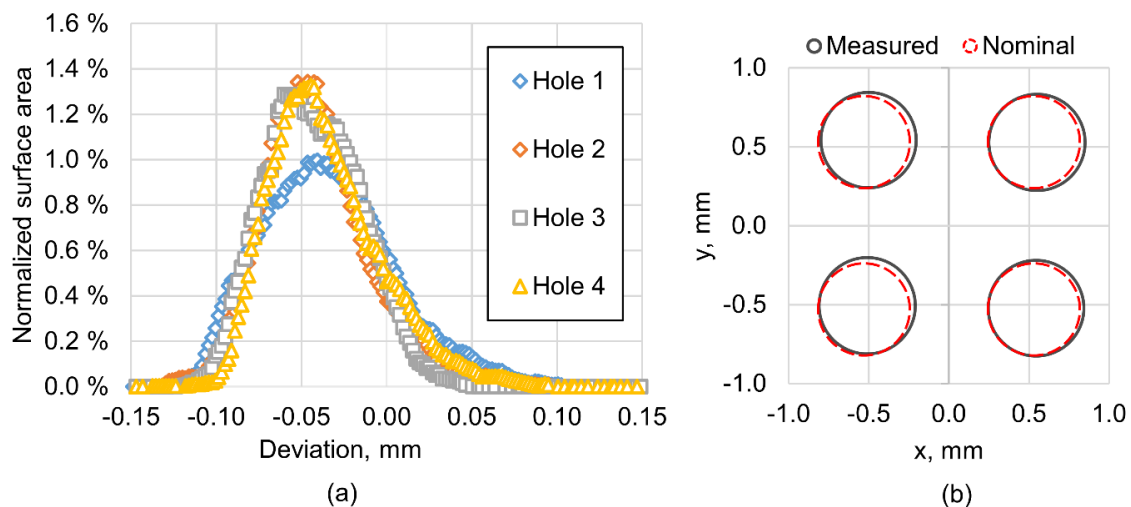


Figure 3.37 (a) Diagram showing the amount of surface area of sample B interested by each specific deviation value. Each set of points (shown in different colours) corresponds to a specific hole; (b) least-squares diameters and position of the internal holes compared to nominal diameters and position

In the case of using high laser power and consequently rough surface finish, the input energy needs to be reduced. It is well understood that an increase in scanning speed improves the surface roughness [70]. For instance, production of NiTi thin walls and simple cubes was done in this research and results showed that an increase in scanning speed results in decrease of

surface roughness. Additionally, it has been understood that high scanning speed is a useful strategy to produce high quality thin walls and enables the production of fine features using additive manufacturing.

Sample C with smaller predefined cylindrical inner holes (i.e. 500 μm diameter) was designed and produced according to design nr2 presented in Figure 2.11. Process parameters are the same for both samples B and C, except of laser scanning speed, which is 120 mm/min for sample B and 150 mm/min for sample C. Scanning electron micrographs of sample C are shown in Figure 3.38; they illustrate the quality of obtained surfaces (Figure 3.38 (a)), of predefined holes (Figure 3.38 (b)) and inter tracks regions (Figure 3.38 (c)). In particular, the comparison of sample C in Figure 3.38 to sample B in Figure 3.34, shows that an increase in scanning speed from 120 mm/min (sample B) to 150 mm/min (sample C) results in improved surface quality when the power of laser is constant (25 W). The surface quality of the investigated samples was further evaluated inside the holes by CT, which has recently started to be used for surface evaluations of AM parts as it is capable of obtaining topographical information at micro-scale, including non-accessible surfaces and undercuts [83]. After removing the form by cylindrical least-squares fitting, S_a and S_z parameters were evaluated on the surface S-F according to the standard [84] and reported in

Table 3.9, confirming that a slight improvement of surface quality can be achieved with increased scanning speed in sample containing smaller holes (sample C) in comparison to sample B. Surface roughness is relevant especially when dealing with micro features production.

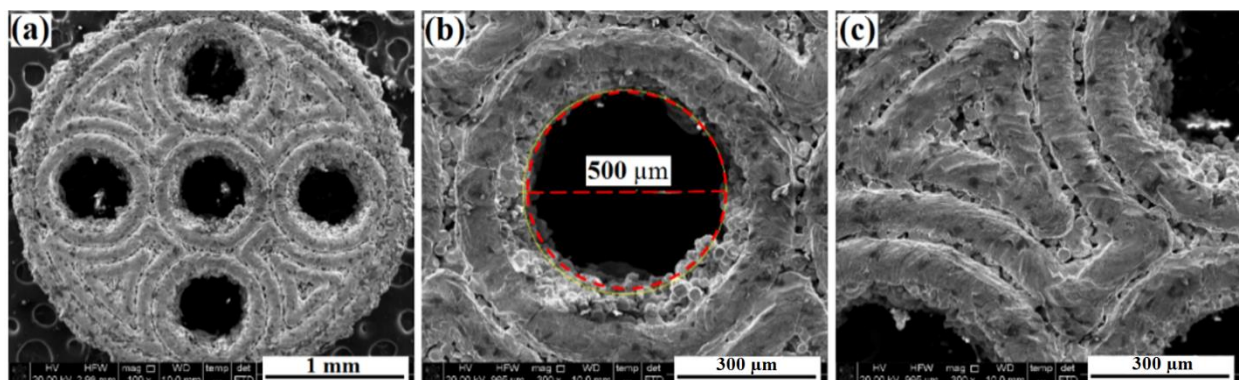


Figure 3.38– Scanning electron micrographs of NiTi sample C

Table 3.9– Sa and Sz parameters evaluated by μ CT on the inner hole's surfaces

Sample	Mean Sa, μm	Mean Sz, μm
B	15.73	176.25
C	14.32	142.07

As stated before, 30% deviation to predefined diameter (750 μm) of holes has been reported in Ti hollow samples produced by SLM (Figure 3.39 (b)) [23]. Lower deviations to predefined hole diameter (500 μm) in NiTi porous sample C can be observed through SEM micrograph in Figure 3.39 (a). Comparing Figure 3.39 (a) and (b), the micro holes produced by μ DMD show more regular internal surfaces than those larger holes produced by SLM. The dimensional accuracy of sample C was further evaluated by μ CT. Distribution of deviations of sample C (as measured by μ CT) with respect to the CAD model are presented in Figure 3.40 using false-colour coded map. Also for sample C, the measured deviations are mainly negative, as confirmed by the diagram in Figure 3.41 (a). In this case, the average positional error of internal features (Figure 3.41 (b)) is similar with respect to Sample B (i.e. 0.025 mm). Furthermore, the mean diameter error evaluated through least-squares fitting of cylindrical elements on the inner holes was found to be 13% (positive) with 1.6% of standard deviation. The mean form error is equal to 0.16 mm.

It can be concluded that the development of μ DMD process enables higher geometrical accuracy for the production of micro features in comparison with the existing literature on SLM process [23]. This result can be attributed to the difference in powder feeding method of the two processes. In SLM, the powder bed method is used, in which the edge of a predefined hole is formed by laser melting when the central region of hole is filled by unmelted powder particles that will be removed at the end of process. Therefore, during the SLM process, a portion of laser input energy is transferred to those powder particles that are not planned to melt according to nominal geometrical models. This transferred energy leads to partial or full

melting of excess powder particles and, consequently, results in augmented geometrical deviations with respect to nominal geometrical predesigned model.

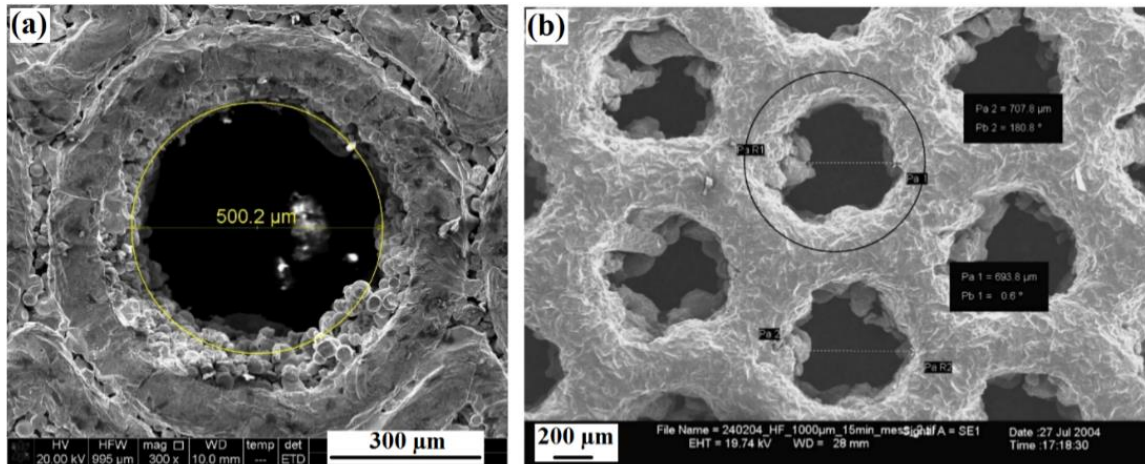


Figure 3.39– Scanning electron micrographs of (a) NiTi sample with 500 μm hole diameter produced by μDMD in this research, (b) Ti hollow sample with 750 μm hole diameter produced via SLM by Hollander et al. [23]

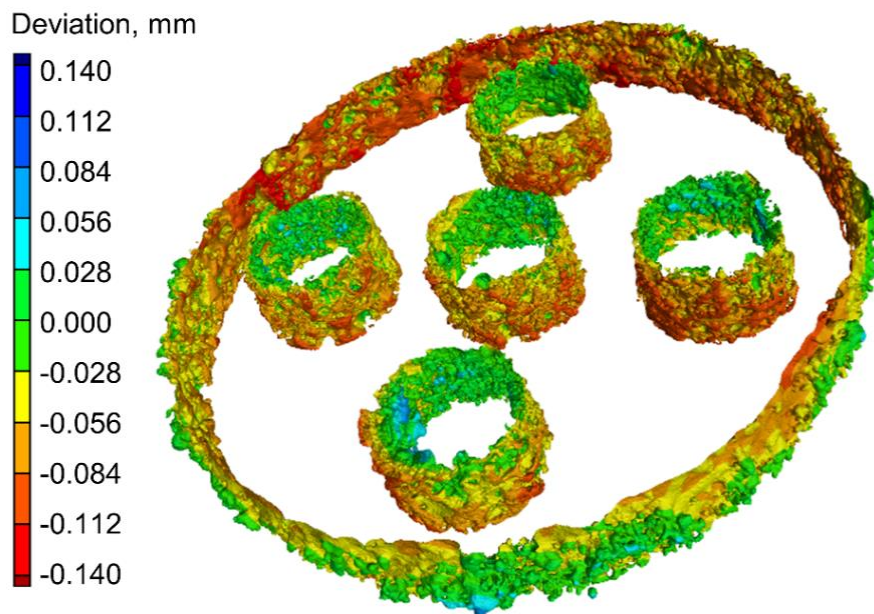


Figure 3.40– Distribution of the deviations of sample C (measured by μCT) with respect to the CAD model shown as colour-coded map of deviations

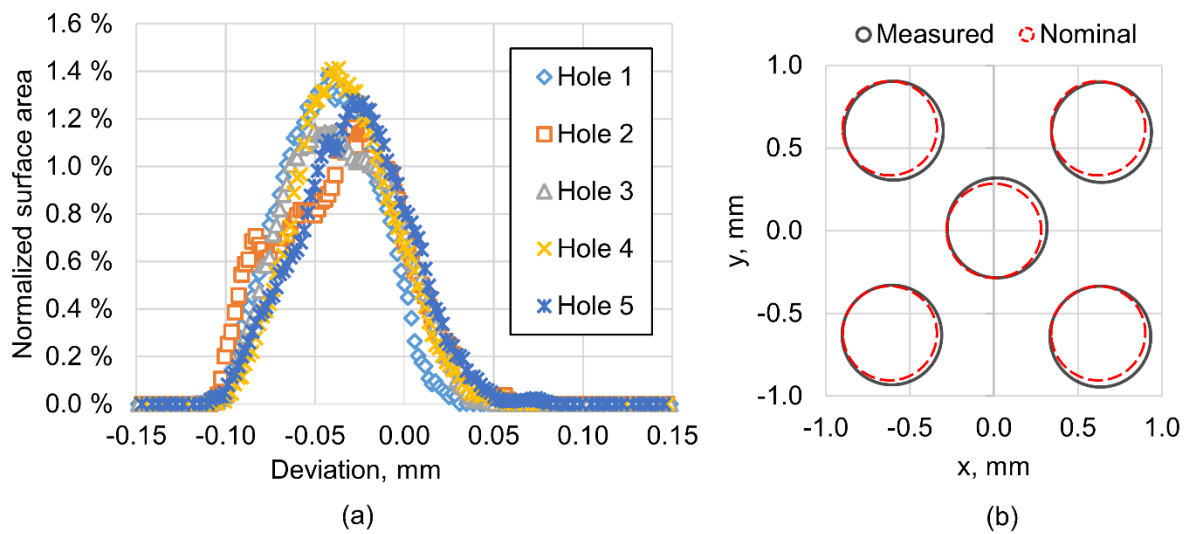


Figure 3.41– (a) diagram showing the amount of surface area of sample C interested by each specific deviation value. Each curve corresponds to a specific hole; (b) least-squares diameters and position of the internal holes compared to nominal diameters and position

Figure 3.42 (a) and (b) compare the controllable micro porosity between tracks contained in samples B and C respectively. CT porosity analysis resulted in about 4.28 vol% of micro pores in sample C. As stated before, micro porosity in sample B was measured as 6.35 vol%. It can be concluded that, by keeping constant the laser power and simultaneously increasing the scanning speed, lower micro porosity contents are achievable. As it can be seen in Figure 3.42, when the laser power is constant, high scanning speed rises the homogeneity of micro pore's distribution between the tracks.

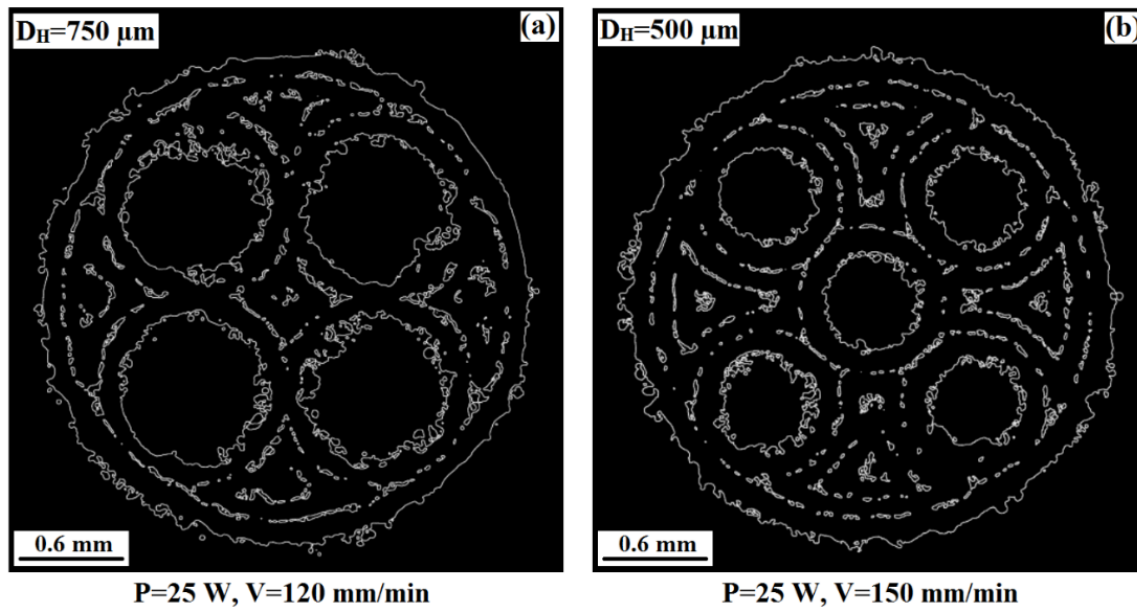


Figure 3.42– Porosity distribution between tracks in NiTi samples (a) B and (b) C produced by μ DMD

In conclusion, by increasing the scanning speed it is possible to produce parts with lower porosity content and with smaller features characterized by better surface quality, improved form errors and almost unchanged dimensional accuracy. However, it should be mentioned that increase in scanning speed decreases the growth rate in build direction and inhibits 3D manufacturing. Thus, optimum process parameters must be extracted for each material and design.

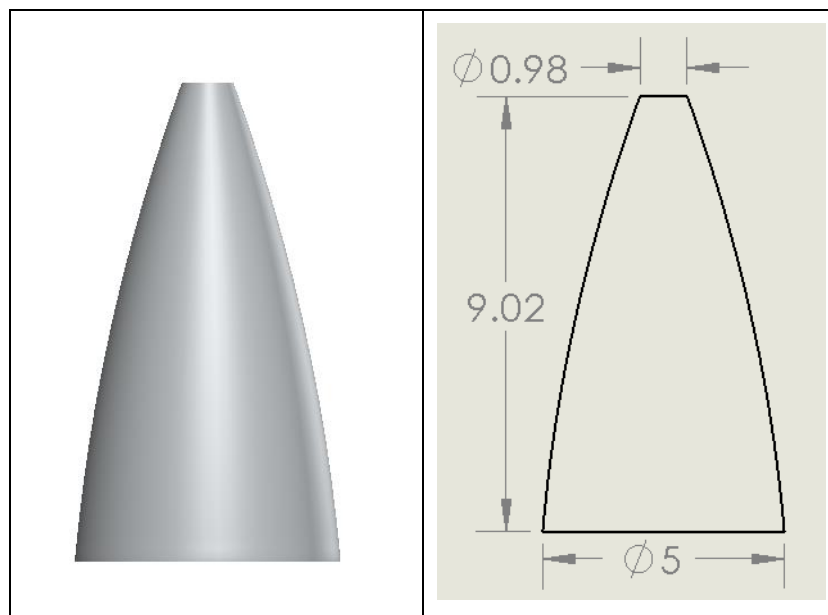
3.6 Production of multi section samples using μ DMD

TiAl is similar to NiTi in sense of difficulties in subtractive machining. Adding Niobium can overcome this limitation but is still interesting for AM processes. Accumulation of heat energy and lack of appropriate heat dissipation could increase the temperature of working plane during the direct metal deposition of successive layers. If an object at one temperature is exposed to a medium of another temperature, the temperature difference between the object and the medium follows exponential decay (in the limit of slow processes; equivalent to good heat conduction inside the object, so that its temperature remains relatively uniform through its volume).

Table 3.10– μ DMD process parameters in z direction according to heat decay model ($\lambda=1$)

N of layer	P (W)	V (mm/sec)	t (μ m)	dh (μ m)	E (KJ/mm ³)
1	70	2.20	7	200	22
2	50	2.30	15	200	7.246
3	40	2.50	18	200	4.444
4	35	2.60	20	200	3.365
5	32	2.70	21	200	2.821
6	27	3	24	200	1.875

A simple cone with 5mm of basal, 9mm of height and 0.12 mm of wall thickness was designed. The maximum overhang of 20° was considered for the inclined surfaces.

Figure 3.44– CAD model of simple cone with maximum overhang of 20°

The CAD model was imported in CALD software and 6 different set process parameters (presented in Table 3.10) were assigned to six layers to cover the 9 mm of cone's height.

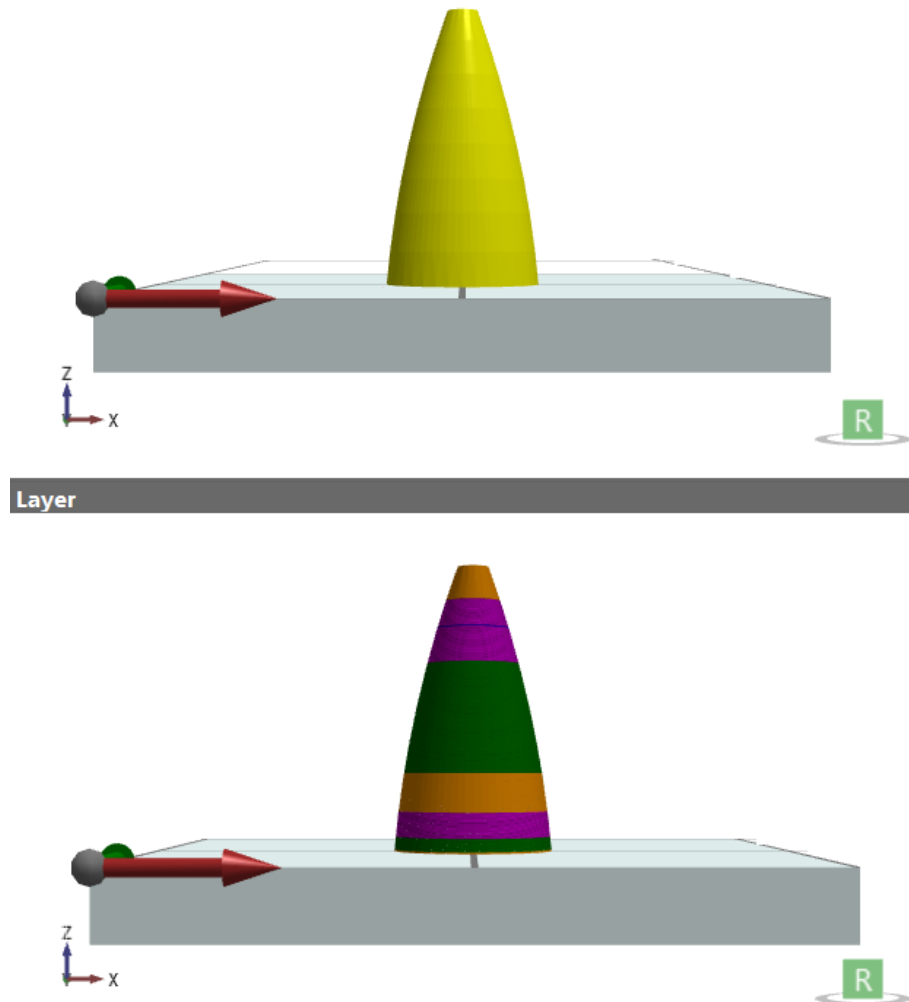


Figure 3.45– Process parameters assignment for fabrication of Ti-Al-Nb cone using μ DMD and heat decay model: Layer 1: 50 μm , Layer 2: 200 μm , Layer 3: 500 μm , Layer 4: 1000 μm , Layer 5: 5500 μm , Layer 6: 1750 μm

Ti-Al-Nb cone was successfully implemented using micro direct metal deposition and process parameters mentioned in Table 3.10. Screw speed, gas flow rate and brush speed were set at 10 $\mu\text{m}/\text{sec}$, 0.5 L/min and 750 rpm respectively. The μ DMD cone is shown in Figure 3.46.



Figure 3.46– Ti-Al-Nb cone produced by μ DMD using heat decay model (in collaboration with Manudirect company)

3.7 Summary and conclusion (μ DMD of NiTi)

Synthesis of NiTi single phase from the elemental powder mixtures using high energy mechanical alloying and μ DMD process was done in this research. The high energy mechanical alloying can produce a sustainable NiTi microstructure with high tendency to form NiTi single phase after μ DMD process. Both the energy accumulated inside the particles during the milling process and the energy input during the laser deposition contribute the melt pool formation; By using high energy milled $\text{Ni}_{50.8}\text{Ti}_{49.2}$ powder, the scanning speed in the μ DMD process can be increased up to 3 times without any change of the phase composition.

Results showed that, raise in substrate's temperature generally facilitates the formation of 3D parts by μ DMD. However, because of high level of input energy in μ DMD process, there is an optimum temperature to achieve 3D part with minimum inherent micro porosity. This temperature is 300 °C for NiTi. Using different scanning strategies in μ DMD process revealed that, when there is a 90-degree rotation between the scanning directions in subsequent layers, the distribution of controllable micro pores is more homogeneous and the pores are smaller and more rounded in comparison with the other strategies. Adjusting the strategy of scanning makes it possible to tailor the controllable micro pore's characteristics and consequently mechanical

properties of μ DMD processed parts. It was found that, the angle between neighbouring laser scanning paths in RD-TD plane (θ_T) has not significant effect on microstructure of μ DMD processed builds and the angle between neighbouring single tracks in successive layers (θ_L) may control the surface microstructure.

The average grain size of NiTi parts produced by μ DMD process is below 10 μm which is smaller than previously obtained grain sizes in conventional DMD process of NiTi by other researchers. It can be attributed to smaller melt pool and consequently sever rapid solidification in μ DMD process with respect to conventional DMD process. A strong $\langle 100 \rangle \parallel \text{RD}$ texture of 11.5x random was characterized for μ DMD processed NiTi sample by bidirectional neighbouring single tracks in consequent layers. Moreover, a discontinuous β fiber texture exists in μ DMD processed NiTi samples produced by unidirectional neighbouring single tracks in consequent layers.

In this thesis, micro direct metal deposition (μ DMD) process was developed for fabrication of NiTi hollow materials with micro features. Investigation revealed that increasing the scanning speed is an effective and efficient way to enhance the surface quality of parts produced by μ DMD. However, it should be noted that increasing the scanning speed inhibits the growth rate in the building direction. Dimensional accuracy of micro features in μ DMD processed parts with respect to nominal geometrical model was qualitatively evaluated using SEM and quantitatively by μ CT. Investigations based on SEM micrographs and CT data revealed lower deviation to nominal geometrical model in μ DMD processed parts than for SLM process (as reported from literature). In particular, the obtained deviations values for design nr. 1 (containing holes with 750 μm nominal diameter) and design nr. 2 (containing hole with 500 μm nominal diameter) from CT analysis were 10 % and 13 % respectively. Moreover, the CT measured deviations between the as-produced and nominal part were found to be mainly negative. This means that the internal cylindrical micro holes of both designs are larger than nominal values.

A slight improvement of surface roughness ($\Delta S_a = 9\%$ and $\Delta S_z = 19\%$) can be achieved with increased scanning speed in the sample containing smaller predefined holes (sample C, $dh = 500\ \mu\text{m}$) in comparison to the one with larger holes (sample B, $dh = 750\ \mu\text{m}$). Micro porosity

analysis using CT technique resulted in about 4.28 vol% and 6.35 vol% of micro pores in sample C and B respectively. Therefore, lower micro porosity contents are achievable in μ DMD processed parts by keeping constant the laser power and simultaneously increasing the scanning speed. It can be concluded that, by using micro direct metal deposition process and specific set of process parameters, feature sizes can be reduced without losing the accuracy, as well as surface finish and density can be improved. It should be mentioned that definition of different layers in term of input energy densities is a crucial factor for production of multi sectional 3D samples.

Chapter 4 Results and discussion: SLM of NiTi and production of lattice structures

In the first section of this chapter, the effect of SLM process parameters on phase composition, porosity and surface topography of NiTi parts has been studied using different techniques, such as X-ray diffraction, scanning electron microscope and micro X-ray computed tomography. Three different regimes of process parameters for obtaining the single phase B2-NiTi by SLM technique have been proposed. In the second part of this chapter, production of self-supported lattice structures and related issues have been addressed through SS316L and Ti6Al4V alloys. Design and manufacture of NiTi porous scaffolds (lattice structures) based on the computed tomography of human bone is the final section of this chapter.

4.1 Production of dense NiTi using SLM

Figure 4.1 (a) and (b) show two main designs that were utilized to build SLM NiTi parts. Geometries have been designed based on the characterization tests sample requirements. To fix the part on the platform and to enhance heat conduction during SLM processing, 3 mm block support structures are developed and added to the sliced CAD model (Figure 4.1 (a) and (b)). Chessboard meander hatch were utilized as scanning strategy and presented in Figure 4.1 (c). This method leads to homogenous distribution of residual stresses after SLM process [85]. Same process parameters were applied for fabrication of internal and external parts of the samples to eliminate the effect of input energy on phase composition of samples.

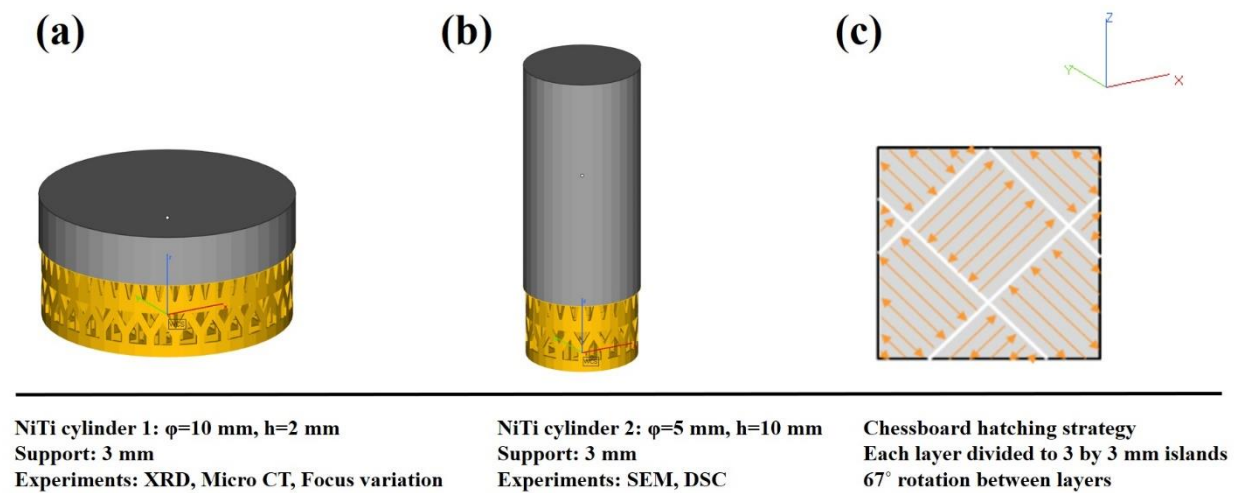


Figure 4.1– (a, b) two CAD designs used in this study for NiTi samples, (c) an overview of the chessboard hatching strategy used in this study

As mentioned in section 2.2.1, the Ni_{50.8}Ti_{49.2} (at%) pre-alloyed spherical powder was used as an initial powder for SLM process. Equiatomic NiTi has low strength and poor cyclic stability. However, Ni content can increase the strength of material. It should be mentioned that in Ni-rich NiTi, TTs are very sensitive to the Ni content of the matrix where they decrease by about 93 °C / at%. This phenomenon limits the production. Input energy density in SLM process has a direct influence on Ni evaporation and consequently component's Ni content.

Selective laser melting process parameters including layer thickness (t), hatch distance (dh), laser spot diameter (dl), laser power (P), scanning speed (V) and scanning strategy are used to manipulate input energy density (E). Calculation of input energy density in selective laser melting process is possible through the main process parameters as presented in equation:

$$E = \frac{P}{V \cdot dh \cdot t} \quad (4.1)$$

There are few research teams working on SLM of Nitinol. Based on the literature, the input energy densities in the range of 50 to 120 j/mm³ have been used for SLM of Nitinol as presented on Table 4.1. An overview of all scanning parameters used for SLM in this study is given in Table 4.2.

Table 4.1- SLM process parameters used for production of dense NiTi in the literature

		P (W)	V (mm/sec)	t (μm)	dh (μm)	E (J/mm^3)	dl (μm)
KU Leuven, Belgium [86]	HP	250	1100	30	60	126	80
	LP	40	160	30	75	111	80
University of Toledo, US [42]		250	1250	30	120	55	80

Table 4.2- Overview of scanning parameters used for SLM of NiTi

Parameter	Values
Power (P)	70, 94, 120, 150 watt
Scanning speed (V)	700, 1000, 1100 mm/sec
Hatch distance (dH)	60, 100 μm
Layer thickness (t)	20 or 25 μm
Energy densities (E)	50-120 j/mm^3
Laser spot diameter (dL)	30 μm
Oxygen level	<200 ppm

The layer thickness should be selected based on the powder particles dimension. In this research, NiTi powder of 15-45 μm was used, therefore, the layer thickness was selected around median of powder size (20- 25 μm). In this thesis, SLM is experimented to manufacture NiTi parts with micro features. Aiming to micro manufacturing, laser spot diameter of 30 μm was used. To the best of our knowledge, it is the minimum laser spot diameter that has been used up to now for the fabrication of NiTi through SLM. Therefore, new regimes of process parameters should be defined. Combinations of all process parameters presented in Table 4.2 have been utilized for fabrication except those are out of the range of appropriate input energy

densities (50 to 120 j/mm³). All 20 possibly acceptable sets of process parameters are listed in Table 4.3.

Table 4.3- Overview of proposal regimes of process parameters for SLM of NiTi

Cube number	Power of laser (W)	Scanning speed (mm)	dh (mm)
C1	70	700	0.1
C2	100	1000	0.1
C3	70	1100	0.06
C4	120	1100	0.1
C5	70	1000	0.06
C6	120	1000	0.1
C7	94	700	0.1
C8	150	1100	0.1
C9	94	1100	0.06
C10	100	700	0.1
C11	150	1000	0.1
C12	94	1000	0.06
C13	70	700	0.06
C14	120	700	0.1
C15	120	1100	0.06
C16	120	1000	0.06
C17	150	700	0.1
C18	94	700	0.06
C19	150	1100	0.06
C20	150	1000	0.06

4.1.1 The effect of process parameters on phase transformation in SLM NiTi

DSC analysis showed that increase in input energy density leads to increase in phase transformation temperatures (TTs) (Figure 4.2). High input energy density, which in this case comes from the low scanning speed, raises the melt pool temperature. Since Nickel has lower melting temperatures than Titanium, the matrix composition shifts to higher titanium content after SLM process due to evaporation of Nickel. For initial NiTi powder and SLMed parts, double transformation peaks were observed during heating and cooling where the first peak can be attributed to austenite to R-phase transformation and the second peak can be attributed to R-phase to martensite transformation. As can be seen in Figure 4.2, increasing in input energy densities increases the temperatures of Martensite to Austenite phase transformation because of Ni depletion. Similar findings have been reported by other researchers [87].

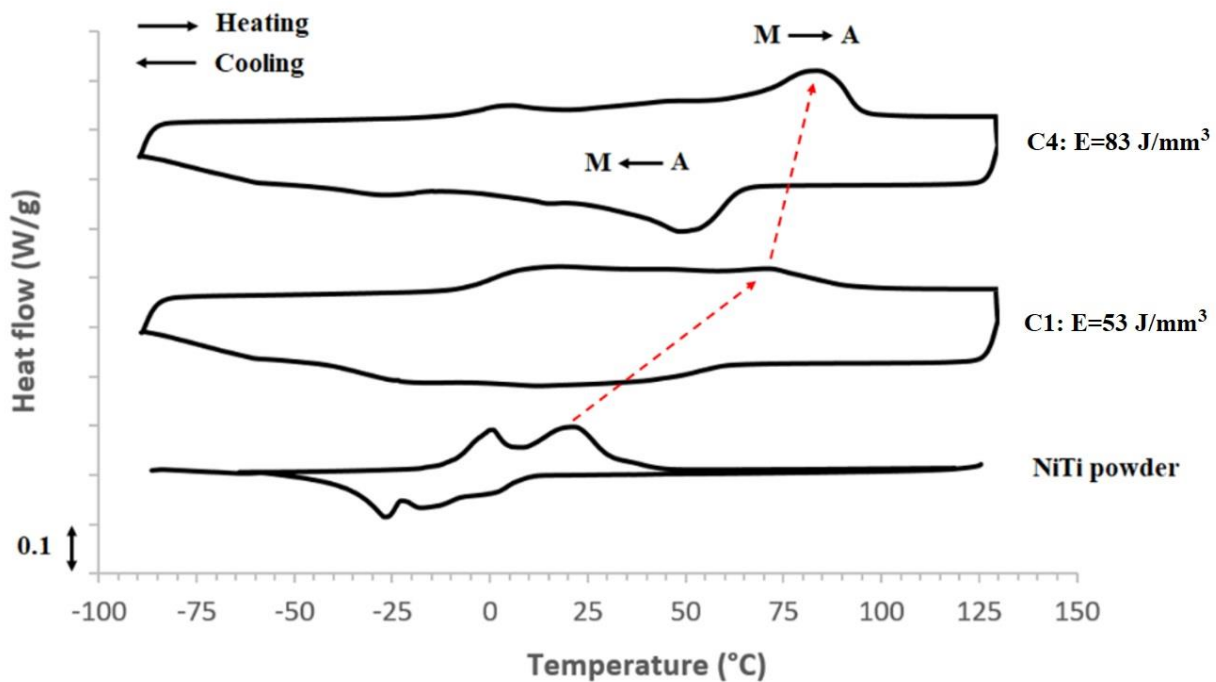


Figure 4.2– DSC curves of SLM NiTi samples produced by two different input energy densities according to Table 3

When the Ni content in NiTi alloy is over 50.5 at%, martensitic transformation temperatures increase with decreasing Ni content. In fact, in Ni-rich nitinol, the Ni content would be the most determinant factor for phase transformation behavior [86]. Dadbakhsh et al. [47] reported different results in Ti-rich Nitinol (55.5 at% Ti) and they connected this finding to other factors such as reduced precipitation due to higher cooling rate at high laser power adjusted to high scanning speed. Moreover, in Ni-rich alloys, precipitates like Ni_4Ti_3 and Ni_3Ti increase the TTs because they facilitate Martensite formation with inducing incoherency stresses [88]. Formation of secondary phases in NiTi system is unavoidable because their formation is much more favorable thermodynamically compared to the formation of NiTi. Precipitates bigger than a threshold may act as a nucleation site for martensitic transformation and facilitate martensite formation. Higher cooling rates coming from higher scanning speed may reduce the grain sizes to a threshold that may decrease TTs. This threshold grain size is reported under 100 nm [89]. However, Ni rich alloys higher speeds leads to Ni depletion and consequently decrease TTs and in such alloys Ni content is predominant factor in comparison to other factors like precipitations and grain sizes [86]. Considering small diameter of laser spot (30 μm) and small melt pool in our research in comparison to previous research works, cooling rate is more severe and leads to finer grain structures due to rapid solidification. Solution treatment has been suggested to dissolve precipitates and increase the grain size and restore the TTs [86]. Based on the energy density, the fabricated parts by SLM are classified into low, medium and high parameters (laser power and scanning speed). Each class greatly influences the transformation temperatures (TTs), the thermomechanical behavior and the microstructure of NiTi parts. Additionally, for fabrication of complicated geometry containing micro features such as micro pores, it is necessary to use different regimes of process parameters for border and internal parts of an object in SLM process. Based on previous experiments and aiming to have fully austenite microstructure at room temperature, three regimes of process parameters have been proposed and tested (Table 4.4).

Table 4.4– Selected SLM process parameters regimes to obtain single phase NiTi

Process parameters	Power of laser (W)	Scanning speed (mm)	dh (mm)	t (mm)	E (j/mm ³)
LP	49	700	0.06	0.025	46.66
				0.020	58.33
MP	70	1100	0.06	0.025	42.42
				0.020	53.03
HP	150	1100	0.1	0.025	54.54
				0.020	68.18

Since change in laser power and scanning speed are restricted by feasibility, one way to assess the effect of input energy density is the change in layer thickness in SLM process (Table 4.4). As can be seen in Figure 4.3, decrease in layer thickness and consequently increase in input energy density leads to formation of martensite phase (Figure 4.3 (a)). It shows that selection of right process parameters is crucial in obtaining single phase Austenite during the SLM process.

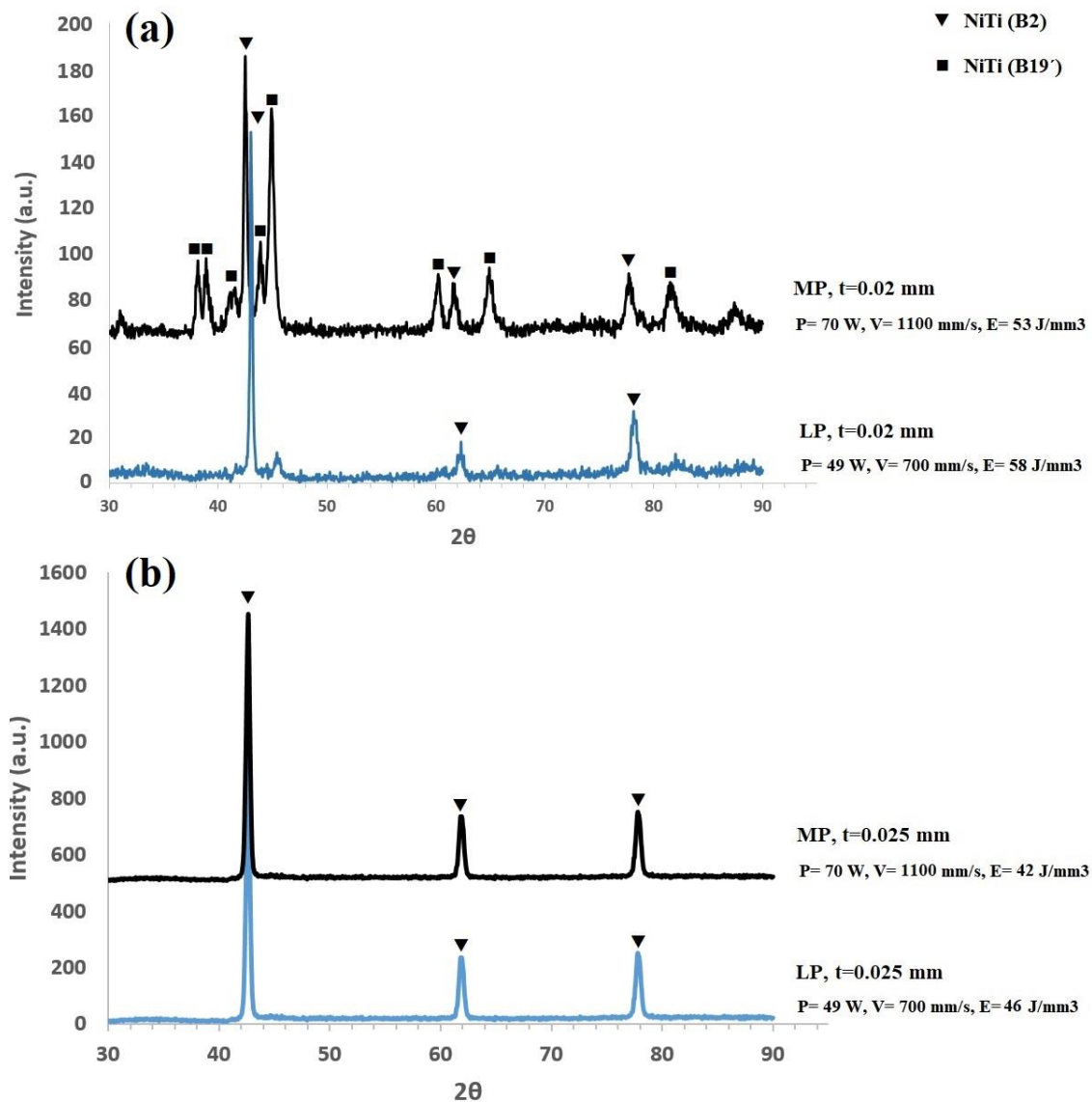


Figure 4.3– XRD patterns of SLM NiTi samples produced by LP and MP parameters (Table 4.4) and two different layer thicknesses (a) 0.02 mm and (b) 0.025 mm

Increase in layer thickness reduces input energy density and consequently decreases the melt pool temperature. Low temperature of melt pool makes temperature gradient (dT/dx) less extreme and cause to the coarse grain microstructure. This phenomenon has been shown in Figure 4.4. XRD pattern of NiTi sample produced by layer thickness of 0.025 mm showed sharper and higher peaks in comparison to NiTi samples produced by layer thickness of 0.020 mm. It is well understood that peak's broadening and height lowering is due to grain fining and

accumulated internal micro strain in crystalline structures. Moreover, low layer thickness in SLM causes to remelting of previous solidified layers which is a conventional method for grain refining.

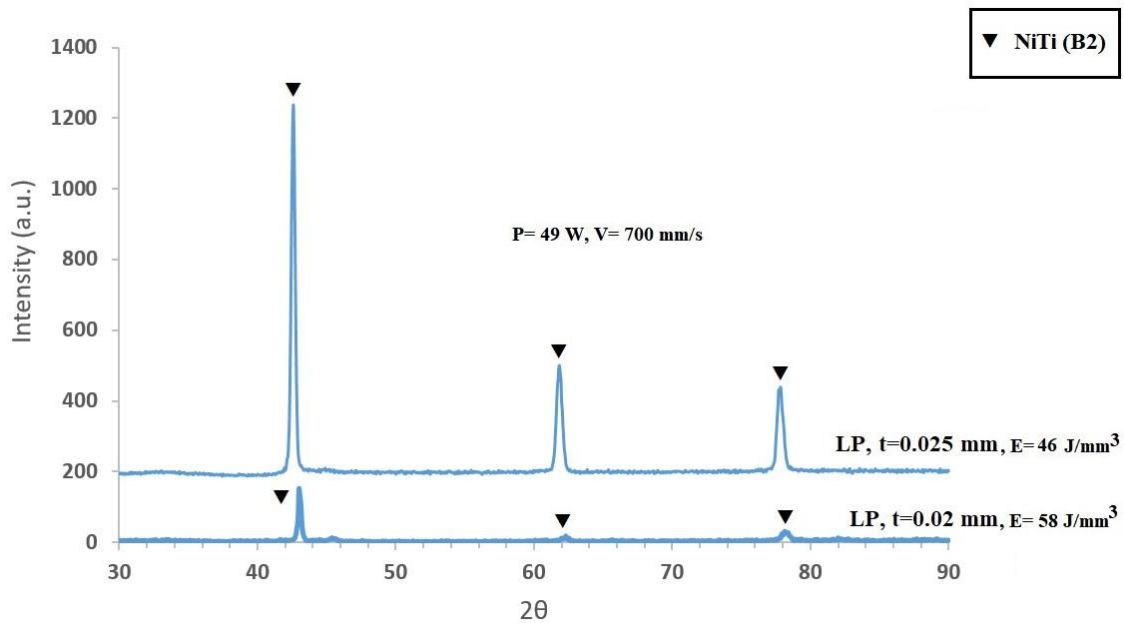


Figure 4.4– XRD patterns of SLM NiTi samples produced by LP parameters (Table 4.4) and two different layer thicknesses (0.02 and 0.025 mm)

As stated before, for production of complicated geometries with micro features, the parameters of internal and external parts should be different and at the same time the outcome phase of all regimes of process parameters should be the same. X-ray diffraction analysis confirmed that the three different regimes of process parameters (LP, MP, HP) proposed in this research are capable to reach a single phase NiTi B2-Austenite phase after SLM of Ni_{50.8}Ti_{49.2} alloy (Figure 4.5).

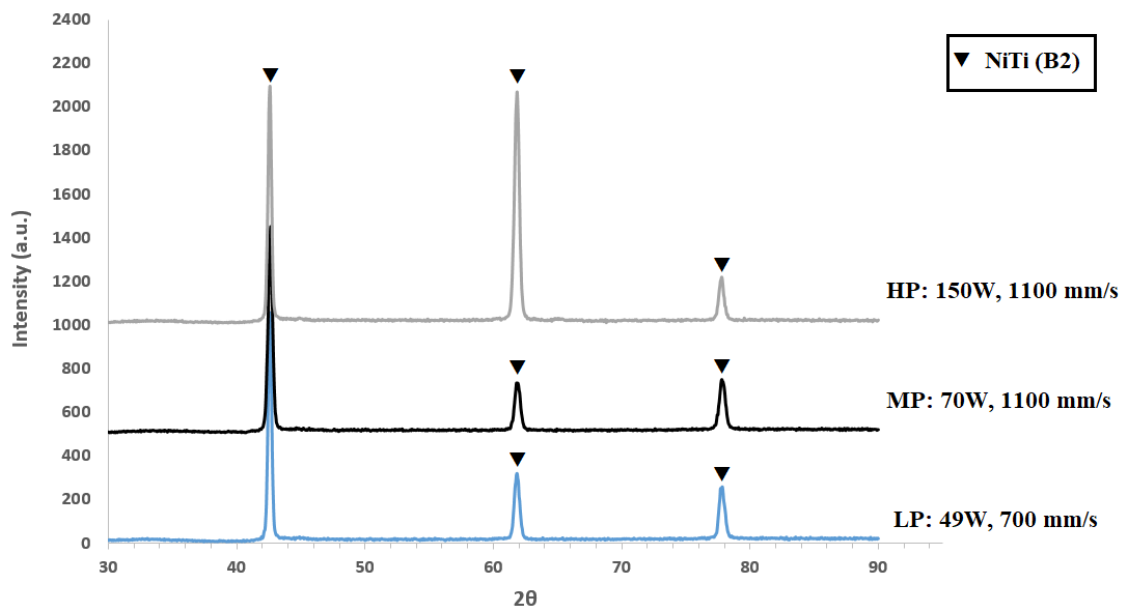


Figure 4.5– XRD patterns of SLM NiTi samples produced by LP and MP parameters (Table 4.4) and two different layer thicknesses (a) 0.02 mm and (b) 0.025 mm

4.1.2 The effect of platform's material on quality of products

Material selection for platform in SLM process is an important issue. Using stainless steel platform provide more cooling rate and increase the thermal gradient (dT/dx). High thermal gradient facilitates martensitic transformation which is brittle compare to austenite phase. Moreover, linear thermal expansion coefficient of steel is significantly different to Nitinol (Table 4.8). Therefore, production of Nitinol parts on steel platforms is limited. Unlike to stainless steel 316, Ti6Al4V could be a good option to be used as platform for SLM of Nitinol thanks to similar thermal expansions and lower cooling rate which stabilize austenite formation in primary layers. Preliminary experiments confirmed that NiTi parts form better on Ti platforms in comparison to steel platforms.

Table 4.5– Thermal properties of Ti6Al4V, Stainless steel 316 and Nitinol

	Ti6Al4V	Stainless steel 316	Nitinol
Linear thermal expansion coefficient ($10^{-6}/^{\circ}\text{K}$)	8.7-9.1	15-18	Austenite: 11 Martensite: 6.6
Thermal conductivity coefficient (W/m.K)	7.1-7.3	13-17	10

4.1.3 Surface topography evaluation

The surface topography of the investigated samples (see Figure 4.1 (a)) was evaluated using two different techniques: (i) optical profiler and (ii) X-ray computed tomography. X-ray computed tomography has recently emerged as a viable alternative technique capable of effectively measuring AM surfaces [83], provided that a sufficiently good metrological structural resolution is achieved. Besides focus variation measurements, CT surface topography evaluations were conducted in this work because they can provide information also about complex features in the micro-scale typical of AM surfaces (e.g. undercuts, re-entrant features, non-totally melted powders attached to the surface), which cannot be measured either with optical techniques nor with contact stylus techniques [90] (see example in Figure 4.6). Moreover, high-resolution CT systems specifically developed for dimensional metrology are currently available [91], hence accurate measurement results can be obtained. Figure 4.7 (a) shows the three-dimensional model of one scanned sample, obtained after CT reconstruction. Ten surface profiles were extracted orthogonally to the weld tracks direction, as depicted in Figure 4.7 (b) and (c) shows an example of profile containing re-entrant features. The conventional surface profile parameters (as per ISO 4288) can be computed on such types of profile only if the undercuts are removed. In this work, the new definition of Pa proposed in [92] was computed on profiles extracted from CT data (primary profiles, obtained removing the form error by fitting of the mean line). This was done using a Matlab routine developed by

the University of Huddersfield [92]. Moreover, the percentage of re-entrant surface features (Prf) was also calculated, as an index of surface complexity.

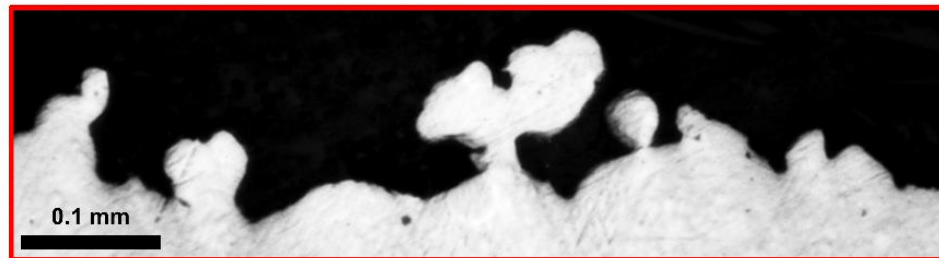


Figure 4.6– 2D profile imaged by an image probing sensor on the cut-section of an AM part. Several re-entrant features can be observed [90]

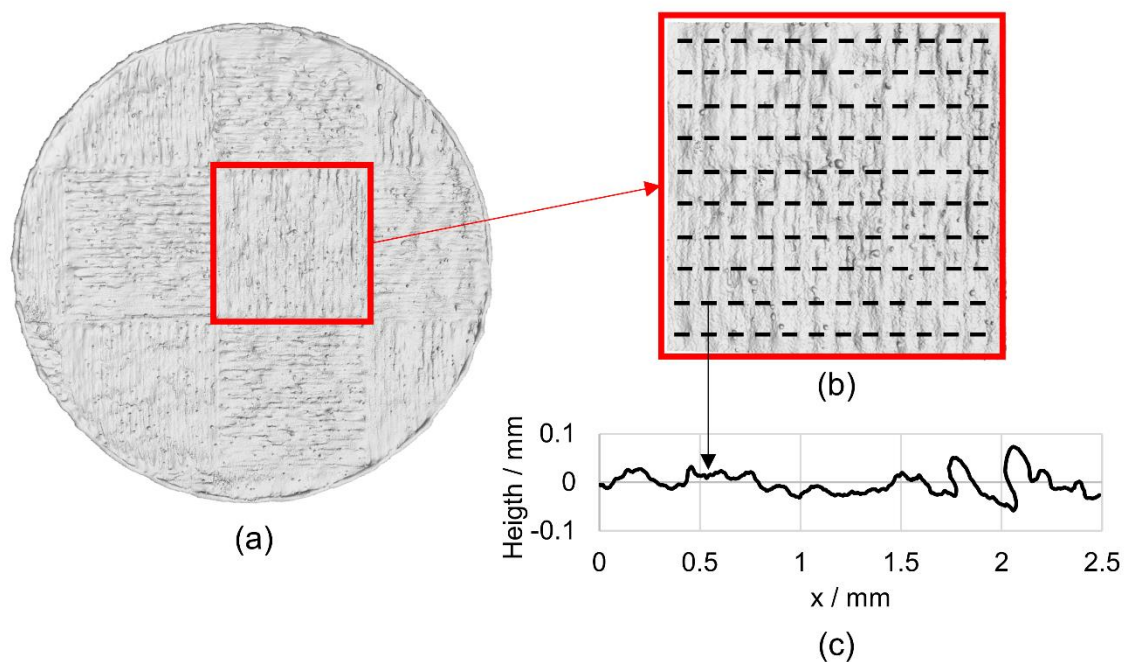


Figure 4.7– CT reconstructed model of one NiTi sample (a); surface topography extracted from the CT volume (b) and 2D profile containing re-entrant features extracted from the surface topography (c)

Surface profile measurements conducted by focus variation microscopy revealed that the laser power is the most determinant factor in surface topography of SLM NiTi samples. As can be seen in Figure 4.33, the surface quality (roughness⁻¹) has almost the same variation trend of the

laser power, while there seems to be not correlation between input energy density and surface quality.

Figure 4.10 (a-c) shows the surface topographies extracted from CT data of samples LP, MP and HP, respectively. Figure 4.10 depicts one profile out of the ten profiles extracted from the topographies of each investigated abovementioned sample. In particular, the shown profiles are the ones with the highest surface complexity (i.e. highest value of Prf) for each sample. It can be observed that the HP profile appears smoother than the others, which are instead characterized by the presence of complex re-entrant features and higher roughness. The parameter Prf , whose maximum and mean values are reported in Figure 4.11, confirm this observation: the presence of re-entrant features is less pronounced for the HP sample. Figure 4.11 compares also the average Pa values obtained using focus variation technique (applying the conventional definition of Pa) and CT (applying the definition of Pa proposed in [90]). The difference between the two measurements is very low for the HP sample (i.e. $0.8 \mu\text{m}$), while it is higher in the other two cases (both above $3.5 \mu\text{m}$). The correlation between such differences and the surface complexity (represented here by the presence of re-entrant features, Prf) can be noticed. This can be explained by the fact that, when a very small amount of undercuts is present, the surface profile parameters defined in [90] converge with the corresponding conventional parameters. This proves that it is important to consider the actual surface morphology, including the presence of undercuts which can be measured by CT. The differences in roughness between the three samples, in fact, increase when considering such surface characteristics. The obtained results let conclude that NiTi sample produced by high laser power (150 W) has the best surface quality and minimum roughness.

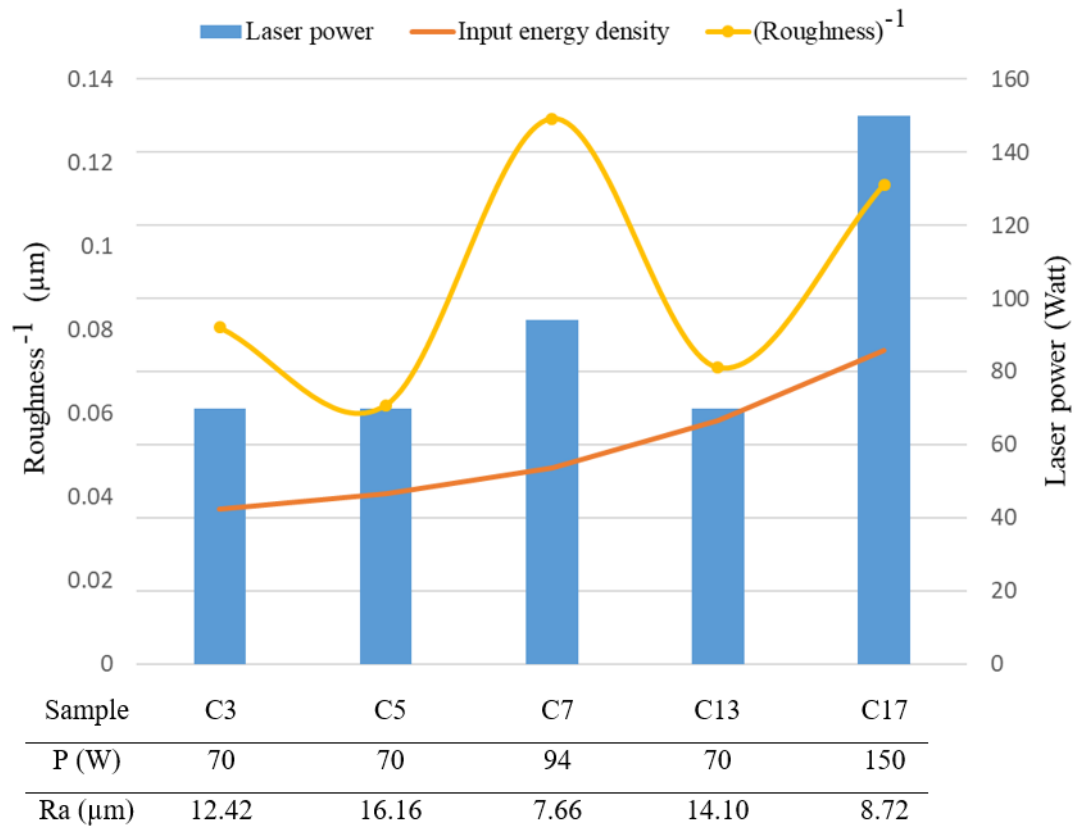


Figure 4.8– Roughness measurements of SLM NiTi (Table 4.3) using optical microscope and focus variation methods

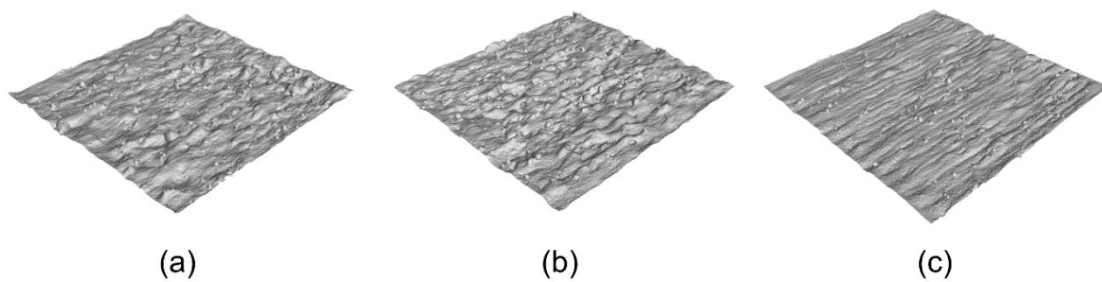


Figure 4.9– Surface topographies extracted from CT data of samples LP (a), MP (b) and HP (c).

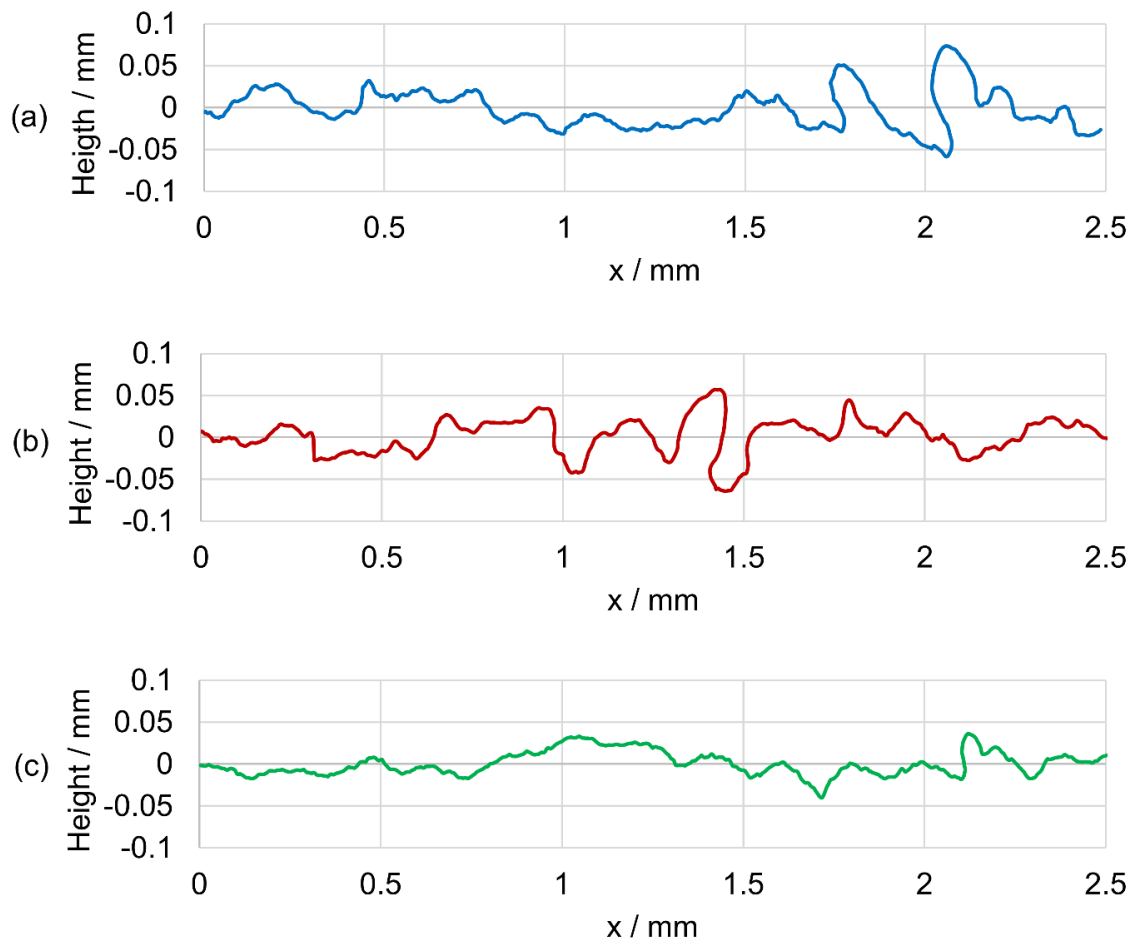


Figure 4.10– Example of surface profiles extracted from CT data of samples LP (a), MP (b) and HP (c)

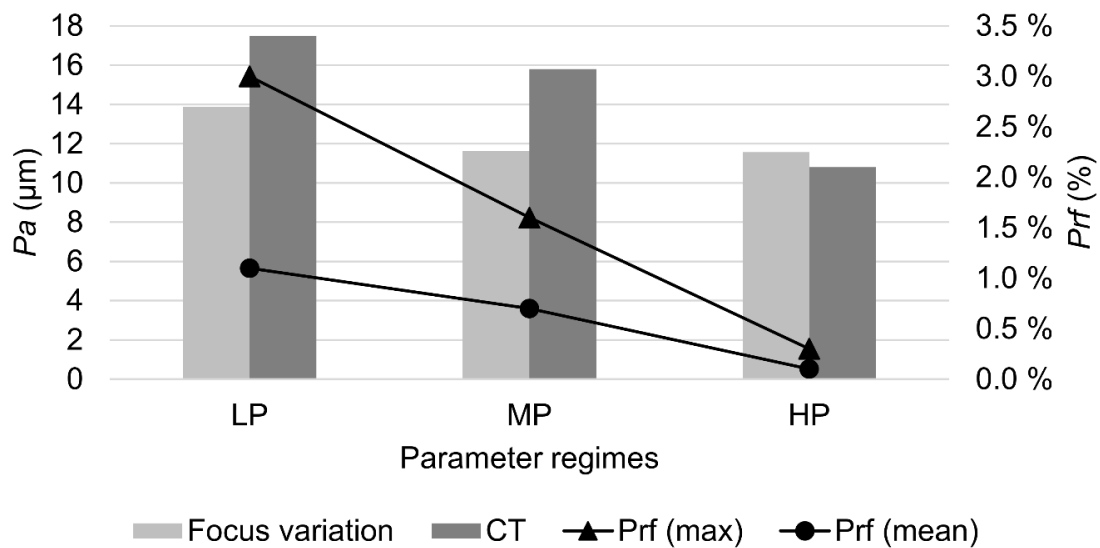


Figure 4.11– Comparison of P_a values measured using focus variation microscope and X-ray CT. Maximum and mean Prf values are also reported as index of surface complexity

4.1.4 Porosity analysis in SLM NiTi alloy

Porosity evaluations were firstly conducted on samples whose design is illustrated in Figure 4.1(b) using scanning electron microscope (SEM) and image analysis method. Such analyses were meant to define a process parameter window to obtain the maximum density and minimum porosity. In addition, CT scans performed on samples shown in Figure 4.1 (a) were used for advanced internal defect inspection as well. CT technique allows measuring the internal porosity in a non-destructive way. Moreover, it is the only available tool capable of providing a complete set of information about the pores' characteristics including size, spatial distribution and morphology. The "Defect detection" module of the analysis-and visualization software VGStudio MAX 3.1 (Volume Graphics GmbH, Germany) was used for this purpose. Porosity measurements using scanning electron microscope and image analysis method depicts that to obtain the maximum density and minimum porosity a precise process parameters window should be defined which is an optimum equilibrium between laser power, scanning speed and hatch distances. From Figure 4.12 it can be concluded that, samples produced by low scanning speeds have high level of porosity. It can be attributed to high localized input energy density and consequently evaporation of molten metal. It should be mentioned that

increase in hatch distances without raise in laser power also leads to high porosity percentages (Figure 4.12).

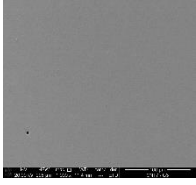
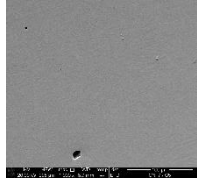
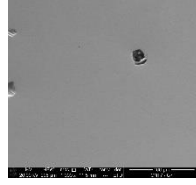
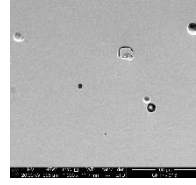
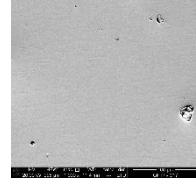
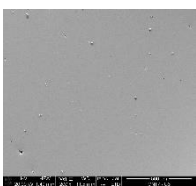
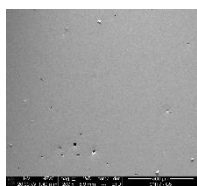
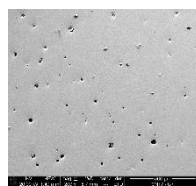
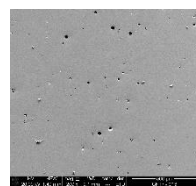
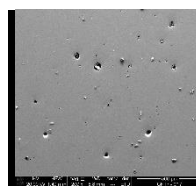
														
														
C3	P	70	C5	P	70	C7	P	94	C13	P	70	C17	P	150
	V	1100		V	1000		V	700		V	700		V	700
	dh	0.06		dh	0.06		dh	0.1		dh	0.06		dh	0.1
	E	42.4		E	46.6		E	53.7		E	66.6		E	85.7
	P%	0.024		P%	0.057		P%	0.462		P%	0.33		P%	0.32

Figure 4.12– Scanning electron micrographs of SLM NiTi (according to Table 4.3) samples after polishing (P%: porosity percentage calculated by image processing applied on SEM micrographs)

As presented before, NiTi sample produced by HP parameters (Table 4.4) demonstrated the minimum surface roughness. Internal defect analysis using micro CT (see Figure 4.13) also revealed that, NiTi sample produced by HP parameters has the minimum porosity percentage (i.e. 0.02 %, against 0.04 % of MP parameters and 0.06 % of LP parameters). It should be mentioned that the median pore size in HP sample is lower than those of LP and MP samples. In fact, high laser power adjusted to increased scanning speed and increased hatch distance could control the evaporation and consequently the internal micro porosity.

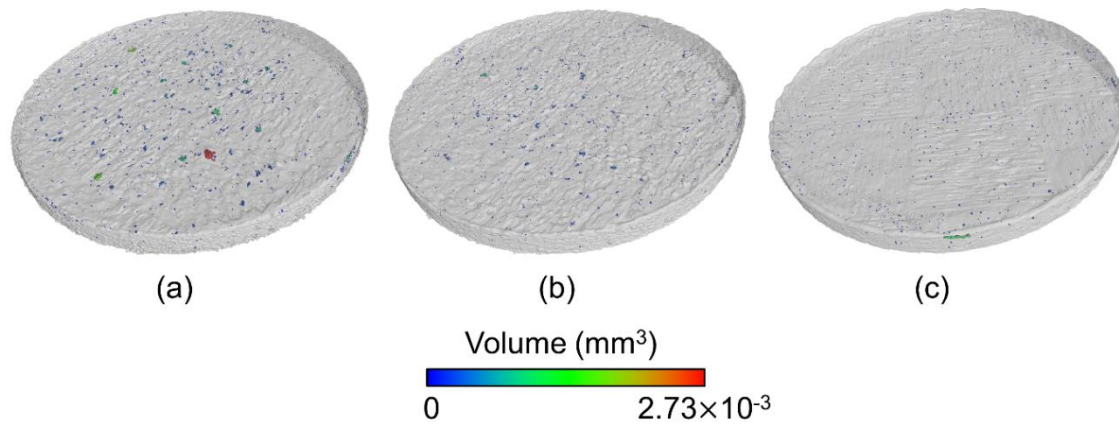


Figure 4.13– Porosity analysis conducted on CT scanned samples LP (a), MP (b) and HP (c).

The detected pores are colored based on their volume

It can be concluded that, using small spot laser diameter ($30 \mu\text{m}$) decreases the dimension of melt pool and consequently leads to severer rapid solidification. But, at the same time high power increases the temperature of melting pool and causes to grain coarsening. Comparison of XRD patterns of LP and MP revealed that broadening and decrease in peak heights has happened due to rapid solidification and low laser power which encourage very fine micro structure and high level of micro strain. Three different regimes of process parameters have been successfully utilized in this research to obtain the single phase B2 Austenite phase after SLM of $\text{Ni}_{50.8}\text{Ti}_{49.2}$ powder. Optimized SLM process parameters ($P=150 \text{ W}$, $V= 1100 \text{ mm/sec}$) led to the minimum porosity and surface roughness of 0.02% and $10 \mu\text{m}$ respectively.

4.2 Design and manufacture of self-supported scaffolds

AM processes being able to create very fine features such as porous scaffolds or lattice structures. Lattice structures are attractive because they can increase the strength-to-weight ratio, offer the ability to tailor stiffness, damage tolerance, and significantly increase the surface area. Such components have thousands of nodes. Regular porous scaffolds or lattice structures are produced almost exclusively through AM. There is no traditional subtractive technology capable of fabricating such component. Internal features have no line of sight for tooling access. They are complicated and time consuming to manufacture using AM; however, these AM components offer the greatest potential advantage such as bone ingrowth in porous orthopaedic stents and weight loss in transportation industries. In this thesis and in collaboration with a master student in Te. Si lab (Jessica Rocco), SLM was used for fabrication of stainless steel lattice structures. In the first step, the effect of SLM process parameters on microstructure and quality of products was investigated using different destructive and non-destructive methods. In the second step, topology optimization was done to improve the productivity of SLM for fabrication of stainless steel 316L porous scaffolds.

4.2.1 The effect of SLM process parameters on microstructure of stainless steel 316L alloy

Attributing to the combination of high corrosion resistance and good weldability, 316L austenitic stainless steel is becoming an important solution in a variety of applications [93]. Compared to 316 stainless steel, 316L alloy is known by high resistance to radiation, high loads and less carbide precipitation due to welding. AM enables the fabrication of innovative structures with complex geometries and desired microstructures. SLM process is characterized by a strong directional heat transfer resulting in a strong textured microstructure. In this section, microstructure and textural evolution of stainless steel 316L (SS316L) during selective laser melting process have been studied. The original approach in this study is to investigate the effects of changing the process parameters on microstructural and textural evolution in volume of the sample in condition of constant input energy. The influence of laser power and scanning speed on phase formation, microhardness, density and textural evolution was investigated.

The XRD patterns of the SLM SS316L samples, fabricated using different scanning speeds and laser powers, are shown in Figure 4.14.

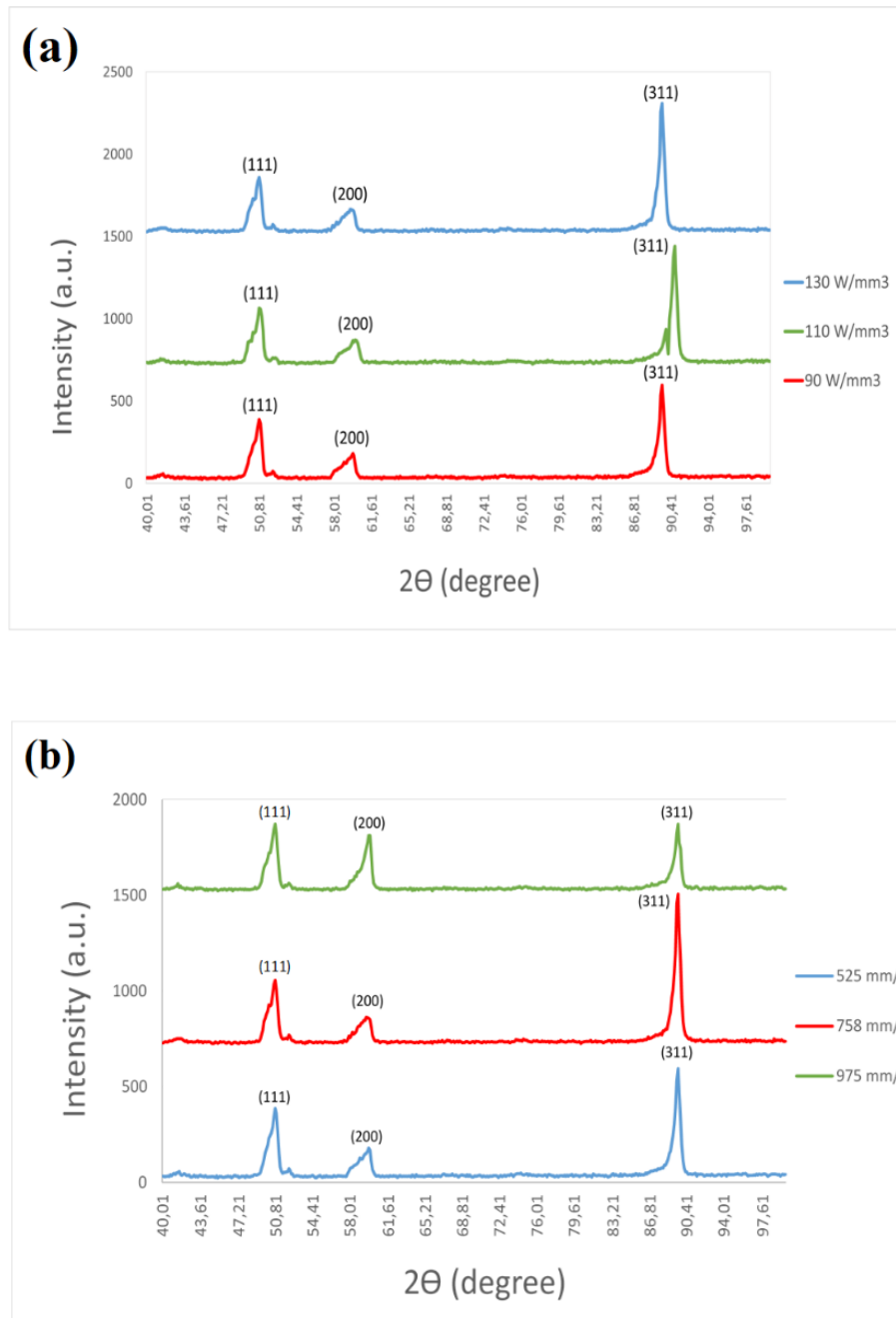


Figure 4.14– XRD patterns of the SLM SS316L produced by different (a) laser powers and (b) scanning speeds.

As can be seen in Figure 4.14 (a and b), the phase composition of 316L parts fabricated by SLM process is not susceptible to the change in laser power or scanning speed. A slight displacement in the position and change in peak height of Austenite phase at $2\Theta = 89^\circ$, can be attributed to the rapid solidification phenomenon in SLM process that leads to grain refinement and microstrain distribution through the microstructure based on the intensity of cooling stage. It is important to note that after solidification, the austenite (FCC phase) is the only present crystalline phase and no trace of ferrite (BCC phase) has been detected. Microhardness depends directly on the phase composition of SLM parts. As a consequence of the phase composition of the samples referred as almost the same, it can be seen in figure 2 that the microhardness value remains almost constant by changing the laser power and the scanning speed. The microhardness of built parts is between 219 to 232 HV.

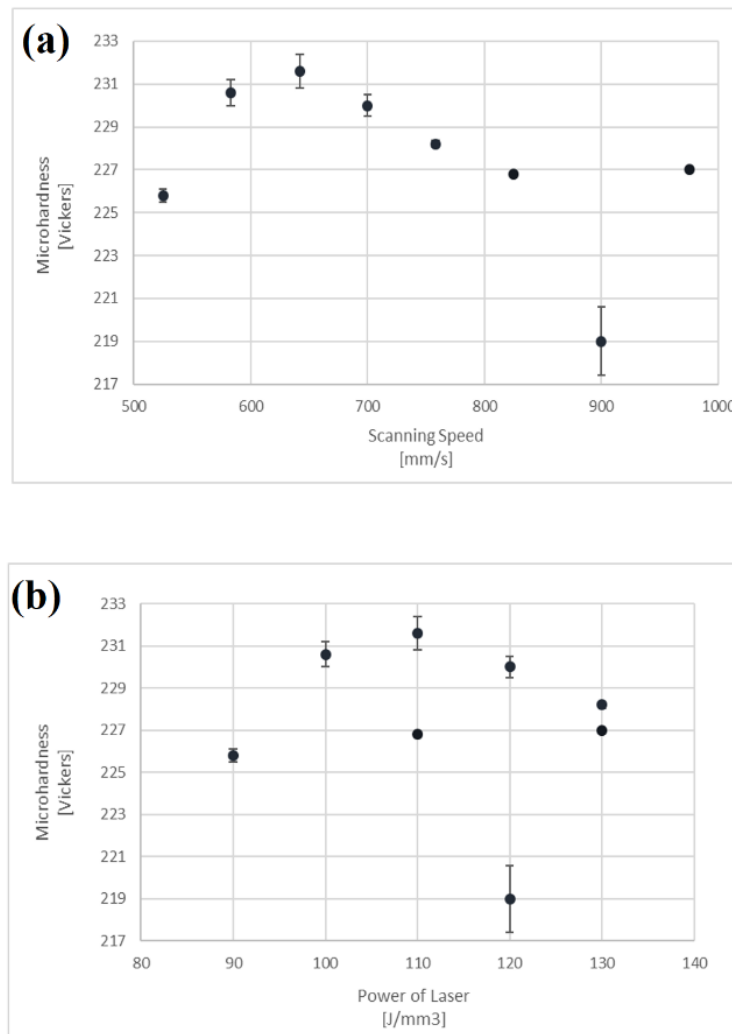


Figure 4.15– Microhardness values of SLM SS316L parts as a function of (a) scanning speed and (b) laser power

SS316L is an austenitic stainless steel and contains predominant γ phase after solidification. Figure 4.16 (a) shows austenitic columnar grains growing parallel to the building direction (from the bottom to the top). Local temperature gradients and solidification at the solid-liquid interface are a consequence of the SLM process parameters. High energy density, high scanning speed and low laser power promote the columnar grain epitaxial growth to the surface [94]. As it can be seen in the Figure 4.16 (b), the grains (are marked by red lines) grow in parallel manner - or almost - to building direction, despite the tracks produced by the laser (blue lines). Epitaxial nucleation along several melt pools, resulting in elongated grains [95], could

cause an anisotropy of mechanical behaviour. It can be seen in Figure 4.16 (b) that the direction of solid-liquid growth interface could change, inside the same grain, from one melt pool to the following.

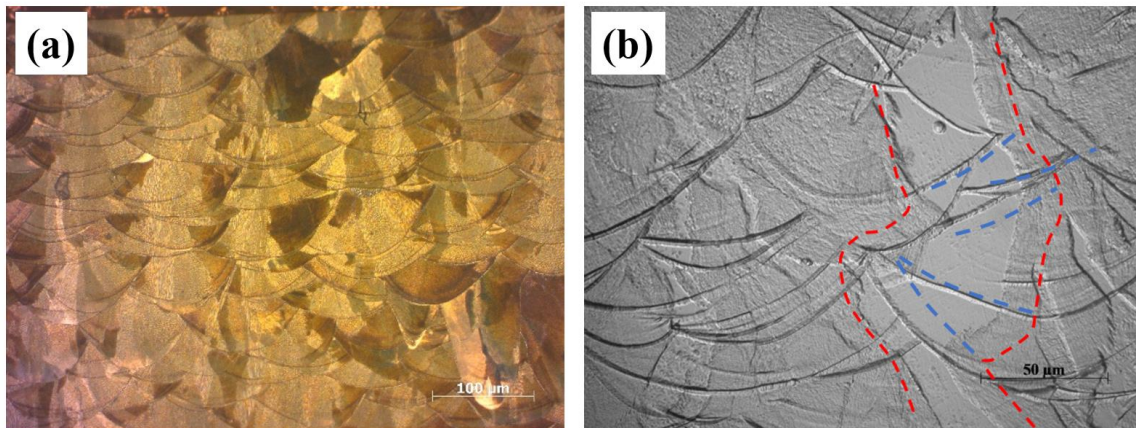


Figure 4.16– (a) Microstructure of SLM SS316L in a cross-section parallel to the building direction (BD) - photo obtained through optical microscope and magnification 200x, (b) epitaxial growth of SLM SS316L – photo obtained through SEM and magnification 500x along BD

Grains orientation distribution or texture of SLM parts is also of great importance because texture remarkably has effect on mechanical properties of final products. Textural evolution during SLM process of the cubic stainless steel 316L samples was analysed using EBSD and along the building direction. The analyses have been done on two samples built with a large difference in laser powers. As it can be seen in Figure 4.17 (a, b) from pole figures, sample built using lower laser power has a stronger [111] fiber texture. The major of grains has nearly [111] orientation along with normal direction (ND) of the sample. In the other hand, Figure 4.17 (c, d) depict a random texture for the sample produced by high laser power. The grains of the sample, built at higher laser power, are randomly oriented. It can be attributed to the decrease in temperature gradient. Considering the small laser spot (30 μm), high laser power decreases the temperature gradient and consequently the directional growth and preferentially oriented grains.

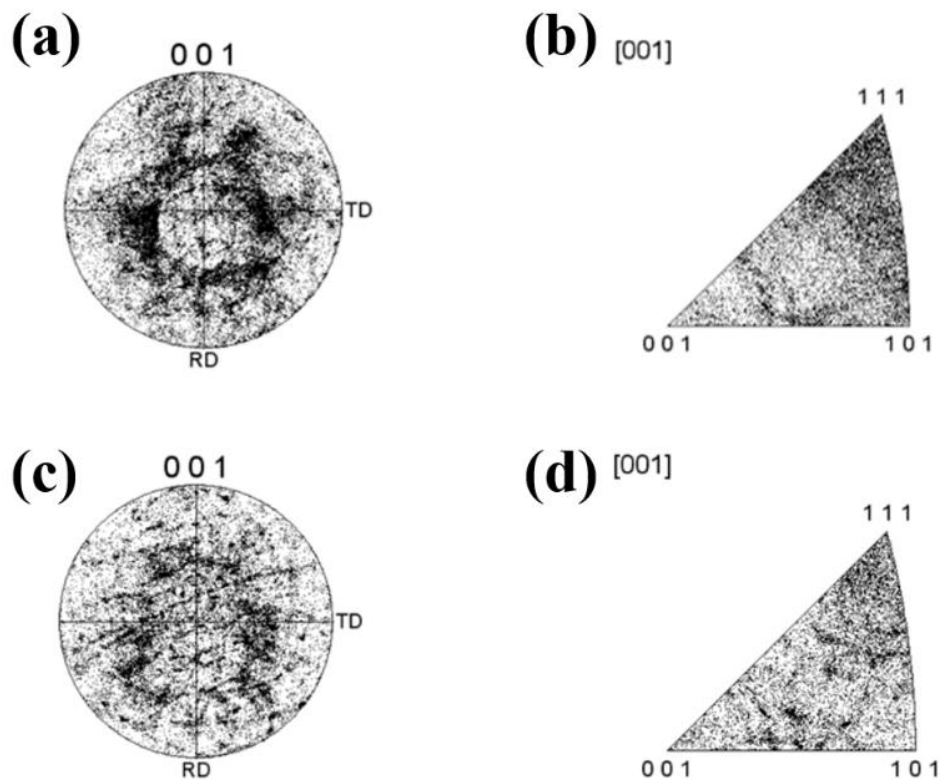


Figure 4.17– (001) pole figure and inverse pole figure of SLM SS316L produced by (a, b): 90 W and (c, d): 130 W power of laser

4.2.2 The effect of pore shape on productivity of lattice structures

Production of complicated geometries such as lattice structures using powder bed techniques like SLM have some limitations in terms of support design and support removal. There are many non-accessible internal parts in lattice structures which are quite impossible to remove their supports. Therefore, design and manufacture of self-supported structures is an interesting way to overcome these difficulties. Support structures are indispensable under certain conditions to ensure manufacturability. These conditions are called “critical factors”:

- For certain angles, support structures are necessary since the overhang cannot be supported sufficiently by the subjacent layers.
- If the angle of surface is smaller than 40-45°, support structures are necessary (see Figure 4.19. The exact angle has to be verified for the respective AM machine and the

material used. Moreover, additional critical factors such as overhangs and process forces should be taken into the account.

Creation of self-supported features by topology optimization is an important step in design and manufacturing of lattice structures. As can be seen in Figure 4.19, two designs based on the same size unitcells and different geometries were manufactured using SLM process in this research. In design 2 and keeping the dimension and porosity percentage of design 1, straight struts were substituted with curve struts. This new design reduces the over angle surfaces and increases the productivity as can be seen in Figure 4.19 on transverse direction of design 2.

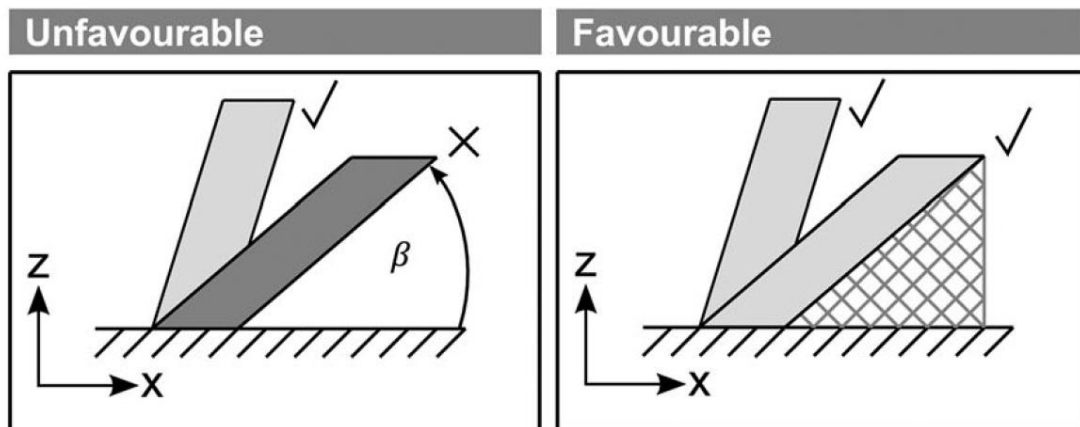


Figure 4.18– Support design for over angle surfaces

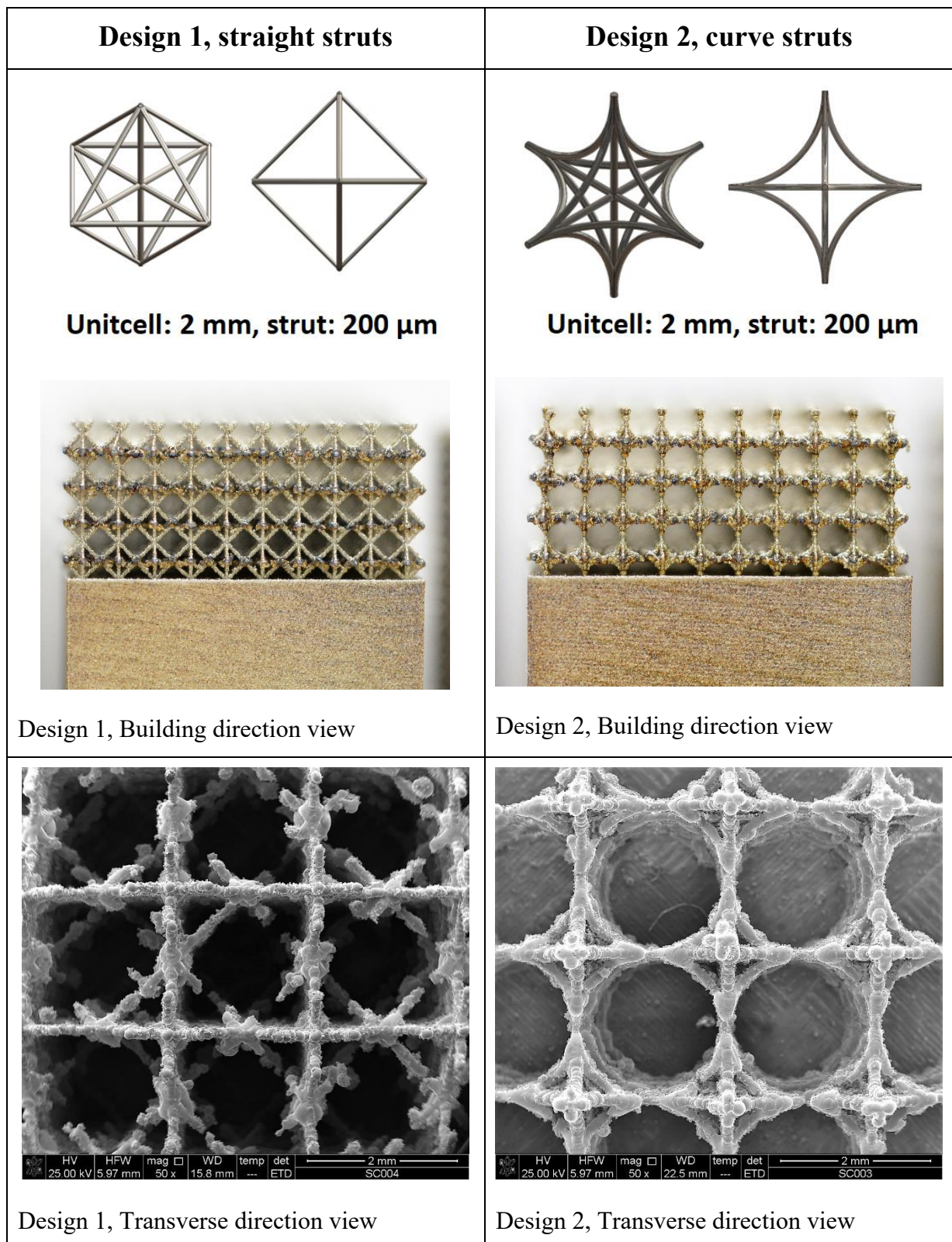


Figure 4.19– The effect of topology optimization on productivity of self-supported scaffolds

4.2.3 The effect of porosity distribution on mechanical properties

The morphology and distribution of porosity is an important parameter in design and manufacture of self-supported scaffolds. In this section and using Finite Element Method (FEM) (Appendix F) and experimental procedures, the effect of pore shape and distribution has been studied in Ti6Al4V hollow samples.

For the investigation of pore morphology and pore distribution on mechanical properties of porous samples, 5 hollow Ti6Al4V samples with the same porosity percentage but different geometry and distribution of holes were designed and manufactured by SLM that are presented in Table 4.6 and Figure 4.20. To evaluate the mechanical properties of porous Ti6Al4V samples, compression test with constant strain (1%) was used. This value is consistent with other compression tests in the literature [96]. Non-linear-elastic finite element model was used in this thesis. In elastic region, linear isotropic behaviour and in plastic region, multilinear isotropic hardening and model were applied.

Table 4.6– CAD designs of Ti6Al4V hollow samples with the same porosity (35%) and different pore shape and distribution

Sample 1	Sample 2	Sample 3	Sample 4	Sample 5

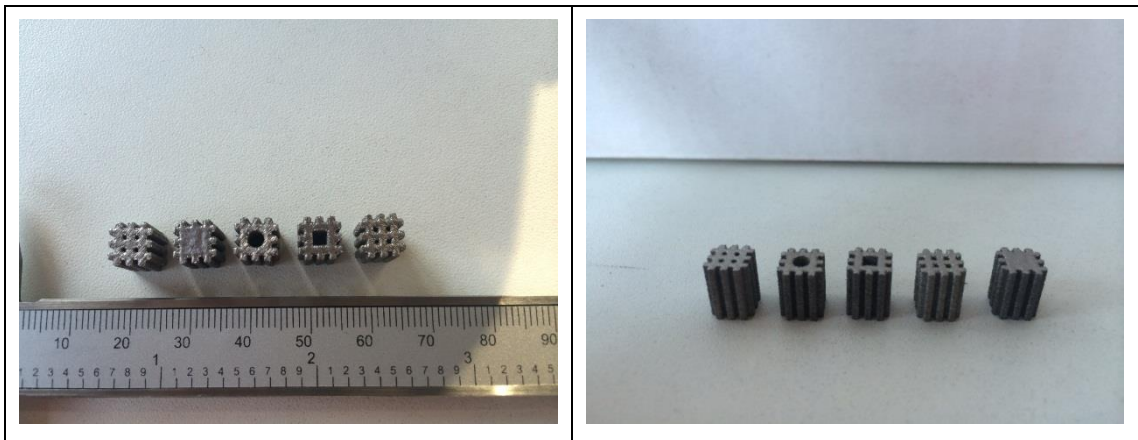


Figure 4.20–Ti6Al4V hollow samples with the same porosity (35%) and different pore shape and distribution produced by SLM

Distribution of elastic stress in pressure direction for five hollow Ti samples is presented in Figure 4.21. As can be seen in Figure 4.21 (a), development of low compressive stressed regions in sample 1 without internal holes is less than other hollow samples with internal channels. These kind of internal channels are typical in bony structures. Formation of a region with low compressive stress and 45° inclinations to the planar surface in hollow samples (samples 2-5, Table 4.6) proves that progress in deformation leads to formation of tensile stress regions at the centre of samples. In sample one (Figure 4.21 (a)) there is more tendency for buckling in comparison with samples containing internal holes (samples 2 to sample 5). At higher strains and plastic deformation area, distribution of plastic strain depends on design of porosity as presented in Figure 4.22 and Figure 4.23.

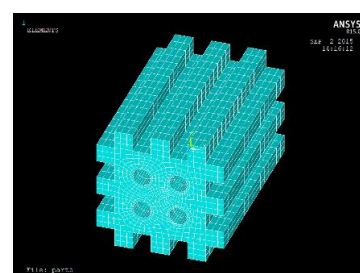
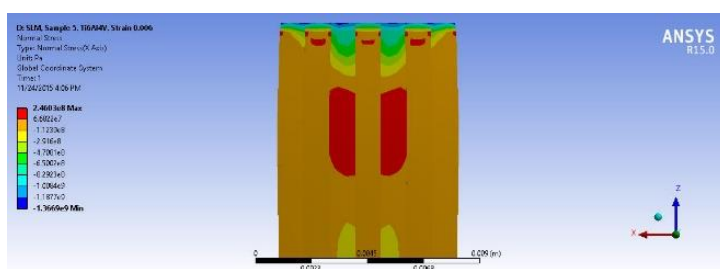
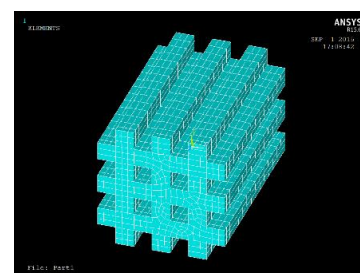
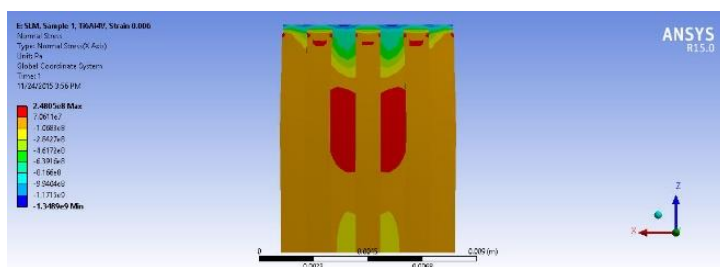
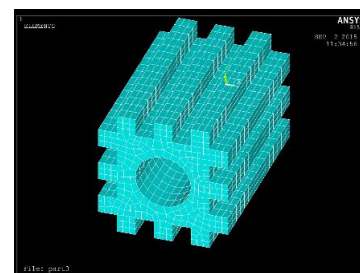
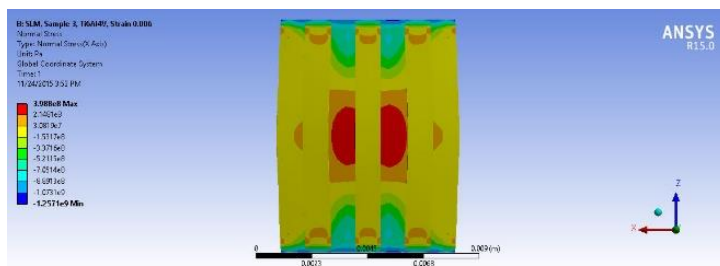
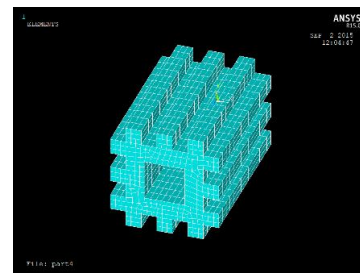
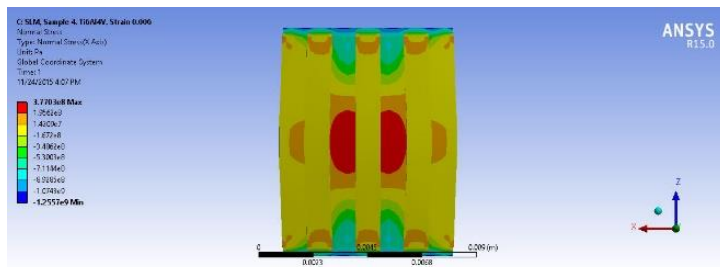
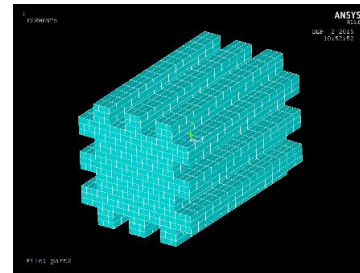
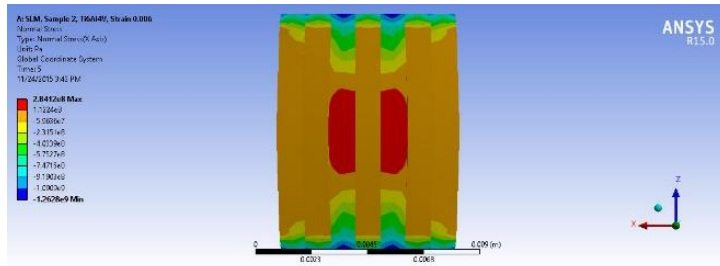


Figure 4.21– distribution of elastic stress in hollow NiTi FEM designs in uniaxial compression direction.

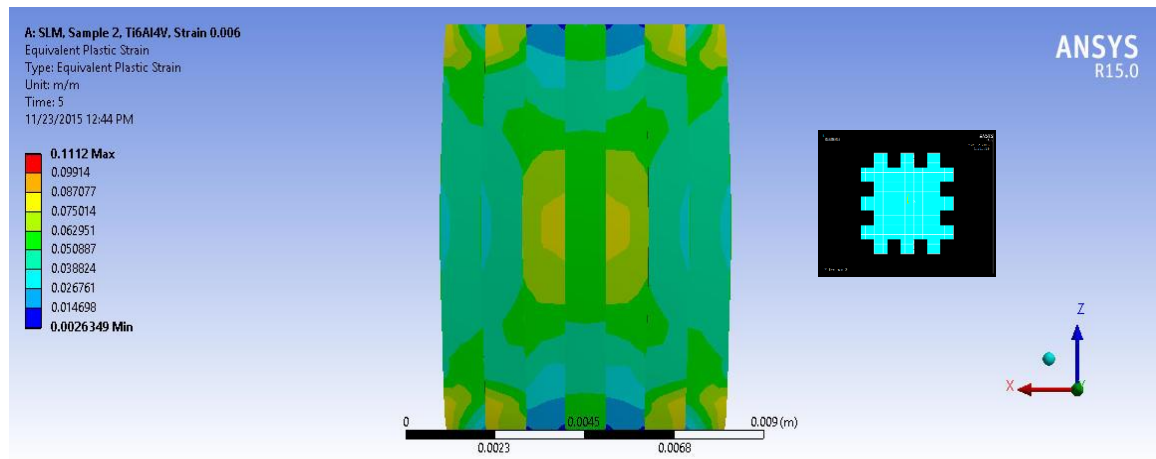


Figure 4.22– distribution of plastic strain in transverse direction of sample 1 according to Table

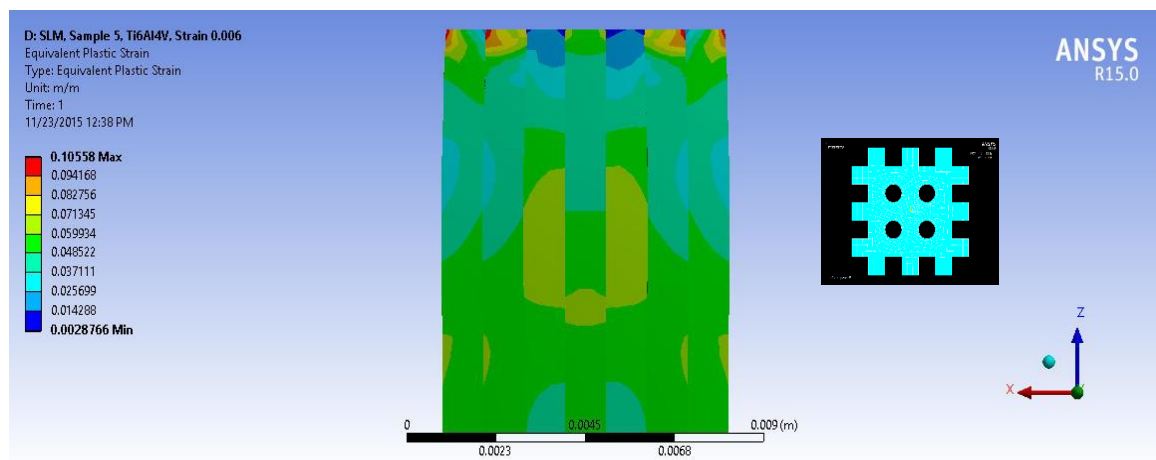


Figure 4.23– distribution of plastic strain in transverse direction of sample 5 according to Table

As can be seen in Figure 4.23, presence of internal circular holes leads to non-symmetric distribution of plastic strain. This phenomenon inhibits the development of area with high plastic stains and increase the strength.

Figure 4.24 shows the stress-strain graphs related to finite element simulation of uniaxial compression tests on hollow Ti samples presented in Table 4.6. The graphs have been calculated using response force of surface nodes.

Figure 4.24 (FE model) and Figure 4.25 (experimental compression test) show that hollow Ti samples do not have significant difference in terms of stiffness. It can be attributed to the same porosity percentage. It is consistent with the results of elastic stress and strain distributions. From Figure 4.24 it can be understood that strength of hollow samples containing circular holes (samples 4 and 5 according to table) are more than those hollow samples containing rectangular holes. Moreover, homogenous distribution of circular holes increases the strength of structure in comparison to the sample with central circular hole (Sample 4 Vs sample 5).

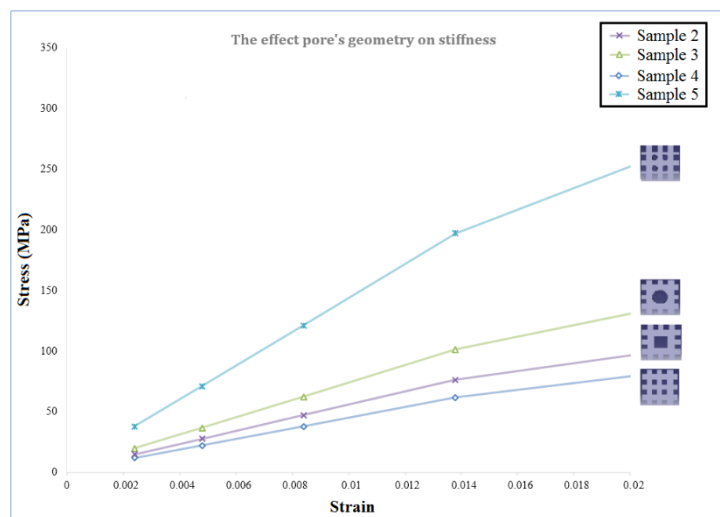


Figure 4.24– FEM stress-strain curves of Ti6Al4V hollow samples with different geometries and distribution of pores

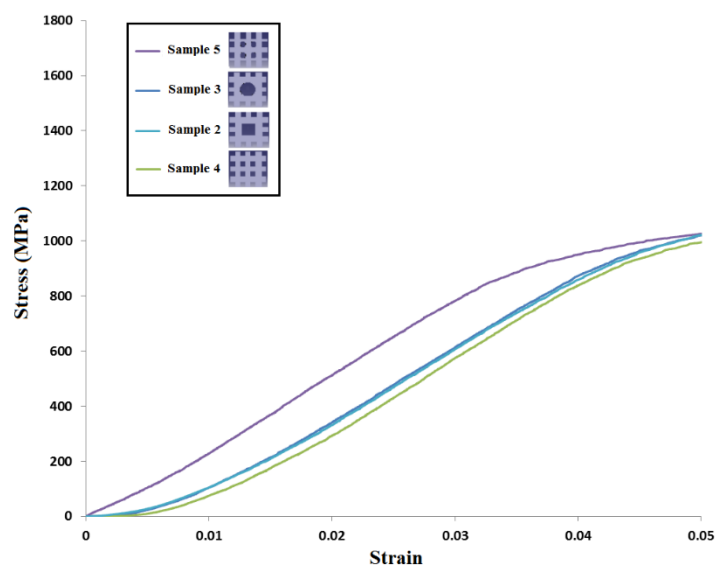


Figure 4.25– stress-strain curves of Ti6Al4V hollow samples with different geometries and distribution of pores, uniaxial compression test (parameters same as FE modeling)

Based on the obtained results for the effect of morphology and distribution of pores on mechanical properties of porous scaffolds, 3 NiTi lattice structures with 35, 42 and 56 % of porosity were designed and manufactured using SLM process (see Figure 4.26). Stress-strain curves of three NiTi scaffolds from uniaxial compression tests at room temperature are presented in Figure 4.27. Based on Figure 4.27, elastic modulus of NiTi lattice structures was calculated by measuring the slope of elastic region of stress-strain curves. Table 4.7 are summarized the comparison between elastic modulus of dense stainless steel 316L, Ti6Al4V, SLM NiTi, three designed scaffolds and human bone. Scaffold with 35% porosity was designed according to the average porosity of human bone considering 50% trabecular and 50% cortical bone. Table 4.7 depicts that NiTi lattice structure with 35% porosity has similar stiffness to human bone.

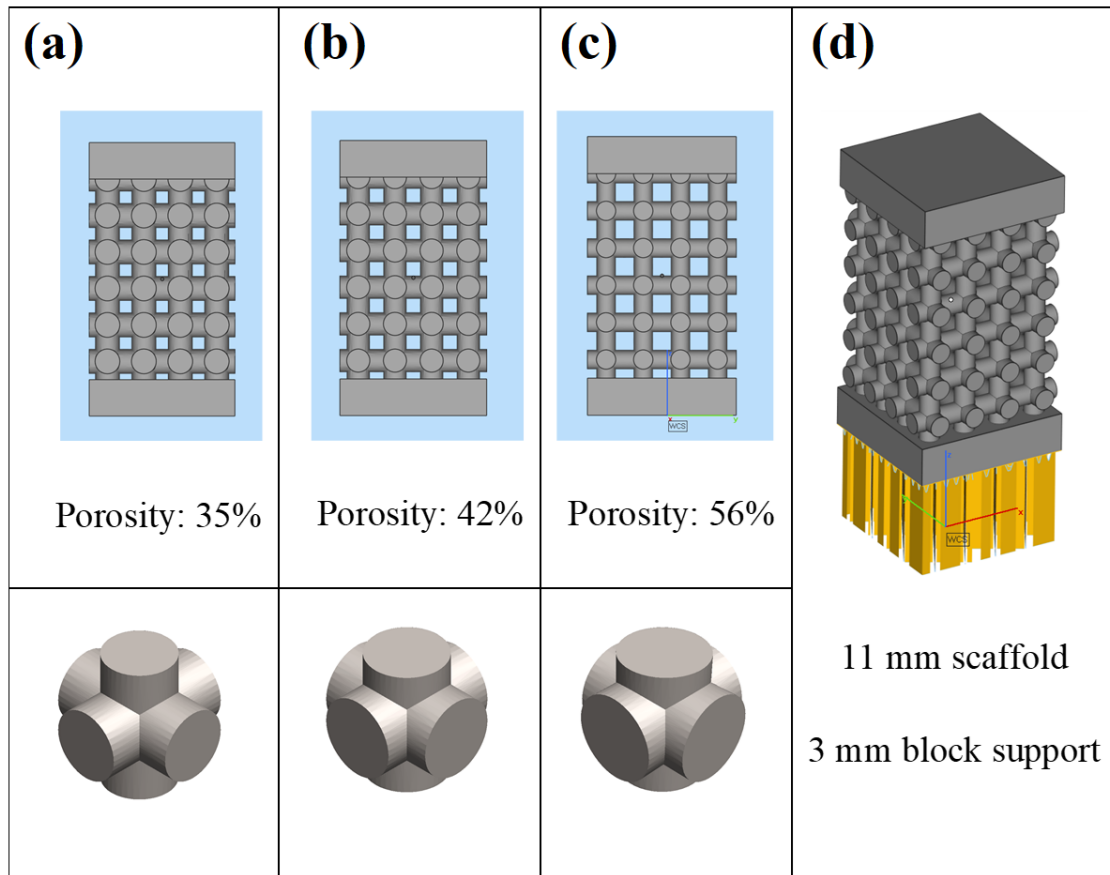


Figure 4.26– regular porous scaffolds and related unitcells with (a) 35%, (b) 42% and (c) 56% porosity designed by Magics software, (d) 3 mm block support designed for scaffolds

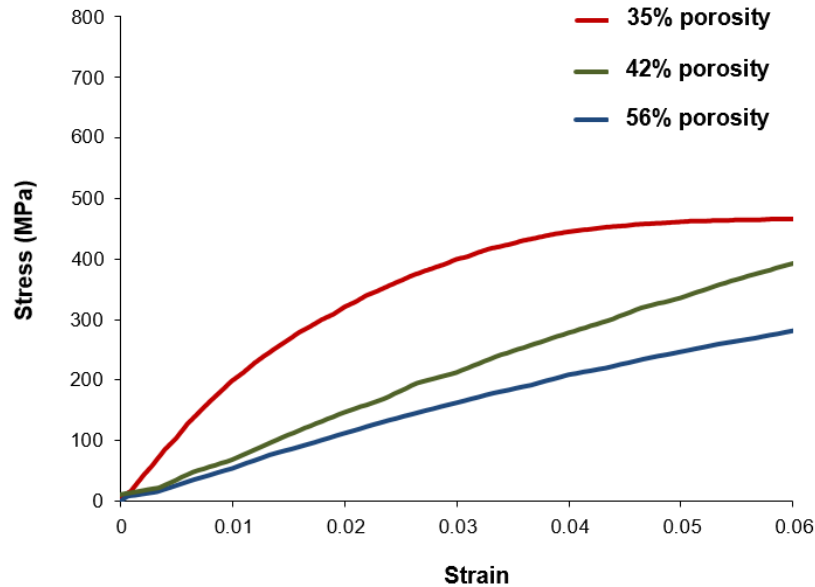


Figure 4.27– stress-strain curves from uniaxial compression test of NiTi porous scaffolds (see fig) produced by SLM

Table 4.7– elastic modulus (stiffness) of porous NiTi produced by SLM in comparison to other synthetic and natural materials

Material	Elastic Modulus (GPa)
316 Stainless Steel	193
Ti6Al4V	116
SLM Nitinol	38.5
SLM Nitinol: 35% Porosity	22.2
SLM Nitinol: 42% Porosity	7.3
SLM Nitinol: 56% Porosity	5.6
Bone [97]	11-18

4.3 NiTi porous scaffolds and bone printing

4.3.1 Computed tomography of bone biopsy

In order to determine the internal architecture of human bone, it is necessary to characterize the bone tissue biopsy. In this research and with the collaboration of medicine school of University of Padova, 10 bone biopsies were prepared. Bone biopsies were dehydrated and embedded in methacrylate. Eight samples had to be rejected based on the controlled cross-section by scanning electron microscope. The main criteria that must be fulfilled is the presence of both cortical and trabecular bone in biopsy. Finally, a small part of vertebral bone was selected as an ideal biopsy containing both bone types belongs to a 35 years old patient. Biopsy was selected for investigation by micro CT (Figure 4.28). The biopsy was not collected specifically for this study and it was a pre-existing sample at orthopaedic section of medicine school. In order to have a compatible model of the real bone, the resolution of CT should be small enough to analyse the microarchitecture. Micro MRI using magnetic field of 7T can reach to resolution of $137 \times 137 \times 410 \mu\text{m}^3$ [98]. Computed tomography in micro scale (mCT) can provide better resolution depend on voxel and sample sizes. In our system, the best resolution is around $3 \mu\text{m}$.

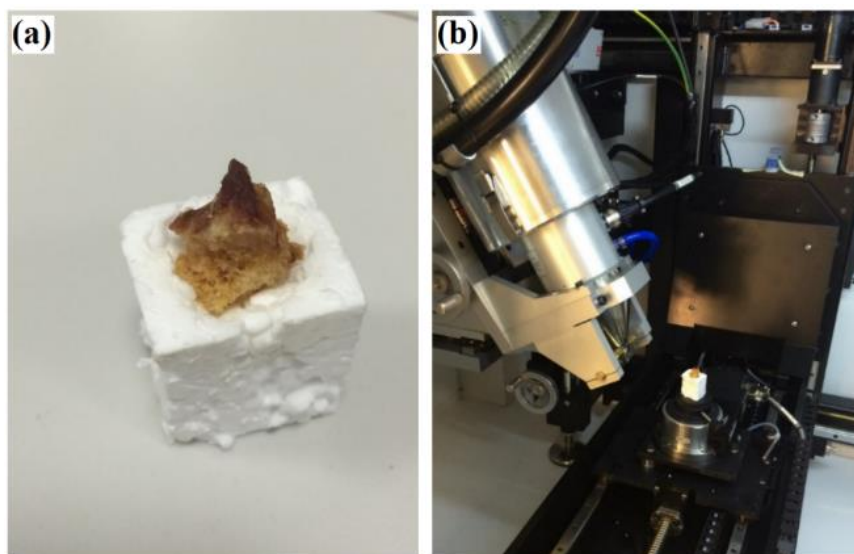


Figure 4.28– (a) human bone biopsy (collaboration with medicine school, UNIPD), (b) positioning of bone biopsy in micro computed tomography for scanning

Firstly, the region of interest (ROI) were defined in a manner to include both cortical and cancellous bone and the 3-D bone volume was rendered (Figure 4.29). Secondly, in both cortical and cancellous parts, two unitcells were selected using VG studio software. Biopsy has two distinct regions of cortical and cancellous bone. However, it was difficult to define exactly a border between two regions. In this project there was no need to define a border between two types of bone because the goal was the selection of suitable unitcells in both regions. The procedure is schematically presented in Figure 4.30. The unitcells were cut at surfaces to have flat surface which is convenient for the replication. The cortical and cancellous bone unitcells were processed using Netfabb software which is a common tool for editing STL files.

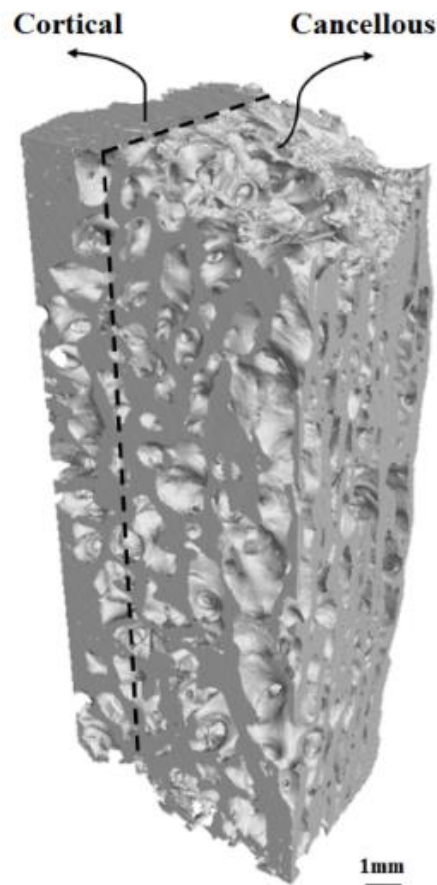


Figure 4.29– Biopsy comprising cortical and cancellous

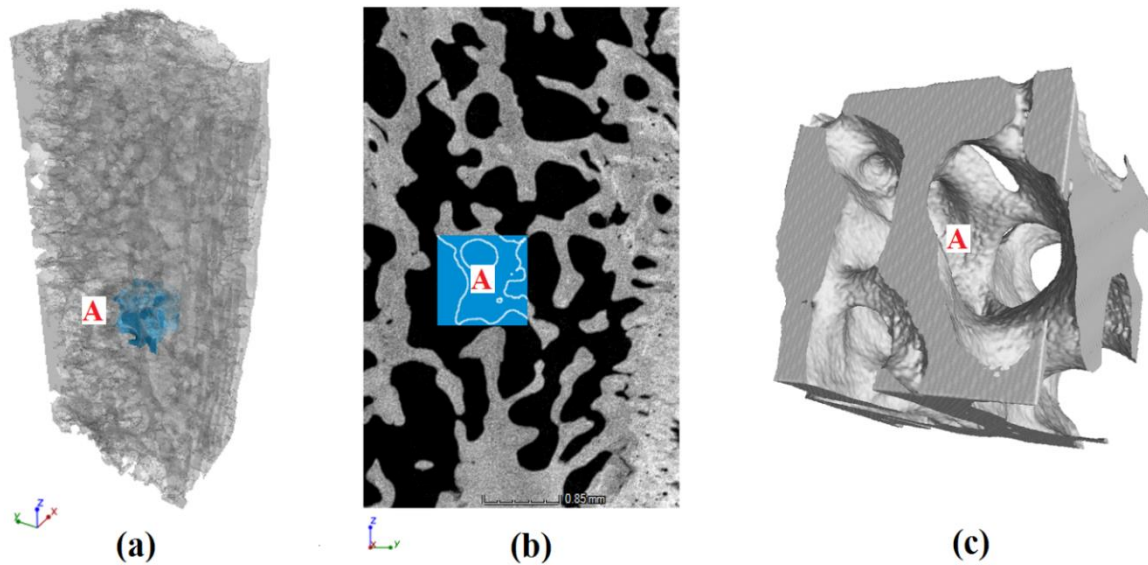


Figure 4.30– (a) micro CT scanning of bone biopsy, (b) selection of unitcell in 2-D view, (c) 3-D view of selected trabecular unitcell

After making the cuts and selection of unitcell from both cortical and cancellous bone, the STLs were transferred to *Magics (Materialise)* software for clean-up and replication.

The problem with STL file manifests itself after replication to create a scaffold from the STL shell of a unitcell. A repair tolerance of 2 μm was used which is less than the scan resolution. Geometrical STL fixing was done using different diagnostic filters to fix inverted normal, bad edges, bad contours, near bad edges, planar holes, shells, possible noise shells, overlapping triangles and intersecting triangles. After having filtered, aligned, and cropped the STL file in *Magics*, it was imported into *Autofab* software where the process parameters were defined. The process parameters were chosen based on the results presented in section 4.1.1 for border and internal parts.

4.3.2 Support design for NiTi scaffolds

Selection of appropriate process parameters for the support has an important effect in implementation of support and consequently the built. Well-designed support can act as a suitable heat sink. To compare the effect of laser power in support production, two different scaffolds were produced using same process parameters for the samples and different laser

powers for the support. Design of experiment and visual results of experiment are shown in Table 4.8 and Table 4.9.

Table 4.8– Design of experiment, support design for NiTi scaffolds

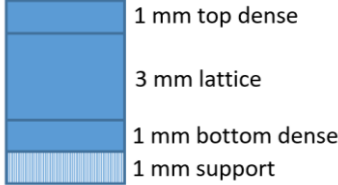


Oxygen level	0.02 (200-250 ppm)
Strategy	Chessboard mender hatch with connected lines
Sample Geometry	 <p>1 mm top dense 3 mm lattice 1 mm bottom dense 1 mm support</p>
Platform	Titanium
Unit-cell	Straight cross, (1mm×1mm×1mm)
Hatch distances	All contour and hatch distance: 0.06 mm

Table 4.9– Support design for NiTi scaffolds

Sample	Sample parameter	P (support)	V (support)	
Low power support	C3 (Table 4.3)	49	437	
Low power support	C3 (Table 4.3)	70		

As can be seen in Table 4.9, low laser power can implement better support structure. It can be attributed to the accelerating and deaccelerating during the production of porous structure such as supports. In fact, variation of laser power in short length distance is too much when high laser power is used.

4.3.3 Design and SLM fabrication of regular and natural porous scaffolds

Treatment of segmental bone defects is known as a complex procedure in orthopedic surgery. Orthopedic regenerative medicine based on the implementation of bio-inspired metallic bone scaffolds is a new and promising approach. An ideal metallic implant mimicking natural bone should be at least partly porous and have sections with controlled anisotropy. Despite recent advances in biomaterials, design and fabrication of bio-inspired scaffolds still remains a challenge. In this thesis, we tried to design and manufacture gradient porous structures with consecutive regular and natural CT-based lattice structures. Surmeneva [99] et al. have produced graded porous structures by electron beam melting (EBM) process and they reported that, graded structures are more ductile in comparison with normal lattice structures (see Figure 4.31).

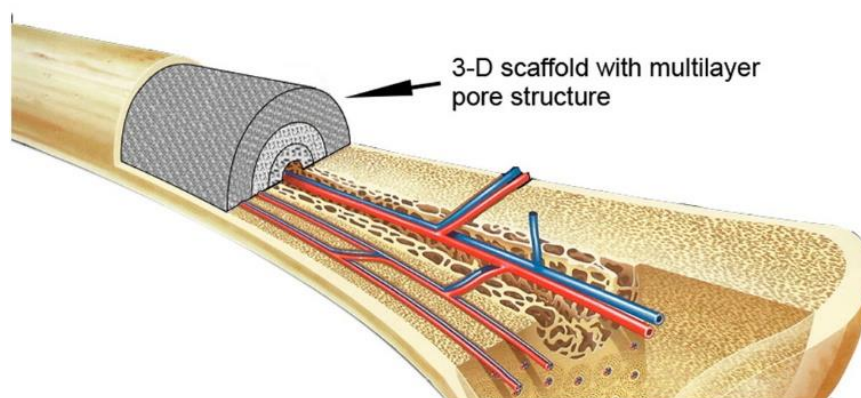
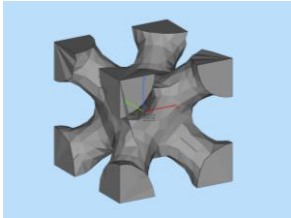
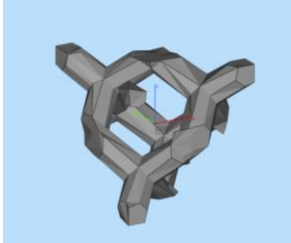
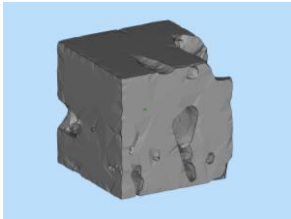
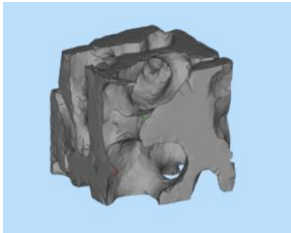


Figure 4.31– A structure of scaffold in substitution of bone tissues, which mimics the internal pore structure of bone tissues [99]

For the porous structures which are based on regular unitcells, we used “regular scaffold” term and hereafter this term will be used for these kind of scaffolds. In opposite, the porous scaffolds based on computed tomography of bone are named “natural scaffolds”.

For the regular scaffolds, the first design stage was done using general CAD program SolidWorks by Dassault Systemes, SolidWorks Corporation. As stated in section 4.3.1, two processed natural unitcells were prepared for fabrication of natural porous scaffolds. Moreover, two regular unitcells were selected based on the porosity measurements of natural bone. Table 4.10 shows the basic outline of the wire-frame body centered cubic (FEM), diamond-like, natural cortical and trabecular unitcells chosen in present research.

Table 4.10– Natural and regular unitcells according to the computed tomography of cortical and trabecular bones

Unitcell	Original Dimensions	Porosity	photo
FEM	Free	56%	
Diamond20	Free	20%	
Cortical1	1×1×1 mm from CT	17%	
Trabecular1	1×1×1 mm from CT	52%	

Since FEM and diamond unitcells have simpler structures as compared to many other types of open unitcell geometries, it is easier to fabricate them using additive manufacturing techniques [100]. Additionally, FEM and diamond unitcells have similar porosity percentages with CT obtained natural trabecular and cortical unitcells respectively. The diamond unitcell geometry also presented a more uniform distribution of stress within the struts than other unitcells, such

as cubic or octahedral [101] . Both unitcells are symmetric, e.g. all three dimensions are identical and referred to as the size of lattice cell.

At this stage of research, scaffolds of trabecular types were designed using FEM and natural trabecular unitcells (Table 4.10). The design of experiment for generation of trabecular porous scaffolds is presented in Table 4.11. As can be seen in Table 4.11, 11 mm cylindrical scaffold was designed on 2 mm dense part and 3 mm support structure. Trabecular structures were generated by structure module of software package Magics by Materialise. During this stage, basic cylindrical geometries were used as the templates, “filled” by the lattices generated from selected library cells of chosen dimensions (FEM 1mm, FEM1.5 mm) and natural trabecular unitcell coming from computed tomography analysis of real bone. Struts of these cells are represented by the wires having no actual thickness, only cell sizes and cell types are used as parameters. As stated before, production of such complicated structures using SLM technique, requires a combination of different regimes of process parameters for the boarder and internal parts of the samples. Based on the given results in section 4.1.1, HP parameters were used as the scanning parameters for the internal parts and MP parameters were utilized for the borders (Figure 4.32). It should be mentioned that previous experiments revealed that both MP and HP parameters lead to single phase B2-Austenite.

Table 4.11– Design of SLM experiment, NiTi trabecular scaffolds (natural and regular)

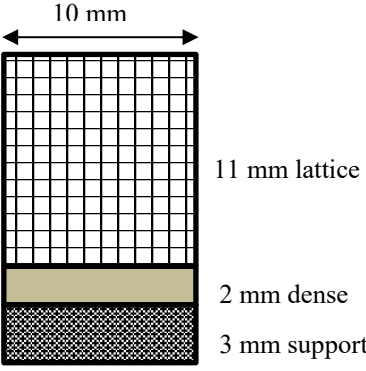
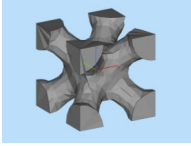
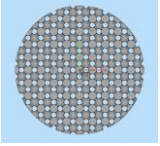
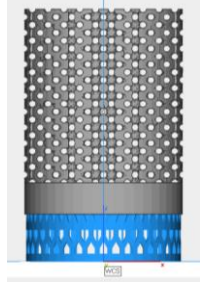
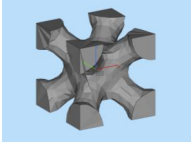
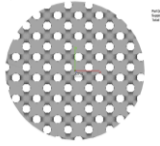
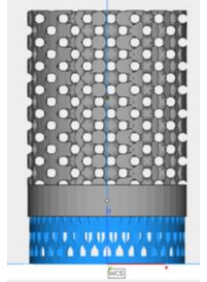
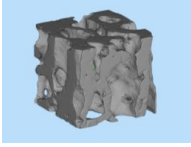
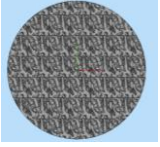
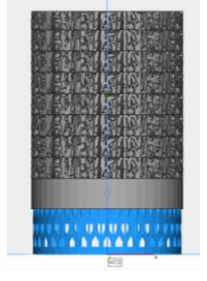
% O ₂	0.02 (200-250 ppm)
Strategy	Chessboard mender connected lines
Sample Geometry	 <p style="text-align: center;">10 mm</p> <p style="text-align: right;">11 mm lattice 2 mm dense 3 mm support</p>
Platform	Titanium
Hatch distances	All contour and hatch distance: 0.06 mm
t (layer thickness)	0.025 mm

Table 4.12– NiTi natural and regular scaffolds based on the porosity of trabecular bone

Sample	Part parameter (Internal-Border)	Unitcell	Scaffold (top)	Scaffold (lateral)
S _{F1}	HP-MP	 FEM, 1 mm, 56%	 Dhole: 0.45 mm	
S _{F1.5}	HP-MP	 FEM, 1.5 mm, 56%	 Dhole: 0.65 mm	
S _{T1.5}	HP-MP	 Trabecular1.5, 1.5 mm, 52%	 52% porosity	

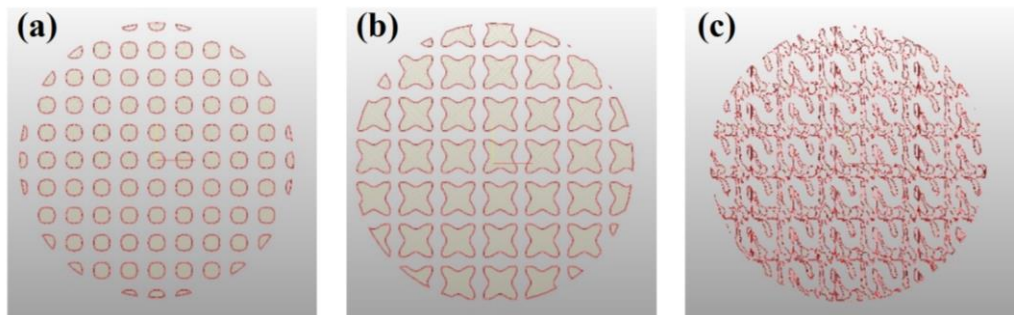


Figure 4.32– applying different SLM regimes for boarder (MP) and internal (HP) in regular and natural trabecular scaffolds (a) S_{F1} , (b) $S_{F1.5}$, (c) $S_{T1.5}$ (Table 4.12).

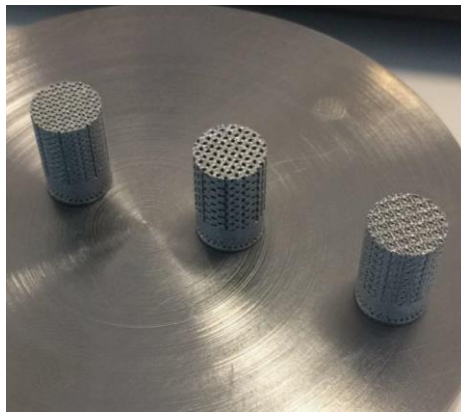


Figure 4.33– NiTi trabecular scaffolds based on natural and regular unitcells presented in Table 4.12 produced by SLM.

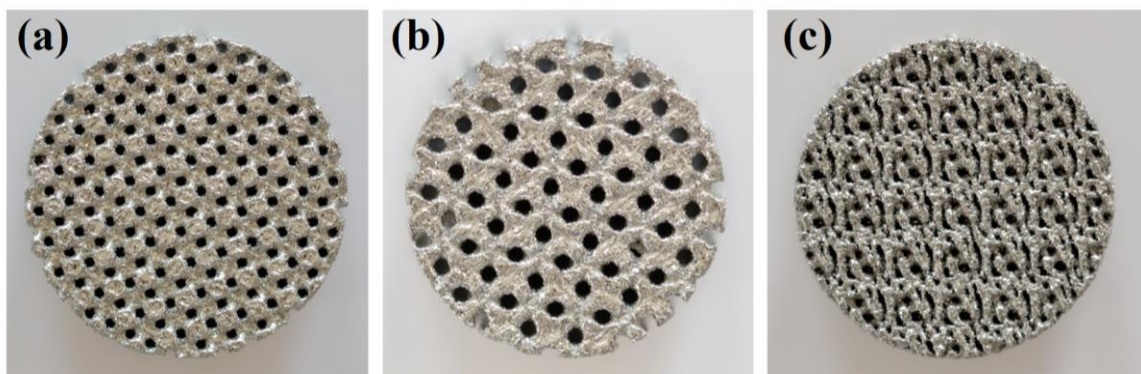
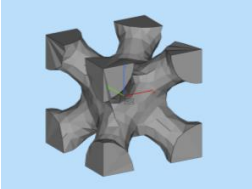
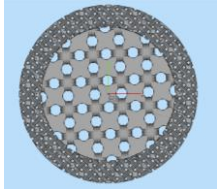
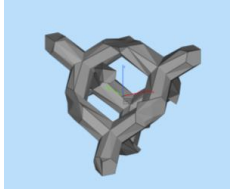
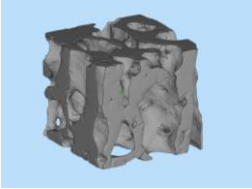
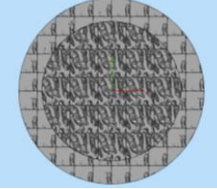
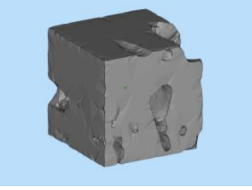


Figure 4.34– Surface view, regular and natural NiTi trabecular scaffolds (a) S_{F1} , (b) $S_{F1.5}$, (c) $S_{T1.5}$ (Table 4.12).

In a similar way, graded porous structures with two separate layers were designed (inner sub-structure has a diameter of 3.75 mm and outer sub-structure has a diameter of 5 mm). The cylindrical samples were generated by the replication of two different unitcells for inner and outer parts. As can be seen in Table 4.13, S_{reg1} has been designed by replication of regular FEM and diamond unitcells for inner and outer layers respectively. In the same way, S_{nat1} has been designed by replication of natural Trabecular and Cortical unitcells for inner and outer layers respectively. As presented in experiment design in Table 4.11, HP parameters were used for internal scan lines and MP parameters were used for boarder scan lines to increase the productivity. Using lower laser power for scanning the boarders, inhibits the melting of excess powders and decrease the dimensional deviation of product to the predesigned model. Figure 4.35 illustrates the surface view of two different NiTi gradient scaffolds produced from natural and regular unitcells applying the new strategy developed in this thesis.

Table 4.13– NiTi functionally porous scaffolds (natural and regular)

Sample	Part parameter Internal- Border	Unitcell	Scaffold (top)
S _{reg1}	HP-MP	 Inner: FEM, 1.5 mm	 Do: 5 mm Di: 3.75 mm to/ti= 0.25
		 Outer: Diamond, 1.5 mm	
S _{nat1}	HP-MP	 Inner: Trab 1.5, 1.5 mm	 Do: 5 mm Di: 3.75 mm to/ti= 0.25
		 Outer: Cortical 1, 1 mm	

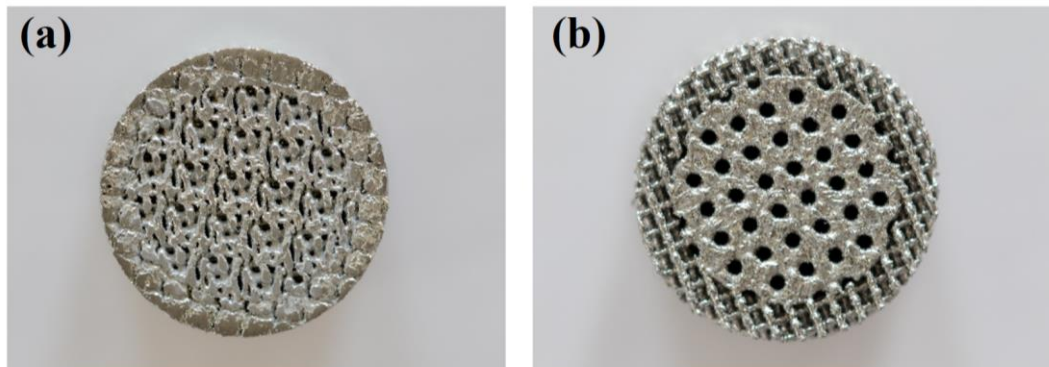


Figure 4.35– (a) S_{nat1} , (b) S_{art1} (Table 4.13)

4.4 Summary and conclusion (SLM of NiTi)

Selective laser melting of atomized $Ni_{50.8}Ti_{49.2}$ powder with a new set of process parameters was done in this research aiming to evaluation of SLM process as a micro additive manufacturing method.

Using small spot laser diameter ($30\ \mu m$), decreases the dimension of melt pool and consequently leads to severer rapid solidification. Also, high laser power increases the temperature of melting pool and causes to grain coarsening. XRD analysis depicts that using high laser power in SLM of NiTi produces a single phase B2 austenite containing sharp peaks which can be attributed to highly crystalline and coarse grain structure. Comparison of XRD patterns of low and medium laser power samples revealed that broadening and decrease in peak heights has happened due to rapid solidification which encourages very fine-grained microstructure and high level of micro strain.

Three different regimes of process parameters have been successfully developed in this research to obtain the single phase B2 Austenite phase after SLM of $Ni_{50.8}Ti_{49.2}$ powder. These regimes of process parameters can be utilized for boarder and internal parts of SLM NiTi samples with complicated geometries and micro features. Using combination of MP and HP parameters for boarder and internal area in SLM process enhances productivity preserving the desired phase composition. Surface topography measurements conducted by focus variation microscopy revealed that the laser power is the most determinant factor in surface topography

of SLM NiTi samples. Optimized SLM process parameters (P=150 W, V= 1100 mm/sec) led to the minimum porosity and surface roughness of 0.02% and 10 μm respectively.

Chapter 5 General conclusions

Many manufacturing techniques have been developed up to now to respond the demand for 3D microfabrication. Current techniques have some limitations for production of complicated geometries and new methods should be developed to address this issue. The AM processes have been identified as a progressive and effective 3D microfabrication technology. This thesis presented two main laser based metal additive manufacturing techniques for microfabrication of porous scaffolds in biomedical application.

Synthesis of NiTi single phase from the elemental powder mixtures using high energy mechanical alloying and μ DMD process was done in this research. Results showed that using high energy milled Ni_{50.8}Ti_{49.2} powder, the scanning speed in the μ DMD process can be increased up to 3 times without any change of the phase composition. In this thesis, μ DMD process was developed for fabrication of NiTi hollow materials with micro features. Dimensional accuracy of micro features in μ DMD processed parts with respect to nominal geometrical models was calculated higher than dimensional accuracy of SLM products (as reported from literature).

Selective laser melting of atomized prealloyed Ni_{50.8}Ti_{49.2} powder with new sets of process parameters was done in this research aiming to evaluation of SLM process as a microfabrication method. XRD analysis depicts that using high laser power in SLM of NiTi produces a single phase B2 austenite containing sharp peaks which can be attributed to highly crystalline and coarse grain structure. Three different regimes of process parameters have been successfully developed in this research to obtain the single phase B2 Austenite phase after SLM of Ni_{50.8}Ti_{49.2} powder. These regimes of process parameters were successfully utilized to fabricate NiTi porous scaffolds with complicated geometries and micro features based on the internal architecture of real human bone.

References

- [1] M. Vaezi, H. Seitz, and S. Yang, “A review on 3D micro-additive manufacturing technologies,” *Int. J. Adv. Manuf. Technol.*, vol. 67, pp. 1721–1754, 2013.
- [2] B. Ghosh, Amitabha, Corves, “Introduction to Micromechanisms and Microactuators,” 1st ed., Springer International Publishing, 2015.
- [3] Y. Qin, *Overview of micro-manufacturing*, 2nd ed. Elsevier, 2010.
- [4] B. Zhang, H. Liao, and C. Coddet, “Effects of processing parameters on properties of selective laser melting Mg–9%Al powder mixture,” *Mater. Des.*, vol. 34, pp. 753–758, 2012.
- [5] B. Zhang, J. Chen, and C. Coddet, “Microstructure and transformation behavior of in-situ shape memory alloys by selective laser melting Ti-Ni mixed powder,” *J. Mater. Sci. Technol.*, vol. 29, pp. 863–867, 2013.
- [6] I. Shishkovsky, Y. Morozov, and I. Smurov, “Nanofractal surface structure under laser sintering of titanium and nitinol for bone tissue engineering,” *Appl. Surf. Sci.*, vol. 254, pp. 1145–1149, 2007.
- [7] M. Gharbi *et al.*, “Influence of various process conditions on surface finishes induced by the direct metal deposition laser technique on a Ti-6Al-4V alloy,” *J. Mater. Process. Technol.*, vol. 213, pp. 791–800, 2013.
- [8] B. V. Krishna, S. Bose, and A. Bandyopadhyay, “Fabrication of porous NiTi shape memory alloy structures using laser engineered net shaping,” *J. Biomed. Mater. Res. - Part B Appl. Biomater.*, vol. 89, pp. 481–490, 2009.
- [9] L. Erica, “Studio e ottimizzazione del processo di fabbricazione additiva (SLM) per applicazioni in ambito biomedicale: produzione di protesi e strutture reticolari,” Università di Bologna, 2017.

- [10] A. C. Ankur Jain, "Ultra-Precision Metal Additive Manufacturing for Thermal Management of Microelectronics," 2015.
- [11] J. Laeng, J. G. Stewart, and F. W. Liou, "Laser metal forming processes for rapid prototyping - a review," *INT. J. PROD. RES.*, vol. 38, pp. 3973–3996, 2000.
- [12] Y. Huang, M. B. Khamesee, and E. Toyserkani, "A comprehensive analytical model for laser powder-fed additive manufacturing," *Addit. Manuf.*, vol. 12, pp. 90–99, 2016.
- [13] S. Khademzadeh, N. Parvin, P. F. Bariani, and F. Mazzucato, "Effects of micro laser sintering process parameters on quality of nickel-titanium single tracks and thin walls," *Met. Mater. Int.*, vol. 21, no. 6, 2015.
- [14] G. Bi, A. Gasser, K. Wissenbach, A. Drenker, and R. Poprawe, "Investigation on the direct laser metallic powder deposition process via temperature measurement," *Appl. Surf. Sci.*, vol. 253, no. 3, pp. 1411–1416, 2006.
- [15] A. J. Pinkerton and L. Li, "The significance of deposition point standoff variations in multiple-layer coaxial laser cladding (coaxial cladding standoff effects)," *Int. J. Mach. Tools Manuf.*, vol. 44, no. 6, pp. 573–584, 2004.
- [16] L. Li and J. Liu, "Effects of process variables on laser direct formation of thin wall," *Opt. Laser Technol.*, vol. 39, no. 2, pp. 231–236, 2007.
- [17] G. Zhu, D. Li, A. Zhang, G. Pi, and Y. Tang, "The influence of laser and powder defocusing characteristics on the surface quality in laser direct metal deposition," *Opt. Laser Technol.*, vol. 44, pp. 349–356, 2012.
- [18] P. L. Blackwell, "The mechanical and microstructural characteristics of laser-deposited IN718," *J. Mater. Process. Technol.*, vol. 170, no. 1–2, pp. 240–246, 2005.
- [19] I. Taberero, A. Lamikiz, S. Martínez, E. Ukar, and J. Figueras, "Evaluation of the mechanical properties of Inconel 718 components built by laser cladding," *Int. J. Mach. Tools Manuf.*, vol. 51, no. 6, pp. 465–470, 2011.
- [20] W. Li *et al.*, "Effect of laser scanning speed on a Ti-45Al-2Cr-5Nb alloy processed by selective laser melting: Microstructure, phase and mechanical properties," *J. Alloys*

- Compd.*, vol. 688, pp. 626–636, 2016.
- [21] G. P. Dinda, A. K. Dasgupta, and J. Mazumder, “Texture control during laser deposition of nickel-based superalloy,” *Scr. Mater.*, vol. 67, pp. 503–506, 2012.
- [22] S. Zhang, Q. Wei, L. Cheng, S. Li, and Y. Shi, “Effects of scan line spacing on pore characteristics and mechanical properties of porous Ti6Al4V implants fabricated by selective laser melting,” *Mater. Des.*, vol. 63, pp. 185–193, 2014.
- [23] D. A. Hollander *et al.*, “Structural, mechanical and in vitro characterization of individually structured Ti-6Al-4V produced by direct laser forming,” *Biomaterials*, vol. 27, pp. 955–963, 2006.
- [24] ASM Handbook Committee. ASM Handbook, “Powder Metal Technologies and Applications. s.l.,” 1998.
- [25] A. Bansiddhi, T. D. Sargeant, S. I. Stupp, and D. C. Dunand, “Porous NiTi for bone implants: A review,” *Acta Biomater.*, vol. 4, p. 773, 2008.
- [26] W. J. Buehler and F. E. Wang, “A summary of recent research on the Nitinol alloys and their potential application in ocean engineering,” *Ocean Eng.*, vol. 1(1), pp. 105–120, 1968.
- [27] Y. Liu, Z. Xie, and J. Van Humbeeck, “Cyclic deformation of NiTi shape memory alloys,” *Mater. Sci. Eng. A*, vol. 273–275, pp. 673–678, 1999.
- [28] S. Nemat-Nasser and W. G. Guo, “Superelastic and cyclic response of NiTi SMA at various strain rates and temperatures,” *Mech. Mater.*, vol. 38, pp. 463–474, 2006.
- [29] A. Kapanen, J. Ilvesaro, A. Danilov, J. Ryhänen, P. Lehenkari, and J. Tuukkanen, “Behaviour of Nitinol in osteoblast-like ROS-17 cell cultures,” *Biomaterials*, vol. 23, pp. 645–650, 2002.
- [30] K. Otsuka and C. M. Wayman, *Shape memory materials*, 1st ed. Cambridge University Press, 1998.
- [31] Dieter and Stoeckel, “The Shape Memory Effect - Phenomenon, Alloys and

- Applications,” in *Shape Memory Alloys for Power Systems EPRI*, 1995, pp. 1–13.
- [32] S. Saedi, “Shape Memory Behavior of Dense and Porous NiTi Alloys Fabricated by Selective Laser Melting,” University of Kentucky, 2017.
- [33] K. Weinert and V. Petzoldt, “Machining of NiTi based shape memory alloys,” *Mater. Sci. Eng. A*, vol. 378, no. 1, pp. 180–184, 2004.
- [34] M. H. Elahinia, M. Hashemi, M. Tabesh, and S. B. Bhaduri, “Manufacturing and processing of NiTi implants: A review,” *Prog. Mater. Sci.*, vol. 57, no. 5, 2012.
- [35] Ming H. Wu, “Fabrication of Nitinol Materials and Components,” in *Proceedings of the International Conference on Shape Memory and Superelastic Technologies*, 2001, pp. 285–292.
- [36] S. K. Wu, H. C. Lin, and C. C. Chen, “A study on the machinability of a Ti49.6Ni50.4 shape memory alloy,” *Mater. Lett.*, vol. 40, pp. 27–32, 1999.
- [37] D. S. Grummon, J. A. Shaw, and A. Gremillet, “Low-density open-cell foams in the NiTi system,” *Appl. Phys. Lett.*, vol. 82, pp. 2727–2729, 2003.
- [38] G. Tosun, L. Ozler, M. Kaya, and N. Orhan, “A study on microstructure and porosity of NiTi alloy implants produced by SHS,” *J. Alloys Compd.*, vol. 487, pp. 605–611, 2009.
- [39] T. Bormann, R. Schumacher, B. Müller, and M. de Wild, “Fabricating niTi shape memory scaffolds by selective laser melting,” *Eur. Cells Mater.*, vol. 22, p. 12, 2011.
- [40] I. Shishkovsky, I. Yadroitsev, and I. Smurov, “Direct Selective Laser Melting of Nitinol Powder,” *Phys. Procedia*, vol. 39, p. 447, 2012.
- [41] T. Mousavi, F. Karimzadeh, and M. H. Abbasi, “Synthesis and characterization of nanocrystalline NiTi intermetallic by mechanical alloying,” *Mater. Sci. Eng. A*, vol. 487, pp. 46–51, 2008.
- [42] S. Saedi, A. Sadi, M. Taheri, C. Haberland, H. Karaca, and M. Elahinia, “The influence of heat treatment on the thermomechanical response of Ni-rich NiTi alloys manufactured by selective laser melting,” *J. Alloys Compd.*, vol. 677, pp. 204–210,

2016.

- [43] S. Saedi, A. S. Turabi, M. T. Andani, C. Haberland, M. Elahinia, and H. Karaca, “Thermomechanical characterization of Ni-rich NiTi fabricated by selective laser melting,” *Smart Mater. Struct.*, vol. 25, pp. 35–43, 2016.
- [44] P. R. Halani, I. Kaya, Y. C. Shin, and H. E. Karaca, “Phase transformation characteristics and mechanical characterization of nitinol synthesized by laser direct deposition,” *Mater. Sci. Eng. A*, vol. 559, p. 836, 2013.
- [45] Q. Wang, Q. Wang, and C. Wan, “Preparation and evaluation of a biomimetic scaffold with porosity gradients in vitro,” *An. Acad. Bras. Cienc.*, vol. 84, pp. 9–16, 2012.
- [46] B. Zhang *et al.*, “The biomimetic design and 3D printing of customized mechanical properties porous Ti6Al4V scaffold for load-bearing bone reconstruction,” *Mater. Des.*, vol. 152, pp. 30–39, 2018.
- [47] M. Taheri, S. Saedi, A. Sadi, and M. R. Karamooz, “Mechanical and shape memory properties of porous Ni50.1Ti49.9 alloys manufactured by selective laser melting,” *J. Mech. Behav. Biomed. Mater.*, vol. 68, no. January, pp. 224–231, 2017.
- [48] A. P. Rubshtein *et al.*, “Porous material based on spongy titanium granules: Structure, mechanical properties, and osseointegration,” *Mater. Sci. Eng. C*, vol. 35, pp. 363–369, 2014.
- [49] S. Bose, M. Roy, and A. Bandyopadhyay, “Recent advances in bone tissue engineering scaffolds,” *Trends Biotechnol.*, vol. 30, no. 10, pp. 546–554, 2012.
- [50] G. Ryan, A. Pandit, and D. P. Apatsidis, “Fabrication methods of porous metals for use in orthopaedic applications,” *Biomaterials*, vol. 27, no. 13, pp. 2651–2670, 2006.
- [51] T. B. Sercombe *et al.*, “Failure modes in high strength and stiffness to weight scaffolds produced by Selective Laser Melting,” *Mater. Des.*, vol. 67, pp. 501–508, 2015.
- [52] Y. J. Liu, X. P. Li, L. C. Zhang, and T. B. Sercombe, “Processing and properties of topologically optimised biomedical Ti–24Nb–4Zr–8Sn scaffolds manufactured by

- selective laser melting,” *Mater. Sci. Eng. A*, vol. 642, pp. 268–278, 2015.
- [53] M. N. Ahsan, C. P. Paul, L. Kukreja, and A. J. Pinkerton, “Porous structures fabrication by continuous and pulsed laser metal deposition for biomedical applications; modelling and experimental investigation,” *J. Mater. Process. Technol.*, vol. 211, pp. 602–609, 2011.
- [54] T.-M. G. Chu, D. G. Orton, S. J. Hollister, S. E. Feinberg, and J. W. Halloran, “Mechanical and in vivo performance of hydroxyapatite implants with controlled architectures,” *Biomaterials*, vol. 23, no. 5, pp. 1283–1293, 2002.
- [55] A. Mikos, G. Sarakinos, M. Lyman, D. Ingber, J. Vacanti, and R. Langer, “Prevascularization of porous biodegradable polymers,” *Biotechnol. Bioeng.*, vol. 42, no. 6, pp. 716–723, 1993.
- [56] S. J. Simske, R. A. Ayers, and T. Bateman, “Porous materials for bone engineering,” *Mater. Sci. Forum*, vol. 250, pp. 151–182, 1997.
- [57] J. Wieding, A. Jonitz, and R. Bader, “The effect of structural design on mechanical properties and cellular response of additive manufactured titanium scaffolds,” *Materials (Basel)*, vol. 5, p. 1336, 2012.
- [58] S. Amin Yavari *et al.*, “Fatigue behavior of porous biomaterials manufactured using selective laser melting,” *Mater. Sci. Eng. C*, vol. 33, p. 4849, 2013.
- [59] V. I. Itin, V. E. Gyunter, S. A. Shabalovskaya, and R. L. C. Sachdeva, “Mechanical properties and shape memory of porous nitinol,” *Mater. Charact.*, vol. 32, p. 179, 1994.
- [60] T. Habijan *et al.*, “The biocompatibility of dense and porous Nickel-Titanium produced by selective laser melting,” *Mater. Sci. Eng. C*, vol. 33, p. 419, 2013.
- [61] S. Carmignato, “Accuracy of industrial computed tomography measurements: Experimental results from an international comparison,” *CIRP Ann. - Manuf. Technol.*, vol. 61, p. 491–494., 2012.
- [62] A. Thompson, N. Senin, C. Giusca, and R. Leach, “Topography of selectively laser

- melted surfaces: A comparison of different measurement methods,” *CIRP Ann. - Manuf. Technol.*, vol. 66, pp. 543–546, 2017.
- [63] ISO 4288:1996 Geometrical Product Specifications (GPS), “Surface texture: Profile method-Rules and procedures for the assessment of surface texture (ISO 4288: 1996),” in *German version EN ISO*, 1997.
- [64] S. Khademzadeh, N. Parvin, and P. F. Bariani, “Production of NiTi alloy by direct metal deposition of mechanically alloyed powder mixtures,” *Int. J. Precis. Eng. Manuf.*, vol. 16, no. 11, 2015.
- [65] Z. Wang *et al.*, “Analysis of factors influencing bone ingrowth into three-dimensional printed porous metal scaffolds: A review,” *J. Alloys Compd.*, vol. 717, pp. 271–285, 2017.
- [66] L. De Chiffre, S. Carmignato, J. P. Kruth, R. Schmitt, and A. Weckenmann, “Industrial applications of computed tomography,” *CIRP Ann. - Manuf. Technol.*, vol. 63, no. 2, pp. 655–677, 2014.
- [67] P. Hermanek and S. Carmignato, “Porosity measurements by X-ray computed tomography: Accuracy evaluation using a calibrated object,” *Precis. Eng.*, vol. 49, pp. 377–387, 2017.
- [68] Z. L. Lu, D. C. Li, B. H. Lu, A. F. Zhang, G. X. Zhu, and G. Pi, “The prediction of the building precision in the Laser Engineered Net Shaping process using advanced networks,” *Opt. Lasers Eng.*, vol. 48, p. 519, 2010.
- [69] Federico Mazzucato, “Additive manufacturing through micro direct laser metal deposition technology: influence of the material and process parameters on the product quality,” University of Padova, 2016.
- [70] Z. L. Lu *et al.*, “Investigation into the direct laser forming process of steam turbine blade,” *Opt. Lasers Eng.*, vol. 49, pp. 1101–1110, 2011.
- [71] X. He, P. W. Fuerschbach, and T. DebRoy, “Heat transfer and fluid flow during laser spot welding of 304 stainless steel,” *J. Phys. D. Appl. Phys.*, vol. 36, no. 12, 2003.

- [72] C. Suryanarayana, "Mechanical alloying and milling," *Prog. Mater. Sci.*, vol. 46, pp. 1–184, 2001.
- [73] ASM International, *ASM Handbook, Volume 3, Alloy Phase Diagrams*. 2004.
- [74] L. Peng *et al.*, "Direct laser fabrication of nickel alloy samples," *Int. J. Mach. Tools Manuf.*, vol. 45, pp. 1288–1294, 2005.
- [75] I. V Shishkovskii, I. A. Yadroitsev, and I. Y. Smurov, "Selective laser sintering/melting of nitinol–hydroxyapatite composite for medical applications," *Powder Metall. Met. Ceram.*, vol. 50, no. 5, pp. 275–283, 2011.
- [76] H. Meier and C. Haberland, "Experimental studies on selective laser melting of metallic parts," *Materwiss. Werksttech.*, vol. 39, no. 9, pp. 665–670, 2008.
- [77] V. Karageorgiou and D. Kaplan, "Porosity of 3D biomaterial scaffolds and osteogenesis," *Biomaterials*, vol. 26, no. 27, pp. 5474–91, 2005.
- [78] L. Sexton, S. Lavin, G. Byrne, and A. Kennedy, "Laser cladding of aerospace materials," *J. Mater. Process. Technol.*, vol. 122, pp. 63–68, 2002.
- [79] L. L. Parimi, G. Ravi, D. Clark, and M. M. Attallah, "Microstructural and texture development in direct laser fabricated IN718," *Mater. Charact.*, vol. 89, pp. 102–111, 2014.
- [80] W. Hofmeister, M. Griffith, M. Ensz, and J. Smugeresky, "Solidification in direct metal deposition by LENS processing," *J. Miner. Met. Mater. Soc.*, vol. 53, no. 9, 2001.
- [81] A. Rollett, F. Humphreys, G. S. Rohrer, and M. Hatherly, *Recrystallization and Related Annealing Phenomena: Second Edition*. 2004.
- [82] L. Thijs, F. Verhaeghe, T. Craeghs, J. Van Humbeeck, and J. P. Kruth, "A study of the microstructural evolution during selective laser melting of Ti-6Al-4V," *Acta Mater.*, vol. 58, no. 9, pp. 3303–3312, 2010.
- [83] A. Townsend, L. Pagani, P. Scott, and L. Blunt, "Areal surface texture data extraction from X-ray computed tomography reconstructions of metal additively manufactured

- parts,” *Precis. Eng.*, vol. 48, pp. 254–264, 2017.
- [84] I. 25178-2, *Geometrical product specifications (gps)-surface texture: areal-part 2: terms, definitions and surface texture parameters*,. 2012.
- [85] J. Robinson, “Determination of the effect of scan strategy on residual stress in laser powder bed fusion additive manufacturing,” *Addit. Manuf.*, vol. 23, pp. 13–24, 2018.
- [86] M. Speirs *et al.*, “On the Transformation Behavior of NiTi Shape-Memory Alloy Produced by SLM,” *Shape Mem. Superelasticity*, vol. 2, no. 4, pp. 310–316, 2016.
- [87] S. Dadbakhsh, M. Speirs, J. P. Kruth, and J. Van Humbeeck, “Influence of SLM on shape memory and compression behaviour of NiTi scaffolds,” *CIRP Ann. - Manuf. Technol.*, vol. 64, no. 1, pp. 209–212, 2015.
- [88] D. Schryvers, W. Tirry, and Z. Q. Yang, “Measuring strain fields and concentration gradients around Ni₄Ti₃ precipitates,” *Mater. Sci. Eng. A*, vol. 438–440, pp. 485–488, 2006.
- [89] A. Ahadi and Q. Sun, “Effects of grain size on the rate-dependent thermomechanical responses of nanostructured superelastic NiTi,” *Acta Mater.*, vol. 76, pp. 186–197, 2014.
- [90] F. Zanini, L. Pagani, P. J. Scott, E. Savio, and S. Carmignato, “Measurement of additively manufactured surfaces with re-entrant features by X-ray computed tomography,” in *ASPE and euspen Summer Topical Meeting: Advancing precision in additive manufacturing*, 2018.
- [91] S. Carmignato, W. Dewulf, and R. Leach, *Industrial X-ray computed tomography*. 2017.
- [92] S. P. J. Pagani L, Zanini F, Carmignato S, Jiang X, “Generalization of profile texture parameters for additively manufactured surfaces,” in *XXII IMEKO World Congress, Belfast (UK)*, 2018.
- [93] C.-C. Shih, C.-M. Shih, Y.-Y. Su, L. H. J. Su, M.-S. Chang, and S.-J. Lin, “Effect of

- surface oxide properties on corrosion resistance of 316L stainless steel for biomedical applications,” *Corros. Sci.*, vol. 46, no. 2, pp. 427–441, 2004.
- [94] A. Saboori, D. Gallo, S. Biamino, P. Fino, and M. Lombardi, “An Overview of Additive Manufacturing of Titanium Components by Directed Energy Deposition: Microstructure and Mechanical Properties,” *Appl. Sci.*, vol. 7, no. 9, p. 883, 2017.
- [95] T. D. H. L. Wei, T. Mukherjee, “Grain Growth Modeling For Additive Manufacturing Of Nickel Based Superalloys,” in *6th International Conference on Recrystallization And Grain Growth*, 2016, pp. 265–269.
- [96] L. T. Wilkerson, “Finite element analysis of cancellous bone,” University of Kentucky, 2012.
- [97] P. Zioupos, J. Currey, “Changes in the Stiffness, Strength, and Toughness of Human Cortical Bone With Age,” *Bone*, vol. 22, pp. 57–66, 1998.
- [98] M. Rafiei, S. Khademzadeh, and N. Parvin, “Characterization and formation mechanism of nanocrystalline W-Al alloy prepared by mechanical alloying,” *J. Alloys Compd.*, vol. 489, no. 1, 2010.
- [99] M. A. Surmeneva *et al.*, “Fabrication of multiple-layered gradient cellular metal scaffold via electron beam melting for segmental bone reconstruction,” *Mater. Des.*, vol. 133, pp. 195–204, 2017.
- [100] H. W. S.M. Ahmadi, G. Campoli, S.A. Yavari, B. Sajadi, R. Wauthlé, J. Schrooten and A.A. Zadpoor, “Mechanical behavior of regular open-cell porous biomaterials made of diamond lattice unit cells,” *J. Mech. Behav. Biomed. Mater.*, vol. 34, pp. 106–115, 2014.
- [101] F.J. Quevedo González, N. Nuño, “Finite element modelling approaches for well-ordered porous metallic materials for orthopedic applications: cost effectiveness and geometrical considerations,” *Comput. Methods Biomech. Biomed. Engin.*, vol. 19, no. 8, pp. 845–854, 2016.

Appendix A Governing equations of powder and gas motion in μ DMD process

A.1 Carrier gas equations

The governing equations and related finite element simulation was done in Te.Si laboratory [69]. The governing equations for the Argon carrier gas were described in a Eulerian reference frame. The primary continuous phase was modelled on the Navier- Stokes equations, where the averaging time-dependent Reynolds method in combination with the standard k- ϵ turbulent model was used to modify the governing equations for the laminar flow. To describe a turbulent flow, the time-averaging governing equations are:

Conservation of mass:

$$\frac{\partial}{\partial x_i} (\rho u_i) = 0 \quad (\text{A.1})$$

where ρ is the Argon density (1.623 kg/m³), u_i the gas velocity and x_i the gas position.

Conservation of momentum:

$$\frac{\partial}{\partial x_i} (\rho u_i u_j) = -\frac{\partial p}{\partial x_i} + \frac{\partial \tau_{ij}}{\partial x_j} + \rho g_i \quad (\text{A.2})$$

Where p is the pressure, g is the gravitational acceleration and τ_{ij} is the viscous stress tensor defined by:

$$\tau_{ij} = \left[(\mu + \mu_t) \left(\frac{\partial u_i}{\partial x_j} + \frac{\partial u_j}{\partial x_i} \right) \right] - \frac{2}{3} \mu_t \frac{\partial u_i}{\partial x_i} \delta_{ij} \quad (\text{A.3})$$

where μ is the molecular viscosity ($2.125 \times 10^{-5} \text{ kg/(m.s)}$) and δ_{ij} is the Kronecker delta (δ_{ij} is equal to 1 for $i=j$, otherwise δ_{ij} is equal to 0). μ_t is the turbulent viscosity defined by:

$$\mu_t = \rho C_\mu \frac{k^2}{\varepsilon} \quad (\text{5A.4})$$

Where C_μ was a constant and usually considered equal to 0.09, k the kinetic energy of turbulence, and ε the dissipation of kinetic energy of turbulence, which is defined in the k - ε turbulence model. Moreover, two more extra equations were required to solve the mass and momentum conservation equations in a time average manner. The most commonly used model to handle this situation was the standard k - ε model in which the k and ε represented the turbulent kinetic energy and dissipation of kinetic energy respectively. The conservation of kinetic energy of turbulence was given by:

$$\frac{\partial}{\partial x_i} (\rho k u_i) = \frac{\partial}{\partial x_j} \left[\left(\mu + \frac{\mu_t}{\sigma_k} \right) \frac{\partial k}{\partial x_j} \right] + G_k + G_b - \rho \varepsilon \quad (\text{A.5})$$

whereas the conservation of dissipation of kinetic energy of turbulence was defined as:

$$\frac{\partial}{\partial x_i} (\rho \varepsilon u_i) = \frac{\partial}{\partial x_j} \left[\left(\mu + \frac{\mu_t}{\sigma_\varepsilon} \right) \frac{\partial \varepsilon}{\partial x_j} \right] + C_{1\varepsilon} \frac{\varepsilon}{k} (G_k + G_b) - C_{2\varepsilon} \rho \frac{\varepsilon^2}{k} \quad (\text{A.6})$$

$$G_k = \mu_t \left(\frac{\partial u_j}{\partial x_i} + \frac{\partial u_i}{\partial x_j} \right) \frac{\partial u_i}{\partial x_j} \quad (\text{A.7})$$

$$G_b = -g_i \frac{\mu_t}{\rho Pr_t} \frac{\partial \rho}{\partial x_i} \quad (\text{A.8})$$

where $C_{1\varepsilon}=1.44$, $C_{2\varepsilon}=1.92$, $k=1.0$ and $\varepsilon=1.3$ are empirical constants, Pr_t is the turbulent Prandtl number, G_k is the generation of turbulence kinetic energy due to the mean velocity gradients, and G_b is the generator of turbulence kinetic energy due to buoyancy. The equations provided above governed the continuous phase constituted by the Argon carrier gas. To complete the theoretical basis of this CFD analysis, the equations governing the secondary phase were discussed in the following.

A.2 Modelling of powder particles

The behaviour of the discrete phase (powder particles) was computed by integrating the force balance for each particle in the Lagrangian reference frame. Along the x direction, the balance of the forces was given by:

$$\frac{du_p}{dt} = F_D(u - u_p) - g_x \left(\frac{\rho_p - \rho}{\rho_p} \right) + F_x \quad (\text{A.9})$$

where u_p was the particle velocity, u was the fluid phase velocity, ρ was the fluid density, ρ_p was the density of the particles, g_x was the x component of the gravitational acceleration, and F_x was an additional acceleration (force/unit particle mass) term. F_D coefficient was the drag force per powder mass unit and it could be calculated as:

$$F_D = \frac{18\mu}{\rho_p d_p^2} \frac{C_D Re}{24} \quad (\text{A.10})$$

In the equation defining F_D , μ is the molecular viscosity of the fluid, d_p is the particle diameter, Re is the relative Reynolds number, and C_D is the drag coefficient defined as:

$$Re = \frac{\rho d_p |u_p - u|}{\mu} \quad (\text{A.11})$$

$$C_D = a_1 + \frac{a_2}{Re} + \frac{a_3}{Re^2} \quad (\text{A.12})$$

Where a_1 , a_2 , and a_3 are empirical constants. The second term on the right of Eq. (A.10) consisted of the gravity and buoyancy forces per unit particle mass. A discrete random walk model is used to consider turbulence fluctuations of the flow. The turbulence is modelled by eddies defined by a Gaussian distributed random velocity fluctuation u' , v' , w' in the equation Eq. (A.14) and a time scale T_L in Eq. (A.15). ζ is a normally distributed random number used for the three directions because of the hypothesis of isotropic turbulence, and C_L is the time scale constant.

$$u' = v' = w' = \zeta \sqrt{\frac{2k}{3}} \quad (\text{A.13})$$

$$T_L = 2C_L \frac{k}{\varepsilon} \quad (\text{A.14})$$

The particle vortex crossing time (t_{cross}) is defined as:

$$t_{cross} = -\tau \ln\left[1 - \left(\frac{L_e}{\tau|u - u_p|}\right)\right] \quad (\text{A.15})$$

Where τ is the particle relaxation time, L_e is the vortex length scale, and $u - u_p$ is the magnitude of the relative velocity. The particle is assumed to interact with the fluid phase vortex over the smaller of the vortex life and crossing times. When this time is reached, a new value of instantaneous velocity is obtained by applying a new value of ζ in Eq. (A.14). The main parameter of this discrete random walk model is the time scale constant C_L . Its recommended value was 0.15 for the k - ε turbulence model by making a link between the eddy lifetime, T_L and the integral time scale, T , defined as:

$$T = \int_0^{\infty} \frac{u_p(t)u_p(t+s)}{u_p^2} ds \quad (\text{A.16})$$

The equations provided above governed the discrete phase constituted by powder particles. Before starting with the CFD simulation and numerical result analysis the boundary conditions and model assumption concerning the deposition process had to be introduced and explained.

Appendix B G-codes, laser focus position

```
(Find laser Foccus)
Definizione variabili)
P1300=16.0 (16 Potenza laser)
P1301=-8 (X start) (-8, -4, 0, 4, 8,)
P1302=1 (Y start) (5, 1, -3, -7)
P1303=+0.2 (Y space)
P1304=-1.5 (Z start)
P1305=+1.5 (Z stop)
P1306=+0.2 (scan Z step)
P1307=+3.0 (x length)
P1308=0 (Y tmp)
P1309=0 (Z tmp)
(Coordinata di Y corrisponente a Z centrale)
(:P1310= P1302 + P1303*(((P1305+P1304)/2)-P1304)/P1306
(Coordinata di Y corrisponente a Z=0)
: P1310= P1302 + P1303*(0-P1304)/P1306
G17 (XY level)
G1 F1000 (speed)
G90 (Impostazioni di quote absolute)
G60 X0 (Look ahead on)
G22 L8011 (Close Box)
M124 (on 220V KA5 Chiller)
M100 (on pompa chiller)
G253 F="WAITING TO START..... (Press START when the machine will be
ready)"
M0
G22 L8017 (Bnc ON)
G61
P1230=P1300
(G4 X1.0 (wait 1 secondi))
G60 X0 (Look ahead on)
S2
G54 X0 Y0 Z2
G0 X+0 Y+0 Z+0 F2000
P1308 = P1302
P1309 = P1304
(Linee orizzontali a distanze crescenti)
N10
G0 X=P1301 Y=P1308 Z=P1309
Q0=1 (laser ON)
: P1400= P1301+P1307
G1 X=P1400 F200
Q0=0 laser OFF)
: P1308= P1308+P1303
: P1309= P1309+P1306
G0 Y=P1308 Z=P1309
Q0=1 (laser ON)
: P1400= P1301-0.4
```

```
G1 X=P1400 F200
Q0=0 (laser OFF)
: P1308= P1308+P1303
: P1309= P1309+P1306
P1311=0
: P1311= SIGN (P1305-P1309) +1
G20 X10 E=P1311
(Segno di zero)
G61
P1230=18.0 (laser power)
G4 X1.0 (wait 1 secondi))
G60 X0 (Look ahead on)
: P1400= P1301+P1307
G0 X=P1400 Y=P1302 Z=P1304
Q0=1 (laser ON)
: P1400= P1301-0.4
G1 X=P1400 Y=P1310 Z+0
: P1400= P1301+P1307
X=P1400 Y=P1308 Z=P1309
Q0=0 (laser OFF)
G22 L8018 (Bnc OFF)
G22 L8016 (Stop)
G22 L8010 (Open Box))
(G22 L8021 (Measure)
```


Appendix C G-codes, single tracks

```
(Single tracks)
G17 (XY level)
G1 F3000 (speed)
G60 X0 (Look ahead on)
G90 (Absolute dimensions)
G4 X0.3 (wait 0.3 seconds to read zero)
(Initialization process)
G22 L8011 (Close Box)
(Powder feeder ON)
P1509 = 15 (speed [0.1 um/s] - Velocita' Asta)
P1508 = 7 (gas [0.1 l/min] - Flusso di Ar)
P1507 = 600 (rpm [RPM] - Giri spazzola)
P1506 = 3 (powder type - Geom. usato)
G22 L8025 (Powder Feeder 1 ON)
G22 L8015 (Start)
(Laser initialization)
G22 L8017 (Bnc ON)
(ripetizione1)
S2 (Laser Position)
G53 S2 (Laser working)
G54 X-0.4 Y-0.6 Z0 (X5.1 Y-6.1 Z0)
G0 X0 Y0 Z0
(Start working)
P1230=30 (laser power 30.0W)
G0 X-7 Y0.15 Z-0.7 F3000 (1)
G61
Q0=1 (laser ON)
G1 X-7 Y0.15 Z-0.7 F20
G1 X-7 Y-1.35 Z-0.7 F20
G1 X-7 Y0.15 Z-0.7 F20
Q0=0 (laser OFF)
G22 L8020 (Fast cleaning)
S2 (Laser position)
M113
G4 X3
G53 S2
G1 F50
(* ZLAYERCOMPLETE #1)
P1230=0 (laser power 0.0W)
Q0=0 (laser OFF)
(Pre-heating OFF)
P1510 = 10 (heater_temp) (Temperatura di preriscaldamento)
G22 L8026 (Powder Feeder 1 OFF)
G4 X3
(* Tail code)
(G22 L8021 (Measure)
G22 L8018 (LASER OFF)
G22 L8016 (Stop Operation)
```


G22 L8010 (Open Box)
M30 (end program)
(cilindro.DIN)

Appendix D G-codes, thin walls

```
(Thin walls)
(Definizione variabili)
P1300=30 (Potenza laser)
P1301=100 (velocita' mm/min)
P1400=2      (X start)
P1401=-10   (Y start)
P1404=0      (Z start)
P1405=0.005 (scan Z step) (thickness of layers)
P1406=2      (Z stop)
P1407=0      (Zcur)
G17          (XY level)
G1 F1000     (Speed)
G90          (Impostazioni di quote absolute)
G60 X0       (Look ahead on)
G22 L8011 (Close Box)
G22 L8017 (Bnc ON)
G22 L8015 (Start)
(Mi Porto al centro dell'area di lavoro)
G61
: P1230=P1300 (laser power)
G4 X1.0      (wait 1 secondi)
G60 X0       (Look ahead on)
(Ciclo di pulizia)
G22 L8020 (Fast cleaning)
S10
G54 X3 Y-9 Z1.4
G0 X+0 Y+0 Z=P1404 F200 (mi Porto al centro dell'area di lavoro)
P1407=P1404 (Zcur=Z start)
N10 (*****INIZIO CICLO*****)
Q0=0 (OFF uscita veloce laser enable)
G0 X1.0 Y1.0 Z=P1407 F300
Q0=1 (ON uscita veloce laser enable)
G1 X-4.0 Y1.0 F=P1301
G1 X-4.0 Y5.0
Q0=0 (OFF uscita veloce laser enable)
: P1407= P1407+P1405 (incremento Z)
G27 X10 Z20 (20 cicli)
(Ciclo di pulizia)
G22 L8020 (Fast cleaning)
S10

G130 X=P1407 Z=P1406 K2 I10 (SE Z_cur < Z_end (X=P1407 > Z=P1406) SALTA A
N10)
N20

(-- End working part --)

(Powder feeder OFF)
(G22 L8026 (Powder Feeder 1 OFF))
```

G22 L8018 (Bnc OFF)
G22 L8016 (Stop)
(G22 L8010 (Open Box)
M30

Appendix E G-codes, cubes ($\theta_T=0$, $\theta_L=90$)

```
Cube-0-90-VH.DIN)
(Definizione variabili)
P1300=27 (Potenza laser)
P1301=100 (velocita' mm/min)
P1302=1000
P1400=2          (X start)
P1401=-10       (Y start)
P1404=0          (Z start)
P1405=0.009 (Z STEP T325) (THICKNESS OF LAYERS)
P1406=2 (Z stop) (Defined height)
P1407=0          (Zcur)
P1408=0.0045
G17              (XY level)
G1 F1000         (Speed)
G90              (Impostazioni di quote assolute)
G60 X0           (Look ahead on)
G22 L8011 (Close Box)
G22 L8017 (Bnc ON)
G22 L8015 (Start)
(Mi Porto al centro dell'area di lavoro)
G61
: P1230=P1300 (laser power)
G4 X1.0          (wait 1 secondi)
G60 X0           (Look ahead on)
(Ciclo di pulizia)
G22 L8020 (Fast cleaning)
S2
G54 X10.8 Y-0.4 Z2.45
G0 X+0 Y+0 Z=P1404 F200 (mi Porto al centro dell'area di lavoro)
P1407=P1404 (Zcur=Z start)

N10 (*****INIZIO CICLO*****
Q0=0 (OFF uscita veloce laser enable)
G0 X-4.3 Y8.0 Z=P1407 F3000
Q0=1 (ON uscita veloce laser enable)
(1)
G1 X-4.3 Y8 F=P1301
G1 X-4.3 Y5
Q0=0
G1 X-4.4 Y8 F=P1302
Q0=1
(2)
G1 X-4.4 Y8 F=P1301
G1 X-4.4 Y5
Q0=0
G1 X-4.5 Y8 F=P1302
Q0=1
(3)
```

```
G1 X-4.5 Y8 F=P1301
G1 X-4.5 Y5
Q0=0
G1 X-4.6 Y8 F=P1302
Q0=1 (ON uscita veloce laser enable)
(4)
G1 X-4.6 Y8 F=P1301
G1 X-4.6 Y5
Q0=0
G1 X-4.7 Y8 F=P1302
Q0=1
(5)
G1 X-4.7 Y8 F=P1301
G1 X-4.7 Y5
Q0=0
G0 X-7.3 Y5 Z=P1408 F3000
Q0=1 (ON uscita veloce laser enable)
(1)
G1 X-7.3 Y5 F=P1301
G1 X-4.3 Y5
Q0=0
G1 X-7.3 Y5.1 F=P1302
Q0=1
(2)
G1 X-7.3 Y5.1 F=P1301
G1 X-4.3 Y5.1
Q0=0
G1 X-7.3 Y5.2 F=P1302
Q0=1
(3)
G1 X-7.3 Y5.2 F=P1301
G1 X-4.3 Y5.2
Q0=0
G1 X-7.3 Y5.3 F=P1302
Q0=1 (ON uscita veloce laser enable)
(4)
G1 X-7.3 Y5.3 F=P1301
G1 X-4.3 Y5.3
Q0=0
G1 X-7.3 Y5.4 F=P1302
Q0=1
(5)
G1 X-7.3 Y5.4 F=P1301
G1 X-4.3 Y5.4
Q0=0
G1 X-4.2 Y8.1 Z=P1407 F=P1302
(Q0=1
(Contorno)
(G1 X-4.2 Y8.1 F=P1301
(G1 X-4.2 Y4.9
(G1 X-7.4 Y4.9
(G1 X-7.4 Y8.1
(G1 X-4.2 Y8.1

(Q0=0
(G1 X-4.2 Y8.1 Z=P1408 F=P1302
```

```
(Q0=1
(G1 X-4.2 Y8.1 F=P1301
(G1 X-4.2 Y4.9
(G1 X-7.4 Y4.9
(G1 X-7.4 Y8.1
(G1 X-4.2 Y8.1
(Q0=0
: P1407= P1407+P1405 (incremento Z)
: P1408= P1408+P1405 (incremento Z)
G27 X10 Z10 (10 cicli)
(Ciclo di pulizia)
G22 L8020 (Fast cleaning)
S2
G130 X=P1407 Z=P1406 K2 I10 (SE Z_cur < Z_end (X=P1407 > Z=P1406) SALTA A
N10)
(Ciclo di pulizia)
G22 L8020 (Fast cleaning)
S2
G61
: P1230=P1300 (laser power)
G4 X1.0 (wait 1 secondi)
G60 X0 (Look ahead on)
(Ciclo di pulizia)
G22 L8020 (Fast cleaning)
N20
      (-- End working part --)
      (Powder feeder OFF)
(G22 L8026 (Powder Feeder 1 OFF))
G22 L8018 (Bnc OFF)
G22 L8016 (Stop)
(G22 L8010 (Open Box)
M30
```

Appendix F Description of Finite Element

The finite element method is an approach for solving partial differential equations over geometrically complex domains. The method works by solving the equations over a simple domain, a rectangle for example. By combining many rectangles, it is possible to create complex shapes. Using small enough rectangles, any object can be well-represented, just as pixels can characterize an image. The simplified domain is called an element, and a finite number of them are used to form the global geometry. Depending on the problem at hand, elements may be lines, triangles, quadrilaterals, tetrahedrons, hexahedrons, or any shape which allows the partially differentiate equation (PDE) to be solved. Today, FEM has been applied to PDEs for heat transfer, fluid flow, and electromagnetic fields, but it was originally developed for the analysis of aircraft structures. ANSYS software is a worldwide leader in finite element simulation. ANSYS can handle, among other problems, material and geometric nonlinearities, stochastic analyses, multi-physics simulation, optimization, contact, composite materials, buckling, vibration, dynamic forces, and element death [96].